Department of Physics and Astronomy
Heidelberg University

Bachelor Thesis in Physics
submitted by

Theodor Brosi

born in Mühlacker (Germany)

2026

Kinematic signatures for fossil AGN outflows in the SDSS MaNGA sample

This Bachelor Thesis has been carried out by Theodor Brosi at the
Astronomisches Rechen-Institut in Heidelberg
under the supervision of
Prof. Dr. Dominika Wylezalek

Abstract (english)

Active galactic nuclei (AGN) play an important role in the evolution of their host galaxy by regulating many of their properties through complex feedback mechanisms. Although the importance of the AGN is well established, the lifecycle of such an event is still not fully understood. First observations and new simulations suggest the presence of AGN driven outflows even after the galaxy nucleus is no longer active. Using resolved spectroscopic data obtained with integral field units, these so-called fossil outflows can be studied on a larger scale. In this thesis I will present a selection method for fossil AGN outflows in the Sloan Digital Sky Survey-IV (SDSS-IV) Mapping Nearby Galaxies at Apache Point Observatory (MaNGA) galaxy sample comprising $\sim 10,000$ galaxies at low redshift. The method is based on kinematic elevation of the ionized gas, traced by broad [OIII]λ5007 emission line widths. To capture the broad outflow component, a multi-component emission line fitting model is applied. By comparing the gas kinematics with the stellar velocity dispersion, gas motions dominated by the gravitational potential can be distinguished from outflow-driven motions. Using this approach, a fossil outflow candidate sample of 390 non-AGN galaxies is identified and promising candidates in different remnant AGN phases are discussed in further detail. Analysis of the outflow properties show comparable mass outflow rates and energy rates of some fossil outflow candidates to currently active galaxies and simple outflow age calculations suggest outflow detections up to $\sim 8\,\mathrm{Myr}$ after the AGN shutdown.

Abstract (deutsch)

Aktive galaktische Kerne (active galactic nuclei, AGN) spielen eine wichtige Rolle in der Galaxieentwickling durch komplexe Feedback-Mechanismen, die die Galaxieeigenschaften regulieren. Obwohl die wichtige Rolle von AGN bekannt ist, fehlt ein genaues Verständnis des Lebenszyklus dieses Ereignisses. Erste Beobachtungen und neue Simulationen deuten auf detektierbare Ausflüsse aus dem Kern hin, nachdem dieser bereits nicht mehr aktiv ist. Mithilfe von integralen Feldeinheiten können diese sogenannten fossilen Ausflüsse durch aufgelöste Spektraldaten effektiv untersucht werden. In dieser Arbeit werde ich eine Selektierungsmethode für fossile AGN Ausflüsse in der Sloan Digital Sky Survey-IV (SDSS-IV) Mapping Nearby Galaxies at Apache Point Observatory (MaNGA) Galaxiesammlung vorstellen. Diese enthält $\sim$ 10.000 Galaxien bei niedriger Rotverschiebung. Die Methode basiert auf kinematischer Verbreiterung der [OIII]λ5007 Emissionslinie. Diese wird durch einen Fit mehrerer Komponenten an die Emissionslinie bestimmt, die die durch den Ausfluss verbreiterte Linie modellieren. Dabei wird zwischen Gas, das durch das Gravitationspotential dominiert wird, von ausflussgetriebenem Gas mithilfe der stellaren Geschwindigkeitsdisperion unterschieden. Durch diese Methode wurden 390 nicht aktive Galaxien in unterschiedlichen Stadien gefunden, die potentielle Kandidaten für fossile AGN Ausflüsse sind. Bei der Analyse der Ausflusseigenschaften werden teilweise vergleichbare Masseausflussraten und Energieraten wie bei aktiven Galaxien festgestellt. Durch eine einfache Abschätzung werden Detektierungen von Ausflüssen bis zu $\sim 8\,\mathrm{Myr}$ nach dem Abschalten der zentralen Aktivität abgeschätzt.

Contents

Acronyms & Symbols

A/N	Amplitude over Noise ratio
AGN	Active Galactic Nucleus
APO	Apache Point Observatory
BAT	Burst Alert Telescope
BH	Black Hole
BLR	Broad Line Region
CCD	Charged-Coupled Device
CCL	Connected Component Labeling
DAP	Data Analysis Pipeline
DBSCAN	Density-Based Spatial Clustering of Applications with Noise
DRP	Data Reduction Pipeline
EELR	Extended Emission Line Regions
FITS	Flexible Image Transport System
FWHM	Full Width Half Maximum
HST	Hubble Space Telescope
IFS	Integral Field Spectroscopy
IFU	Integral Field Unit
IMF	Initial Mass Function
ISM	InterStellar Medium
KDR	Kinematically Disturbed Region
LINER	Low-Ionisation Nuclear Emission-line Region
LOS	Line Of Sight
LOSVD	Line Of Sight Velocity Distribution
ΛCDM	Lambda (Λ) Cold Dark Matter cosmological model
MaNGA	Mapping Nearby Galaxies at Apache Point Observatory
MIR	Mid InfraRed
$M_{\odot}$	Solar Mass
$M_{\star}$	Stellar Mass
NIR	Near InfraRed
NLR	Narrow Line Region
NRAO	National Radio Astronomy Observatory
NVSS	NRAO Very Large Array Sky Survey
PAGB	Post-Asymptotic Giant Branch stars
pc	Parsec
pPXF	penalized PiXel Fitting
PSF	Point Spread Function

Quasars	Quasi-stellar radio source
SDSS	Sloan Digital Sky Survey
SED	Spectral Energy Distribution
SF	Star Formation
SFR	Star Formation Rate
SMBH	Super Massive Black Hole
SNR	Signal-to-Noise Ratio
SSP	Simple Stellar Population
WISE	Wide-field Infrared Survey Explorer

1 Introduction and physical background

1.1 Active galactic nuclei

The radiation of regular galaxies is dominated by the thermal radiation emitted by the plasma in the stars athmospheres. With temperatures ranging from $3,000\,\mathrm{K} \lesssim T \lesssim 40,000\,\mathrm{K}$ the Planck spectrum is restricted between $\sim 4,000\,\text{Å}$ and $\sim 20,000\,\text{Å}$ which is near infrared (NIR) to optical wavelengths. Then there are galaxies that exhibit an enormus band width with additional radio-, X-ray and gamma ray radiation. The emission originates from a small central region which is called Active Galactic Nucleus (AGN). This broad spectrum, whose luminosity typically reaches or even exceeds the one from the stellar contribution of the entire host galaxy, indicates that the emission is not entirely of thermal origin and is attributed to accretion onto a supermassive black hole (SMBH, Schneider 2006 chapter 5). SMBH are present in most or even all centers of massive galaxies (Graham 2016).

1.1.1 The unified model

Historically AGN were classified by their differences in luminosity, radio emissions and broadness of their emission lines but can be united in the unified model of AGN (Antonucci 1993; Urry and Padovani 1995) displayed in figure (1).

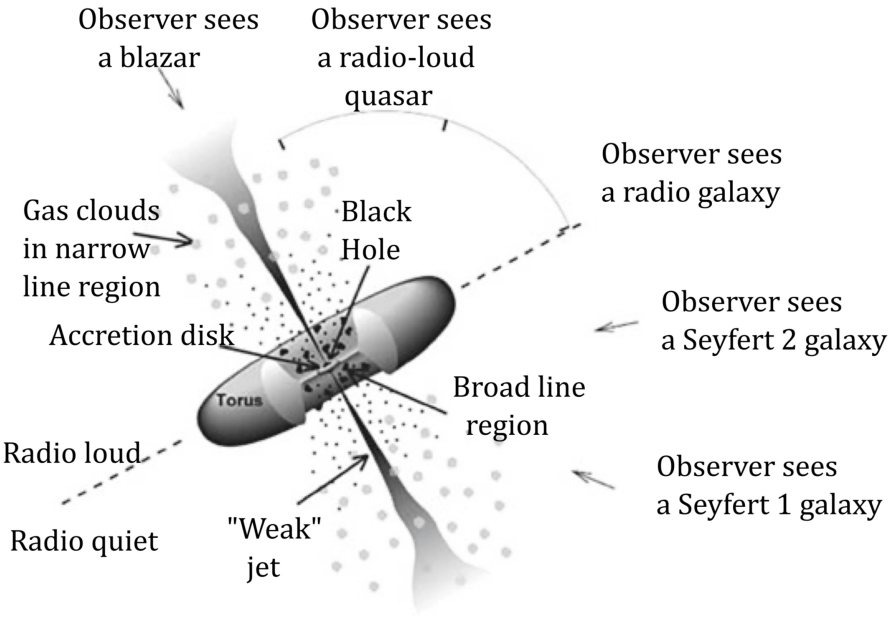

Figure 1. Unified model of AGN with different classifications depending on the viewing angle. The top half shows the observed type for radio-loud AGN and the bottom half for radio-quiet AGN. This differentiation must be taken with caution as radio-quiet AGN show low but measurable radio emissions as well. (Urry and Padovani 1995, modified by Horvath 2022)

The unified model suggests a similar structure for all AGN with the different observed AGN types depending on the observing angle. In the center there is an actively accreting SMBH with a mass range of $10^5 M_\odot < M_{\rm BH} < 10^{10} M_\odot$. Around it is the accretion disk on sub-parsec scales where gas is performing a differential rotation because of their angular momentum components. The resulting friction leads to infalling gas, converting gravitational potential into continuum radiation (Alexander et al. 2025; Schneider 2006 chapter 5.3). A hot corona surrounding the accretion disk Compton-up-scatters photons from the disk into the X-ray regime. Nearby high density gas clouds ($< 1\,$pc) get accelerated and exited by the radiation from the accretion disk, emitting collisionally ionized emission lines with extreme doppler broadening. This is called the Broad Line Region (BLR). Further away towards kpc scales the gas cloud density decreases. Still ionized by the central source they only emit narrower emission line leading to the name Narrow Line Region (NLR). Due to the lower density, forbidden emissions are produced apart from the permitted lines. Surrounding the accretion disk spanning $0.1 - 10\,$pc, an optically thick dusty torus is obscuring the line of sight. For radio loud AGN collimated emission structures, so-called jets, connect radio lobes through the central source spanning up to $1\,$Mpc (Schneider 2006 chapter 5.4).

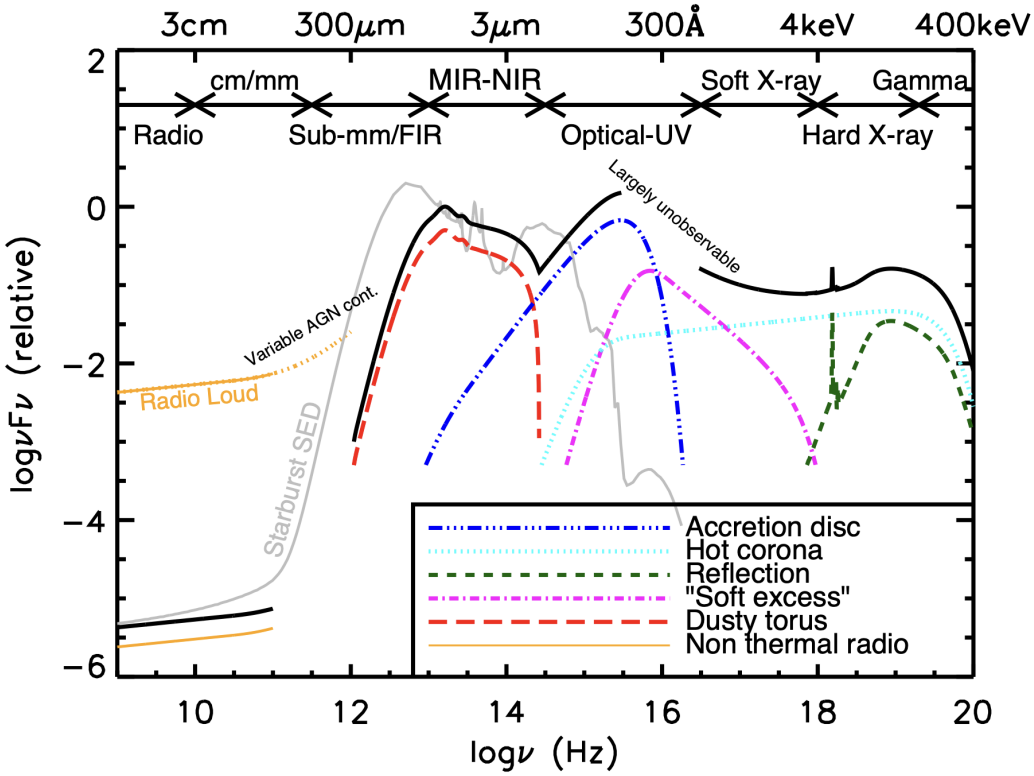

Figure 2. A schematic representation of an AGN Spectral Energy Distribution (SED). The solid black curve represents the total SED and the colored curves (with an arbitrary offset) represent the emission of the individual components described in this section. The grey curve shows an example radio-UV SED of a starburst galaxy. The figure is taken from Harrison (2014).

1.1.2 AGN populations in the local universe

From the unified model, it can be seen that AGN do not significantly differ in their structure but in the observed spectrum. Nevertheless, at lower redshift Heckman and Best (2014) suggest two main AGN populations. First, the radiative-mode AGN where efficient conversion of potential energy in electromagnetic radiation through the mechanism described above takes place. Jet-mode AGN on the other hand, lack or have only a truncated accretion disk and rather have a geometrically thick structure, which results in advection dominated or radiatively inefficient accretion flows. On this basis the most important types in the nearby universe will be shortly discussed.

Seyfert Galaxies are radio quiet, radiative mode AGN. They are a lower luminosity AGN-type and mostly found in spiral galaxies. Two types are differentiated. Type I seyfert galaxies show both broad (FWHM $\gtrsim 1000\,\mathrm{km\,s^{-1}}$) and narrow emission lines because it is possible to look directly at the BLR. In Type II syfert galaxies, the torus obscures the BLR and only narrow emission lines can be seen.

Radio-AGN are jet-mode AGN. These flows are capable of launching two sided jets that can extend on Mpc scales. The Radio-loud population is the less abundant type of AGN (Kellermann et al. 1989) compared to the radio-quiet population.

LINER (Low-Ionisation Nuclear Emission-line Region) is a galaxy that has overall lower luminosity and different relative strength of their emission lines compared to Seyfert galaxies (Heckman 1980). If confirmed to be AGN they would make up the largest fraction of the AGN population (Ho 2008). There is still an ongoing debate whether these objects host jet-mode AGN or whether their emissions can be explained with ionizing photons from post-Asymptotic Giant Branch stars (pAGB). Additional diagnostics are required here and will be discussed later.

1.1.3 Accretion luminosity

The luminosity produced by mass accretion $\dot{M}$ on the SMBH is given by:

$$L_{acc} = \epsilon \dot{M} c^2 \tag{1}$$

and is often referred to as accretion or bolometric AGN luminosity. Here c is the speed of light and the mass-energy efficiency conversion ϵ is typically estimated to be $\epsilon \approx 0.1$. This is theoretically well motivated for radiative mode AGN, radiating at a significant fraction of the Eddington limit but may be underestimated for jet-mode AGN radiating at small eddington ratios (Heckman and Best 2014).

The Eddington ratio:

$$\lambda_{Edd} = \frac{L_{acc}}{L_{Edd}} \tag{2}$$

is used to compare accretion rates of BH with different masses M_{BH} as higher mass BH typically have higher luminosities. It measures L_{acc} in ratio to its theoretical upper limit called the "Eddington luminosity" L_{Edd}. It is calculated over the balance of the radiation pressure created by accretion of fully ionized hydrogen onto the BH and the gravitational force:

$$L_{Edd} = \frac{4\pi G M_{BH} m_p c}{\sigma_T}. \tag{3}$$

Here G is the gravitational constant, m_p the proton mass and σ_T the Thompson cross section for an electron.

1.2 Galactic winds and outflows

1.2.1 AGN driven outflows and feedback modes

Close to the center of an AGN a huge amount of energy, momentum and mass can be released from the accretion disk or dusty torus surrounding the black hole. This can manifest in radio jets or a radiatively-driven wind, which will be discussed in this section. The via accretion released energy over the black hole's lifetime exceeds the galactic binding energy by a factor of ~ 100 (Fabian 2012; Alexander et al. 2025). So even if a small fraction of this energy couples to the interstellar medium (ISM) it can have a large effect on the host galaxy and its evolution. It is thought that the jets and winds produced in the central pc sweep up the gas in the ISM, resulting in kpc scale gaseous outflows that have become increasingly observable in recent years thanks to spatially resolved spectroscopy (e.g. Rupke and Veilleux 2013; Liu et al. 2013).

The interaction of the AGN driven winds and outflows with its host galaxy is described as feedback (Fabian 2012). In the "radio mode feedback" (also "maintanance mode" or "hot halo mode" feedback) the bulk of energy created by accretion is concentrated and channeled into powerful radio jets that produce radio lobes that expand outward. Through the mechanical work required to inflate the cavities, the outflow deposits energy heating up the gas. This prevents the gas from cooling down and forming regions of higher density which is required for stars to form. This feedback mode is thought to be most efficient in periods of low black hole accretion rates and found in radio-loud AGN. In the case of rapid accretion in luminous AGN "radiative mode" feedback is proposed (also "quasar mode" or "superwind mode" feedback). Gas gets expelled by outflows shutting down future BH growth and star formation (SF, see Heckman and Best (2014) for further description). An illustration of the two feedback modes can be seen in figure (3). In addition to the negative feedback quenching SF, AGN driven outflows could cause positive feedback by inducing pressure in cold gas reservoirs triggering star formation (Zubovas et al. 2013).

The here discussed AGN feedback plays a crucial role in galaxy evolution. Models

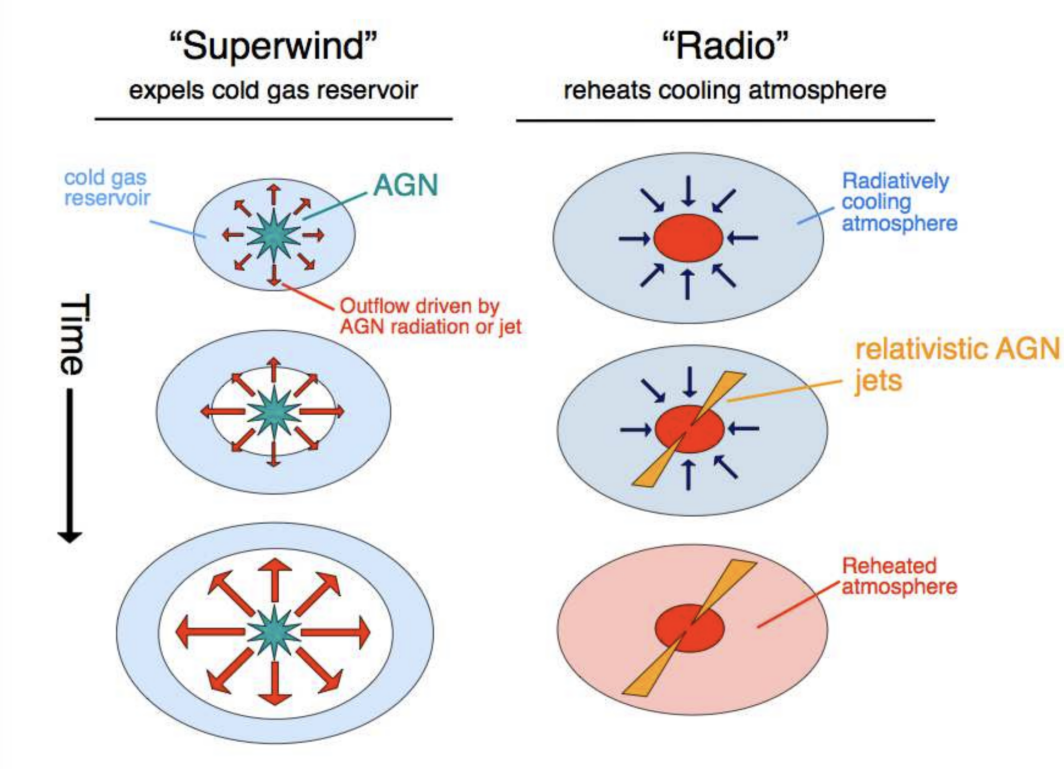

Figure 3. A schematic representation of "superwind mode" feedback (also known as "radiative mode" or "quasar mode") and "radio mode" feedback (also known as "maintanance mode" or "hot-halo mode") taken from Alexander and Hickox (2012).

that do not take AGN feedback into account turn out to be gas-rich, actively star-forming and fail to quench, failing to reproduce key observed properties of galaxy evolution and star formation history (see Alexander et al. (2025) section 6, and references therein). By suppressing the cooling in massive galaxies AGN feedback sets the upper limit to the masses of the galaxies (Ferrarese and Merritt 2000; Fabian 2012) and mediates the morphological transition from disk to elliptical galaxies (Dubois et al. 2016), likely by preventing disks from re-forming after major galaxy merger events.

Further signs of the coevolution of the SMBH and the host galaxy are tight correlations between the mass of the SMBH and galactic bulge (the dense central region of a spiral galaxy) properties, such as the bulge mass (Häring and Rix 2004), the bulge velocity dispersion known as the M-σ relation (Ferrarese and Merritt 2000), and the bulge luminosity (Magorrian et al. 1998; Marconi and Hunt 2003). Feedback during an active phase is required to link these properties.

1.2.2 Star formation driven outflows

It is important to note that galactic outflows can also occur due to massive stars that are product of high star formation rates (SFR). Their strong stellar winds and radiation combined with their quicker life cycle resulting in supernovae can also drive large scale

outflows (Chevalier and Clegg 1985; Murray, Quataert, and Thompson 2005). As a consequence they can alter the host galaxy and evolution in a similar way than AGN-driven outflows and can possibly slow down the rate for subsequent SF.

While star formation driven outflows in star-forming galaxies at higher redshift seem to be ubiquitous (Shapley 2011), in the local universe strong winds are only observed in intense star burst galaxies (Heckman, Armus, and Miley 1990). Being a complex multiphase phenomenon spanning from cold molecular gas to hot ionized gas (Veilleux, Cecil, and Bland-Hawthorn 2005) and being a wide-angle bipolar outflow along the galaxy minor axis (Chen et al. 2010) there can be difficulties distinguishing it from AGN-driven outflows. Besides line diagnostics that will be touched on later, SF driven winds are associated with high SFR per unit area (Chen et al. 2010) and Heckman et al. (2015) showed that measured outflow velocities correlate well with the global SFR and indicated that there is a higher limit for the outflow velocity that can be achieved via SF.

1.3 Coevolution of galaxies and SMBH over cosmic time

Apart from the different historical classifications of different observed AGN properties, generally all galaxies have been classified in some way. The well known hubble sequence (Hubble 1926) is a purely optical classification based on galaxy morphology and differenciates elliptical (E), spiral (S) and barred-spiral (SB) galaxies. Later in a revised version of (Kormendy and Bender 1996) a few changes were made, such as including irregular galaxies and reordering the ellipticals by the isophote shape shown in figure (4).

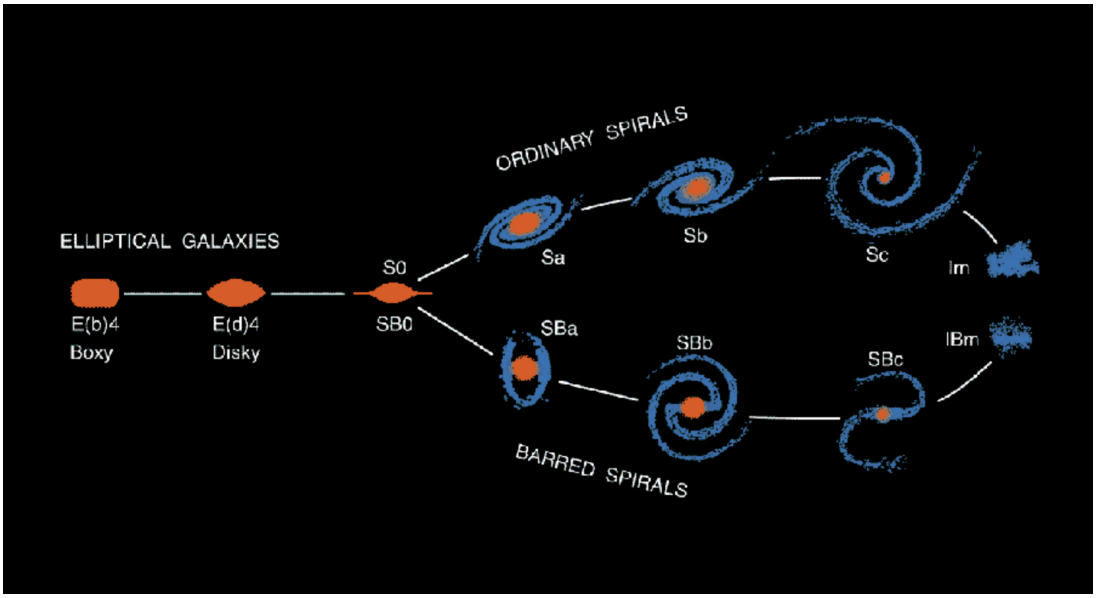

Figure 4. The revised Hubble tuning fork taken from (Kormendy and Bender 1996). The elliptical galaxies are referred to as early type galaxies and the spiral and barred galaxies as late type galaxies although this is only a morphological classification and does not infer actual galaxy evolution steps.

This classification is connected to a clear bimodality in the galaxy population in the contemporary universe (Kauffmann et al. 2003a; Baldry et al. 2004). The bimodal distribution of galaxies can be seen in figure (5) and is divided into the "blue cloud", galaxies that exhibit ongoing star-formation and have more shortlived hotter stars that have a bluer color, and the "red sequence" which has an older stellar population and little SFR and therefore showing the redder color of these older stars. The galaxies in the blue sequence share further properties like small stellar masses $M_\star$ and a small concentration of their light and are associated to late hubble type galaxies. Subsequent analysis showed a tight correlation between the SFR and $M_\star$ known as the star-forming main sequence (Brinchmann et al. 2004; Schiminovich et al. 2007) for the blue population. The red population is linked to early type galaxies with higher stellar masses and wider spread of their light. In between the two populations lies the "green valley" with a small galaxy density which indicates a fast transition from the the blue to the red population. In fact, studies over cosmic time showed a build up of the red sequence from $z = 2.5$ to $z = 0$ (Bell et al. 2004; Whitaker et al. 2012).

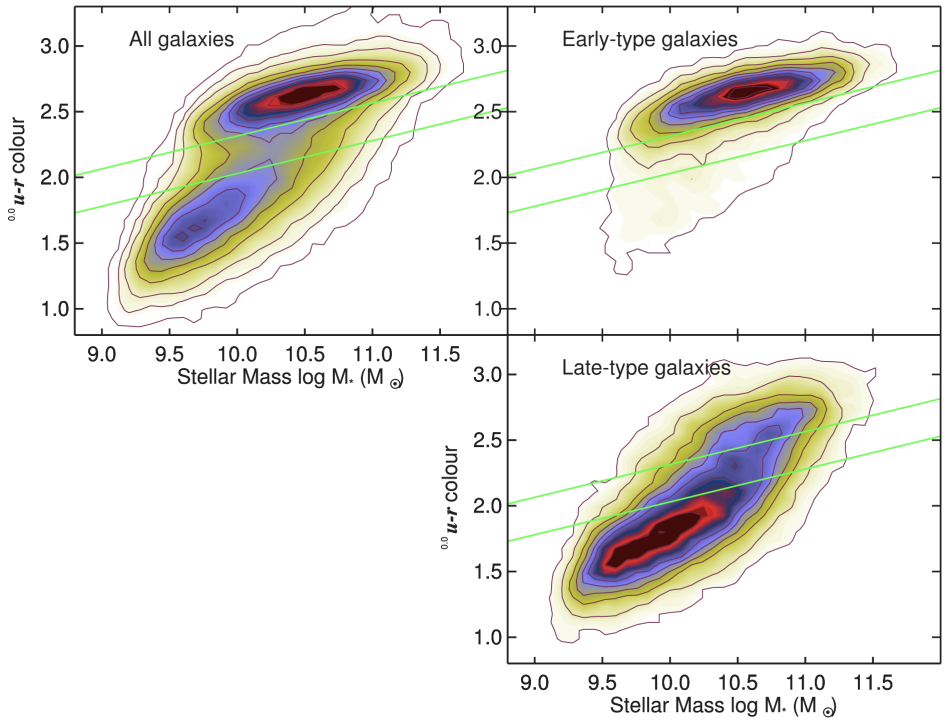

Figure 5. $u - r$ color mass diagram for a low redshift galaxy sample taken from (Schawinski et al. 2014). The color is defined over the the magnitudes in the u (ultraviolet) and r-band (red). Because of the logarithmic magnitude scale, in which smaller magnitudes correspond to brighter objects, a smaller $u - r$ index corresponds to a bluer color and higher index corresponds to a redder color.

In this simple galaxy evolution picture (e.g. Lilly et al. 2013) a galaxy increases in mass through accretion of cold gas from the cosmic web and through galaxy mergers,

evolving along the blue star-forming sequence. At some point at higher mass the cold gas supply is shut off, the SF is quenched and the galaxy evolves into the red population. The complete physical process of the quenching of galaxies is still unclear but as established in section (1.2.1) AGN driven outflow is needed to heat and eject gas from the galaxy. Apart from the signs for coevolution stated above, both the cosmic SFR density (Madau et al. 1996) and the cosmic BH growth (Marconi et al. 2004; Aird et al. 2010) peak around $z \sim 2$ called the "cosmic noon" (figure (6)).

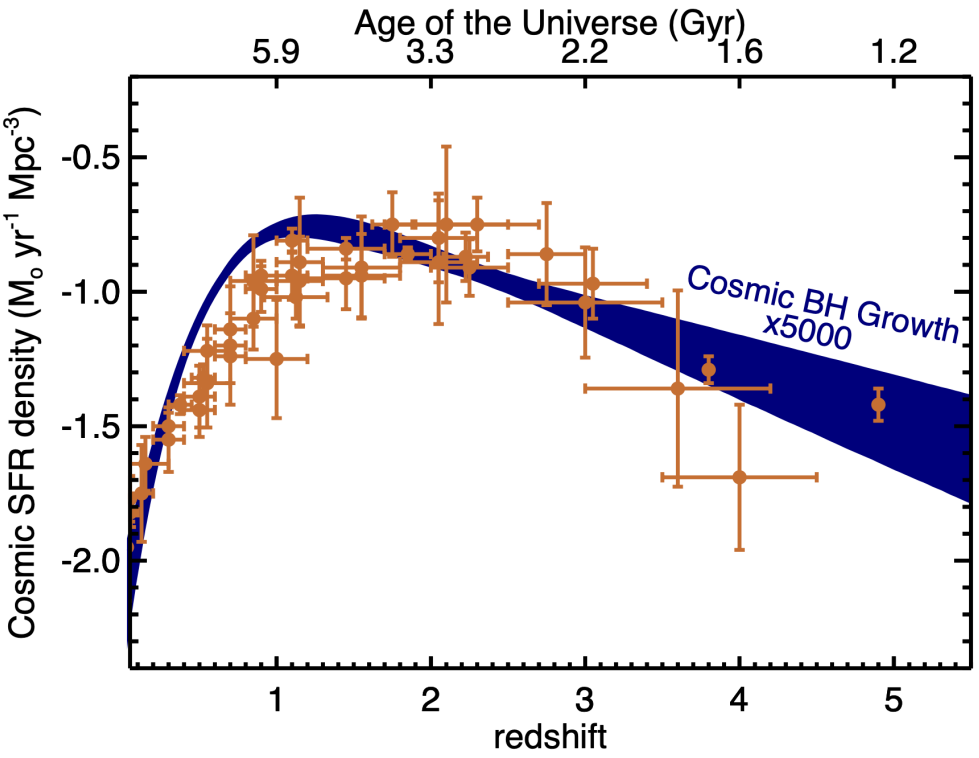

Figure 6. Volume averaged SFR density as a function of redshift. The plot is taken from Harrison (2014) with data points for the SFR density from the compilation by Madau and Dickinson (2014) and a representative model of the observed evolution of BH growth scaled by $\approx 5,000$ taken from Aird et al. (2010). Both curves show a broad maximum around $z \sim 2$ with a steep decline towards $z = 0$.

This not only tells a story of the coevolution of BH with their host galaxy but also indicates that the spatial Quasar (Quasi-stellar radio source) density was much higher at earlier times as BH growth happens during active phases. Quasars are the most luminent AGN with Seyfert-like spectra often completely outshining the light of their entire host galaxy which gave them their name of quasi-stellar objects. Due to the expansion of the universe and galaxy clusters virializing over time, mergers were more common in earlier cosmic times (Kormendy and Kennicutt Jr. 2004). This sets a picture of a quasar evolutionary sequence where two gas rich galaxies merge, driving gas into the central region, triggering intense dust-obscured SF. This enhances the gas inflow, resulting in initially obscured quasar activity. Due to the large gas supply, the quasar will ultimately

drive the gas and dust away, revealing an unobscured quasar and shutting down SF. This leaves a quienscent or inactive galaxy behind (see Alexander et al. (2025) section 5 and references therein).

As mergers become less common, evolution in the present days and in the future is expected to proceed predominantly through secular processes, such as gas inflow driven by bars and spiral structures that feed the central BH (see Alexander et al. (2025) section 4 for a systematic review).

1.4 Fossil outflows

An important detail of AGN is that the active growth of the SMBH and therefore the timespan in which outflows and feedback mechanisms happen, is an event and therefore time-limited. A first remnant of this event was observed during the Galaxy Zoo Project (Lintott et al. 2008; Lintott et al. 2011), which is a project where over 100,000 participants classified around 900,000 objects from the Sloan Digital Sky Survey (SDSS) with comparable accuracy to professional astronomers. One of the voluntary researchers, Hanny van Arkel, a dutch teacher, made an unusual finding. She spotted a giant highly ionized nebula near the spiral galaxy IC 2497 (at least 50 kpc away) emitting green light because of the domination of the emission lines [OIII]$\lambda\lambda$4959,5007 that will be touched on later. This object later called "Hanny's Voorwerp" (dutch for Hanny's object) can be seen in figure (7).

Emission line ratios from spectra in Lintott et al. (2009) indicate ionizing of the nebula by an AGN rather than hot stars. Follow up radio observations with the Westerbork Synthesis Radio Telescope (Józsa et al. 2009) detected an asymmetric radio jet originating at the center of IC 2497 and pointing towards the ionsized nebula, indicating an ongoing AGN outflow that is still ionizing the nebula. X-ray observations with *XMM-Newton* and *Suzaku* (Schawinski et al. 2010) show low X-ray luminosity and observations with the Hubble Space telescope (Keel et al. 2012b) support the picture of a fading AGN that has not enough power to drive an outflow this far ionizing the complete region. Hanny's Voorwerp is therefore believed to be a signature of a fossil outflow meaning from a past more active phase. The following scenario is proposed: A major merger triggered an active phase with ionizing luminosity appropriate for a quasar. The merger left a massive tail of H I (molecular hydogen) and a remnant IC 2497 with a significantly warped disc. The escaping radiation of the quasar ionized parts of the H I tail. Meanwhile the AGN shut down to a modest Seyfert or LINER level within 10^5 yr leaving the situation as can be seen today.

Since this first observation, more less luminous AGN-ionized gas clouds (Extended Emission Line Regions, EELR) on large scales ($10 - 40$ kpc) from the galaxy center were found within the Galaxy Zoo project (Keel et al. 2012a) preferentially in disturbed sys-

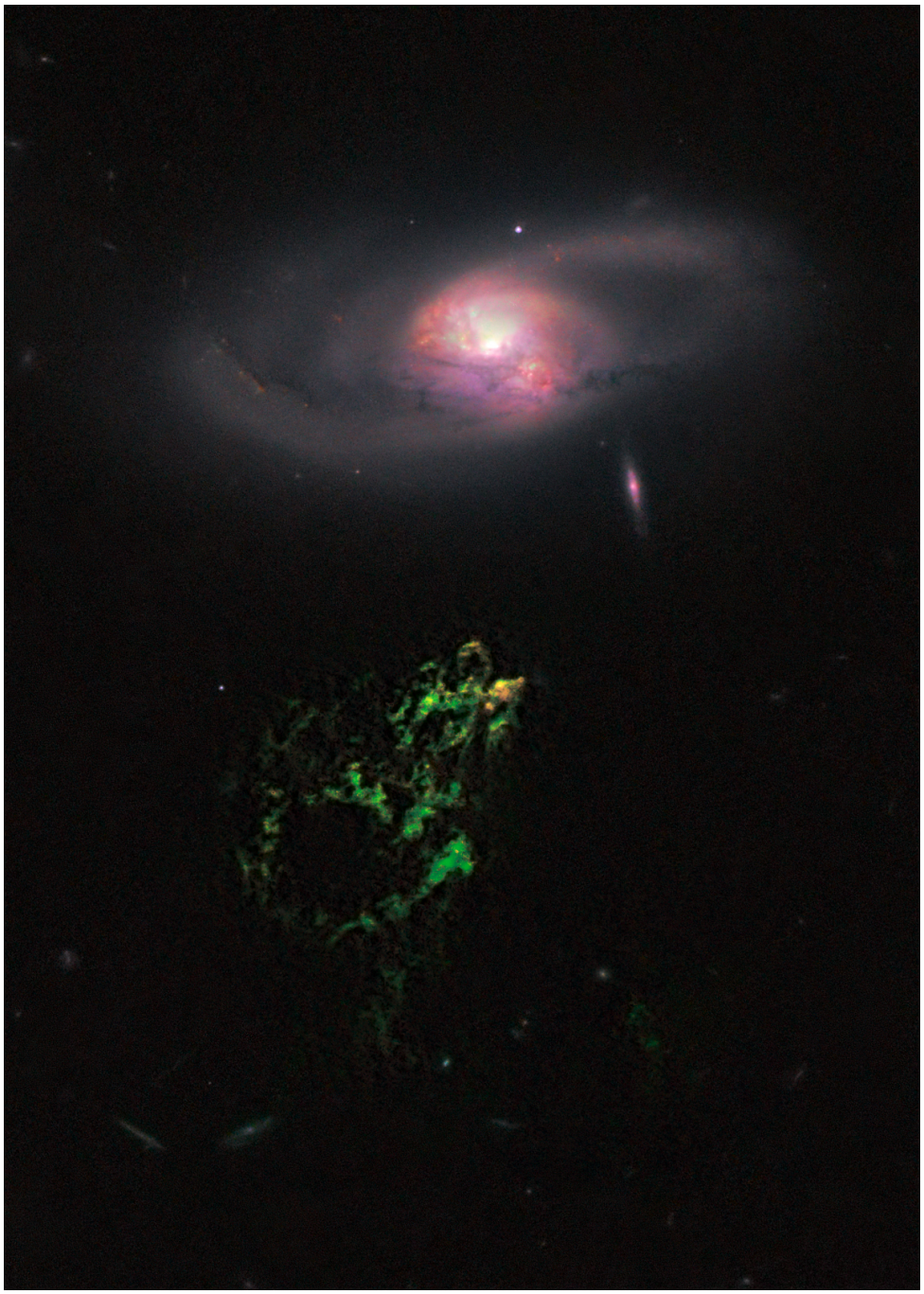

Figure 7. Composite image by NASA's Hubble Space Telescope (HST) of spiral galaxy IC 2497 and Hanny's Voorwerp. It combines seperate exposures from the Advanced Camera for Surveys and the Wide field Camera 3 on the HST assigning different colors to the greyscale images of the individual filters. The assigned colors are Dark green: F160W (H) Dark red: F814W F814W (I) Red: FR716N (Redshifted H-alpha) Green: FR505N ([OIII]) Blue: WIYN (B) and the picture was taken from NASA 2011.

tems, rising in many cases from tidal tails. At higher redshift ($z = 0.2 - 0.6$) analysis of SDSS photometric data revealed ultraluminous NLR in the g-band in some galaxies giving them the name "Green Beans" (Schirmer et al. 2013). These galaxies show emission line ratios in the NLR clearly powered by an AGN but the mid-IR emissions measured with

WISE are 5-50 times lower, suggesting an already faded AGN and a light echo interpretation for those sources. Fossil outflows might also be present in our own galaxy, the Milky Way, in the form of the fermi bubbles (Su, Slatyer, and Finkbeiner 2010), which are giant lobes extending above and below the galactic plane. They were detected in the γ-ray regime but are also visible in X-ray and microwave emissions and are speculated to originate from past activity of our central BH Sgr A* (Zubovas and Nayakshin 2012).

Analysing the timescales and the theoretical lifecycle of an AGN event recently made further progress in observational studies and simulations. Many X-ray detected AGN without an ionized NLR which indicates recently turned on AGN as the NLR responds to AGN radiation only after light-travel times of $10^3 - 10^4$ yr were found. Their frequent occurrence together with the estimates of the age of the "Voorwerpes" implies an active phase of $\sim 10^5$ yr (Schawinski et al. 2015). Regarding total accretion time-scales of $10^7 - 10^8$ yr (Marconi et al. 2004) this indicates that AGN "flicker" on and off. Semi-analytical estimates show that because of the higher dynamical scale of the outflow of $10^5 - 10^6$ yr (Zubovas 2018) compared to the AGN event, up to 60% of of all observed outflows may be fossil (Zubovas, Bialopetravičius, and Kazlauskaitė 2022). However, the derived timescale of the outflows is probably an overestimate since the outflow would become undetectable once its velocity drops below the typical velocity dispersion of the ISM. The properties of fossil outflows were explored in hydrodynamical simulations in idealized galaxy bulges (Zubovas and Maskeliūnas 2023) and will be quickly summarized here:

(i) Detachment: fossil outflows are spatially detached from the nucleus, showing inflowing or turbulent gas between the outflow bubble and the nucleus.

(ii) Asymmetry: while driven outflows are more symmetrical and form a biconical shape along the less dense galactic minor axis, in fossil outflows one of the cones is likely to stall and collapse earlier than the other leading to a lobsided shape.

(iii) Multiphase structure: fossil outflows have lower ratio of ionized gas to atomic/molecular gas than driven ones as the gas cools down much faster than it dissipates.

The simulations also showed that fossil outflows only form in galaxies with large enough eddington ratio λ_{Edd} or low enough gas fraction $f_g = \rho_{gas}/\rho_{tot}$ compared to the total stellar and gas mass given with $\lambda_{Edd} \gtrsim 7 f_g$. For galaxies with lower AGN luminosity or higher gas fraction, the fossil outflow stalls and collapses in a tenth of the AGN episode duration. So fossil outflows should be rare in very gas rich systems but rather common in typical systems in the local universe. Because the bulge masses at higher redshift ($z \sim 2$) are lower by 1-2 orders of magnitude for a given SMBH mass, fossil outflows are probably more common.

1.5 Scope of this thesis

Based on the investigations of fossil outflows and predictions of simulations, one can suspect that a large number of fossil outflows may be hiding in the data of inactive galaxies. New spatially resolved observations, which are made possible by integral field spectroscopy (IFS), should help to detect these outflows. This work focuses on a systematic search for fossil outflows in the SDSS MaNGA (Mapping Neaerby Galaxies at Apache Point observatory) sample comprising optical and resolved spectra of $\sim$ 10,000 galaxies. I will only focus on galaxies that have not been classified as AGN by different selection methods and the goal is to find as many possible fossil outflow candidates as possible. To detect the outflows, the kinematic disturbance in the ionized gas will be analyzed with the emission line width of the prominent [OIII]λ5007 emission line. The elevation on gas kinematics will be assesed relative to the stellar kinematics and on the basis of absolute elevation. The elevated regions will be clustered to statistically significant region detections. This described method aims to detect fossil outflows of more recently turned off AGN since it does not depend on visual identification in EELR like tidal tails that are illuminated by coincidence. The resolved nature also poses the possibility of excluding galaxies that show ionized gas signatures only in their core and investigate those who show them further out. Subsequent analysis of the fossil outflow candidated detected in this way will help investigate the activity histories of galaxies and therefore create a more complete picture of AGN and host galaxy evolution. Their number could shed more light to the hypotheses of the prevalence of fossil outflows over driven ones and the outflow ages can be compared to the estimates of the timescales of the persistence of these outflows.

The thesis is structured as follows: In section 2 I will present an overview of the observational data from the MaNGA survey and in section (3) describe the methods used for evaluating the kinematic disturbance as well as AGN selection techniques and fitting procedures since I will mostly work with processed and analyzed data. The used prosessed data sets are described in section 4 and the analysis and search for the outflows are carried out in section 5. In section 6 the final sample is inspected and discussed and promising sources are presented. At the end in section 7 the results are concluded and an outlook is given.

1.6 Assumed cosmology

Since distances and luminosities that I want to work with in this thesis differ for different cosmological models, I want to give a short overview of the used model. I implement the flat Lambda Cold Dark Matter ΛCMD model with the hubble constant $H_0 = 70\ \mathrm{km\,s^{-1}\,Mpc^{-1}}$, $\Omega_m = 0.3$ and $\Omega_\Lambda = 0.7$. H_0 describes the current rate of expansion of the universe, the density parameter of matter Ω_m accounts for baryonic and dark matter and the vacuum energy Ω_Λ represents the dark energy. The density parameter

accounting for radiation will be neglected and curvature is assumed to be zero. These density parameters tell us how much matter and the cosmological constant Λ contribute to the total density of the current epoch.

An integral ingredient to measure the distance (Hogg 2000) is the cosmological redshift z, caused by the Doppler shift of a photon emitted with wavelength λ_{em} and the observed wavelength λ_{obs} because of the expansion of the universe. It is defined over:

$$z = \frac{\lambda_{obs} - \lambda_{em}}{\lambda_{em}}. \tag{4}$$

Further, the comoving distance D_C is needed which is the distance between two objects in the universe that remains constant over time because it factors out the expansion of the universe. It is calculated as follows:

$$D_C = c \int_0^z \frac{dz'}{H(z')}, \qquad H(z) = H_0 \sqrt{\Omega_m (1+z)^3 + \Omega_\Lambda} \tag{5}$$

with the Hubble constant $H(z)$ as measured by a hypothetical astronomer working at redshift z.

Now, the angular distance D_A can be calculated with the comoving distance defined by the following relation:

$$D_A(z) = \sqrt{\frac{R^2 \pi}{\omega}} = \frac{D_C}{1+z}. \tag{6}$$

R is the radius of a source and ω the solid angle it appears in. The luminosity distance D_L is defined as the relation of the bolometric (integrated over all frequencies) luminosity L with the measured bolometric flux S by:

$$D_L = \sqrt{\frac{L}{4\pi S}} = (1+z) D_C \tag{7}$$

The Two distance measures are connected over:

$$D_L = (1+z)^2 D_A. \tag{8}$$

2 Observational Data

The Sloan Digital Sky Survey (SDSS, York et al. 2000) began regular observations in the year 2000, starting off by imaging half the northern sky and mapping the 3-dimensional clustering of one million galaxies and 100,000 quasars in the first years. SDSS uses mostly the 2.5m Sloan Foundation Telescope (Gunn et al. 2006), which is located in the Apache Point Obervatory (APO) in New Mexico. In its various projects until the third generation (SDSS-III) the observational technique for spectroscopy was single fiber spectroscopy. Here single fibers with a set aperture are used to observe specific regions in the sky. The collected light intensity is integrated over the the entire aperture, resulting in a single spectrum for each object. In this way many spectra can be captured at once like it was done for SDSS I and II, where plates with 640 individual fibers with 3" aperture, distributed to match the sky positions of the 640 targets, could be observed together. But if resolvable objects such as nearby galaxies are observed, simply pointing in the center does not capture galaxy properties that vary with distance from the center. Only an averaged spectrum possibly of different galaxy components is extracted, which is difficult to compare with other galaxies at different distances since it integrates over different galaxy size proportions.

2.1 SDSS Mapping Nearby Galaxies Galaxies at APO

In the fourth project phase (SDSS-IV) spatially resolved spectroscopy was introduced in the form of Integral field Units (IFUs, Allington-Smith and Content 1998 for an overview of the techniques) in the Mapping Nearby Galaxies Galaxies at APO (MaNGA, Bundy et al. 2015) survey. For the MaNGA survey this is achieved by an array of fibers each with a diameter of ~ 2" in the telescope focal plane. They are organized in a hexagonal shape with different sizes (19, 37, 61, 127 fibers) depending on the apparent size of the target galaxy ranging in diameter from 12-32 arcseconds. Since the fibers are circular, dithering is applied, where the whole IFU is offset between observations to fill the gaps. In one set observations take place in three different positions each with a 15 minute integration time and each source is observed in multiple sets totaling 3 hr in the median conditions. The spatially resolved spectra cover the optical range of 3622 Å to 10354 Å at a spectral resolution of $R \sim 2000$. This results in a median spectral resolution of $\sigma = 72\,\mathrm{km\,s^{-1}}$.

The limit for the spatial resolution is given through the aperture or fiber size over which the collected light is integrated and other effects modeled in the point spread function (PSF). The PSF is a model for the spatial spread of a point source of light which is caused by diffraction on the aperture or mirrors in the telescope in case of ideal optics. In reality seeing effects, caused by atmospherical turbulence, and optical abberations caused by the telescope geometry or different wavelengths being deflected differently dominate the PSF for ground based telescopes. The median reconstructed spatial resolution is 2.54".

2.2 MaNGA Data Release 17 and Data Reduction Pipeline

MaNGA data was released in several data releases. The last one, the 17th data release (DR17, Abdurro'uf et al. 2022), includes resolved spectra of 10,010 unique galaxies. They were chosen at low redshift $0.01 \lesssim z \lesssim 0.15$ with an approximately flat stellar mass distribution of $M_\star/M_\odot = 10^9$ from the SDSS Main Galaxy Sample (Strauss et al. 2002). This sample was selected from the photometric data obtained by the imaging survey. At the median redshift of $z = 0.037$ the spatial resolution translates to 1.8 kpc (Bundy et al. 2015). Two third of the MaNGA galaxies are targeted to be covered out to $1.5\,R_e$ and the other third out to $2.5\,R_e$, where R_e is the radius which encloses half of the total emitted light from the galaxy (Law et al. 2016).

After the observations, the data goes through a Data Reduction Pipeline (DRP, Law et al. 2016) before they are released. The DRP is generally split into two phases. In the first phase, a 2D-reduction is performed, where bias correction, flatfiedling, extraction and wavelength calibration as well as flux calibration take place. To get rid of skyline emissions, also a sky subtraction is performed in this step. In the second phase, a 3D data cube is constructed. Here, astrometry is used to calculate the on-sky position of each fiber and produces a pixel grid with respective sizes of 0.5" from IFU geometry and dither offsets. Each pixel or better spaxel (spatial pixel) contains a spectrum resulting in a 3D data cube (x, y, λ).

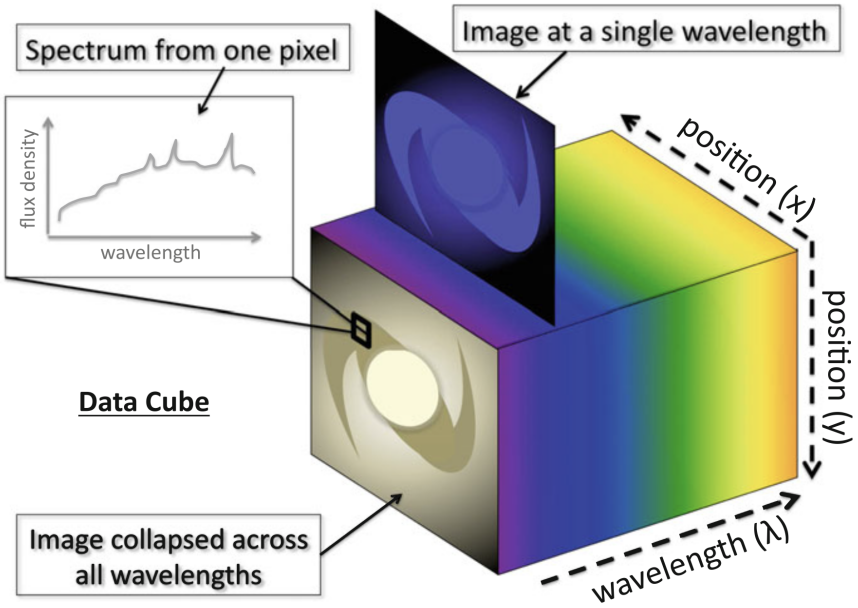

Figure 8. Illustration of a data cube taken from Harrison 2014. It provides information in two spatial dimension and a third dimension of wavelength. At each spaxel of the datacube a spectrum can be extracted and at any wavelength an image of the target can be obtained.

The resulting data cubes are visualized in figure (8) and are called LOGCUBES be-

cause the wavelengths are logarithmically resampled in order to have linear velocity spacing of the spaxel. The LOGCUBES can be downloaded for a specific Plate-IFU number which corresponds to the used plate number followed by the number of fibers used in the IFU with an extra number 01-04 corresponding to the different IFU with the same number of fibers. In this thesis I will refer to the galaxies by their Plate-IFU number, which is not unique for each galaxy, since some galaxies were observed more than one time. Each galaxy has a unique associated MaNGA ID.

3 Methods

In the process of finding kinematic signatures for fossil AGN outflows, many methods and techniques have to be applied. These include a technique to measure kinematic elevation that suggests an AGN outflow and comparison to the stellar kinematics, SFR in the galaxies, identification of the non-AGN galaxies and more. Not all methods described here were performed directly in this thesis but were used to obtain the processed data I will work with and therefore it is important to know how this data was derived.

3.1 [OIII] line as AGN outflow tracer

To trace the energetic outflows of AGN, this thesis makes use of the [OIII] line but also other permitted and forbidden emission lines in the optical spectrum. In this section, I will shortly discuss their origin and how they can be fitted and then used as a kinematic outflow tracer.

3.1.1 Permitted and forbidden emission lines

Permitted emission lines have high transition probability and therefore very short decay times by photon emission ($\approx 10^{-8}\,\mathrm{s}$). Therefore, they are produced both in high-density environments like the BLR with electron density $n \gtrsim 10^{8}\,\mathrm{cm}^{-3}$ and low-density environments. Two permitted lines that will be referred to in this thesis, are the Balmer lines $H\alpha(\lambda = 6563\,\text{Å})$ and $H\beta(\lambda = 4861\,\text{Å})$ often referred to as recombination lines (Osterbrock and Ferland 2006). They are produced by transition from a higher principle energy level, $n = 4$ for $H\alpha$ and $n = 3$ for $H\beta$ to the level $n = 2$. In emission line regions, where enough photons with ionizing Energy $h\nu \geq 13.6$ eV exist, electrons constantly get removed and recombined with hydrogen nuclei in an excited state. From here they cascade down the energy levels, emitting the recombination lines.

Forbidden emission lines on the other hand, have lower transition probability from their meta-stable states and therefore longer decay times. So they emit photons only in less dense environments when they do not get collisionally de-excited by another particle before photon emission. In general, forbidden emission lines are depicted in square brackets. The [OIII] species is twice-ionized oxygen (O^{2+} in chemistry notation) and requires a high energy source to produce the required photoionizing photons with $h\nu \geq 35.1$ eV. The [OIII] line is actually a line doublet [OIII]$\lambda\lambda$4959,5007 created by movement in orbitals and changing of spin of the two electrons in the outer $2p^2$ sub-shell. The transitions of [OIII] in the energy-level diagram can be seen in figure (9). Because of their transition probabilities, the flux ratio of the [OIII]λ5007 and the [OIII]λ4959 line is theoretically set to 2.98 (Dimitrijević et al. 2007). The collisionally excited state $^1D_2$ shown in figure (9) gets de-excited by collisions before it can produce a photon in high density environments

with $n_e \gtrsim 7 \cdot 10^5\,\mathrm{cm}^{-3}$ (Osterbrock and Ferland 2006). This is why they cannot be found in the BLR of AGN.

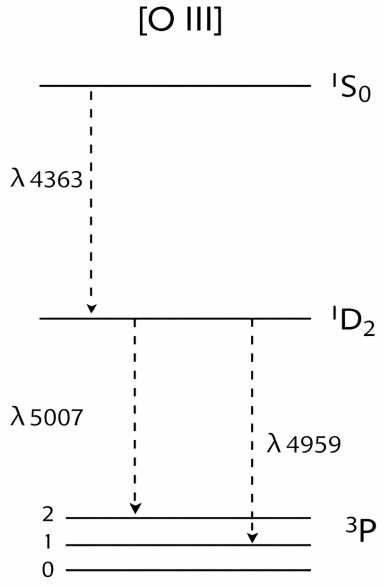

Figure 9. Energy-level diagram for transitions of strong optical emission lines by de-excitation of [OIII]. The energy level difference of the ^3P lines has been exaggerated.

3.1.2 Non-parametric line measurements

The structure of an emission line is generally dominated by complicated velocity projections onto the LOS with an often negligible contribution of thermal line broadening, especially for heavier elements. Deviations from a Gaussian profile are presumably due to a different gas component or outflow whose three dimensional velocity is projected on the LOS creating broader wing components. To account for these broader components the lines are fitted with two Gaussian curves and non-parametric values based on percentages of the total integrated flux are used to describe the line properties (Liu et al. 2013; Zakamska and Greene 2014). The measurements base on the comulative flux $\Phi(v)$ as a function of velocity:

$$\Phi(v) = \int_{-\infty}^{v} F_v(v')dv'. \tag{9}$$

Here the velocity v is referred to as the velocity caused by the non-relativistic doppler broadening $\Delta\lambda/\lambda = v/c$. The wavelength is converted into a rest wavelength frame λ_{rest} with the systemic redshift of the galaxy z_{sys} and now v can be calculated with the rest

wavelength λ_0 of the emission line such that:

$$\lambda_{rest} = \frac{\lambda}{1 + z_{sys}} \qquad \Rightarrow \qquad v = c\frac{\lambda_{rest} - \lambda_0}{\lambda_0}. \tag{10}$$

The conversion of the flux density over wavelength $F_\lambda(\lambda)d\lambda$ into the velocity dependent flux density $F_v(v)dv$ has to be taken into account:

$$F_\lambda(\lambda)d\lambda = F_v(v)dv. \tag{11}$$

With the comulative flux, the total line flux is given by $\Phi(\infty)$ and the LOS velocity v_{med} by $\Phi(v_{med}) = 0.5\Phi(\infty)$ which is the velocity that bisects the total area under the emission line profile. Most importantly, the line width W_{80} that encloses 80 per cent of the total flux can be defined over the difference between the velocities at 10 and 90 per cent of the comulative flux:

$$W_{80} = v_{90} - v_{10} \tag{12}$$

with $\Phi(v_{90}) = 0.9\Phi(\infty)$ and $\Phi(v_{10}) = 0.1\Phi(\infty)$. The double Gaussian fit compared to a single Gaussian emission line fit and an illustration of the line width W_{80} is shown in figure (10).

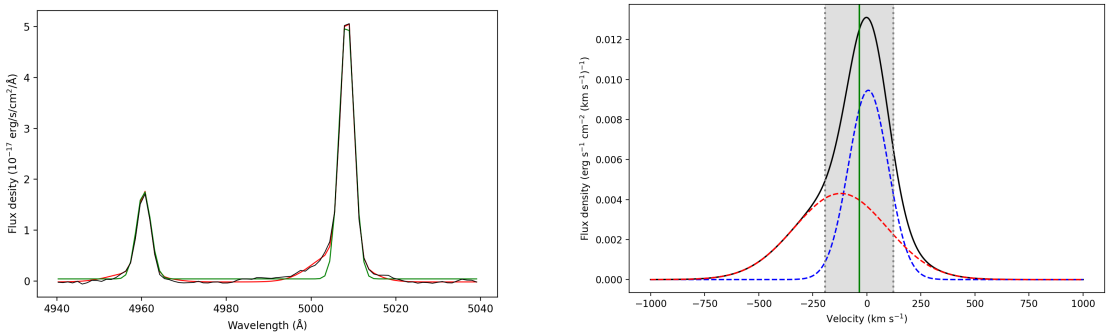

Figure 10. On the *left side* an example fit of a spaxel in MaNGA galaxy 7443-12703 of the [OIII] line doublet. The observed spectrum after subtraction of the stellar continuum is shown in black, the single Gaussian fit is shown in green and the double-Gaussian fit in red. It can be seen that the red lines provides a better fit to the emission line profile and can therefore retrieve the kinematic properties better. On the *right side* the model profiles are shown in the velocity space for just the [OIII]λ5007 line. The vertical green line marks the LOS velocity. The broad fitted component in red and the narrow component in blue together create the total line fit depicted in black. The shaded grey area represents the W_{80} line width.

In a purely single Gaussian profile, the W_{80} line width is close to the Full Width Half

Maximum (FWHM) of the line:

$$W_{80} = 2.563\sigma = 1.088\,\mathrm{FWHM} \tag{13}$$

but is more sensitive for weaker broader bases of emission lines for non-Gaussian profiles. When mentioning the W_{80} value in this thesis, the [OIII] line W_{80} width is meant, if not stated otherwise.

3.1.3 [OIII] line W_{80} as tracer of AGN ionization

As established above, the forbidden [OIII] line originates in the NLR surrounding the AGN. It can trace the low-density AGN-ionized gas out to several kiloparsecs (Liu et al. 2013; Gatto et al. 2024). It is a strong and easily observed line and suffers relatively little from dust obscuration compared to optical emission in the central region (Heckman and Best 2014) and is therefore widely used as a gas outflow tracer in low- and intermediate-redshift AGN (Liu et al. 2013; Zakamska and Greene 2014; Wylezalek et al. 2020; Dall'Agnol de Oliveira et al. 2021). In particular Wylezalek et al. (2020) showed that two to three times as many MaNGA-selected AGN candidates exhibit enhanced [OIII] kinematics compared to non-AGN. This was determined by how many galaxies in both samples show $W_{80} > 500/800/1000\,\mathrm{km\,s^{-1}}$. The AGN candidates also showed higher mean $\langle W_{80} \rangle$ values over all valid spaxel. Interestingly, they found some sources that have not been selected as AGN and do not have enhanced merger fractions or indicators for SF driven outflows, that show elevated [OIII] kinematics.

But not only high absolute W_{80} line widths are a tracer of AGN outflow but also relative elevation compared to the stellar dispersion. The idea behind a relative elevation of the [OIII] line width relative to the stellar dispersion is that stars are dynamically relaxed over larger timescales and are expected to follow the gravitational potential. Ionized gas on the other hand, is a collisional system and reacts locally to force acting on it, for example in the form of AGN or stellar feedback. In the case of kinematic disturbance from outside the galaxy or recent/ongoing galaxy merger events, both systems get disturbed and it is no longer possible to distinguish between kinematic disturbance from AGN activity and from external influences. This is adressed in section (6.1). Studies showed that stellar dispersion $\sigma_\star$ is dynamically hotter (larger) than ionized gas dispersion σ_{gas} for star forming galaxies with rising $\Delta\sigma = \sigma_{gas} - \sigma_\star$ when AGN emissions are present (Oh et al. 2022; Ilha et al. 2019). For a large sample of $\sim 39,000$ type 2 AGN at $z < 0.3$ Woo et al. (2016) found the [OIII] velocity dispersion for AGN with double Gaussian [OIII] line profiles to be on average 1.3-1.4 times larger than the stellar velocity dispersion and relative elevation of the gas dispersion can therefore be used as an AGN outflow tracer.

3.2 Stellar continuum fitting

When working with galaxy spectra it is essential to perform a stellar continuum fit in order to retrieve stellar kinematics such as the stellar LOS velocity $v_\star$ and the stellar velocity dispersion $\sigma_\star$. The stellar continuum is also needed to be subtracted from the total spectrum in order to perform emission line fitting and can be used to determine the SFR history in the galaxy. As mentioned above, the stellar kinematics will also be used as a measure for the relative gas outflow.

3.2.1 Penalized pixel fitting

Penalized pixel fitting (`pPXF`, Cappellari and Emsellem 2004; Cappellari 2016) models the observed galaxy spectrum $G_{mod}(x)$ after quality masks and masking the emission lines that do not originate from stars with:

$$G_{mod}(x) = \sum_{k=1}^{K} w_k [B * T_k](x) + \sum_{l=0}^{L} b_l \mathcal{P}_l(x) \qquad\qquad w_k \geq 0. \tag{14}$$

The sum over w_k is a linear combination of stellar templates T_k that will be touched on in section (4.1), convoluted with the broadening function $B(x) = \mathcal{L}(cx)$. $\mathcal{L}(v)$ is the line of sight velocity distribution which comes from the doppler broadening which affects the stellar light in the LOS similar to the emission lines. The convolution accounts for this broadening in the templates. In the `pPXF` routine $\mathcal{L}(v)$ is given by:

$$\mathcal{L}(v, \sigma, h_m) = \frac{1}{\sigma\sqrt{2\pi}} e^{-\frac{(v-V)^2}{2\sigma^2}} \left[1 + \sum_{m=3}^{M} h_m H_m \left(\frac{v-V}{2\sigma}\right)\right]. \tag{15}$$

This is a Gaussian LOSVD extended with Hermite polynomials H_m weighted with h_m, which originate from the derivative of a Gaussian function and can therefore model small derivations from a Gaussian profile well. The linear combination of Legendre polynomials $\mathcal{P}_l(x)$ aim to compensate for any subtle mismatch between the spectral templates and the science spectra that change slowly with wavelength arising for example from calibration errors or internal or foreground reddening (Westfall et al. 2019). The model is fit to the spectrum, minimizing χ^2 but adding a penalty term when the fit deviates too much from a Gaussian shape to avoid overfitting on too noisy or complex spectra. The result is a spaxelwise fitted stellar continuum and the best fitting parameters for the stellar kinematics.

3.2.2 Simple stellar population modeling

To retrieve information about the star formation history, one cannot simply use normal stellar templates but model the spectrum of a galaxy with a combination of simple stellar populations (SSP). A SSP is a spectrum of a population of stars that have the same age, same initial metallicity and follow the same initial mass function (IMF) which is the initial distribution of stellar masses on the main sequence. To construct a SSP, three ingredients are needed. First, the stellar evolution theory in the form of isochrones is needed. An isochrone is a curve on the Hertzsprung-Russel diagram which depicts the stars luminosity against its effective temperature, representing a population of stars with the same age but different initial masses. Different populations with different ages result in a different isochrone. Secondly, for each point, so for different masses on the isochrone, an associated stellar spectrum is needed. This spectrum can be observationally or theoretically created. Lastly, each spectrum needs to be weigthed by the initial mass function and a SSP model is created (Conroy 2013).

If many SSP are combined in a similar way as the stellar templates for the `pPXF` fitting an observed galaxy stellar continuum can be modeled and with the also known mass to light ratios M/L for each SSP the SFR history over a chosen time interval can be reconstructed.

3.3 AGN selection techniques

This work focuses on finding fossil AGN signatures and therefore galaxies without a currently active galactiv nucleus are analyzed. So, in order to focus on the AGN signatures in non-AGN galaxies, first the AGN in the sample have to be identified. Because of both differences in intrinsic AGN properties (such as the differences in accretion rate, black hole mass, obscuration of the BH and the strength of the radio jet) and the relative strength of the light from the host galaxy, it is not possible to probe only one property or wavelength regime for AGN signatures to identify all AGN. As established in section (1.1) the AGN have a largely spread SED and therefore multiwavelength approaches can be used to distinguish between AGN emissions and those produced by other processes like ongoing star formation, existing stellar populations or hot insterstellar gas (Alexander et al. 2025). Combining these methods, the AGN selection is aimed to be as complete as possible because every selection method has its caveats.

Here, a short summary of the selection techniques that are performed by the catalogs used in this thesis will be given. For a more systematic overview of the selection techniques, see for example Padovani et al. (2017).

3.3.1 Optical AGN diagnostics

The high-quality spectra of optical spectroscopic surveys like the Sloan Digital Sky Survey (SDSS, York et al. 2000) make the detection of Type I AGN possible through their easily detactable broad-emission lines and strong non-stellar continuum which is evidence for AGN activity.

For those galaxies that show no broad emission lines, it was discovered that the relative intensities of strong forbidden and permitted emission lines differ for different ionization sources (Baldwin, Phillips, and Terlevich 1981; Veilleux and Osterbrock 1987). Stronger high-exitation emission-lines such as [OIII] indicates a "harder" ionizing continuum than seen from the "softer" continuum of O stars associated with on-going star formation (HII regions) and therefore imply AGN activity. The three used so-called BPT diagrams are depicted in figure (11) for the SDSS main galaxy sample. The separation of the strictly star forming galaxies and the AGN population is primarily done in the [OIII]λ5007/Hβ vs. [NII]λ6584/Hα ([NII] BPT) whereas the [SII]$\lambda\lambda$6714,6731/Hα ([SII] BPT) and [OI]λ6300/Hα ([OI] BPT) line ratios are used to separate AGN from LINERs. Here line pairs that are close in wavelength are used to reduce the effects of dust reddening which could affect the measurements of the emission line ratios (Kennicutt Jr. 1992).

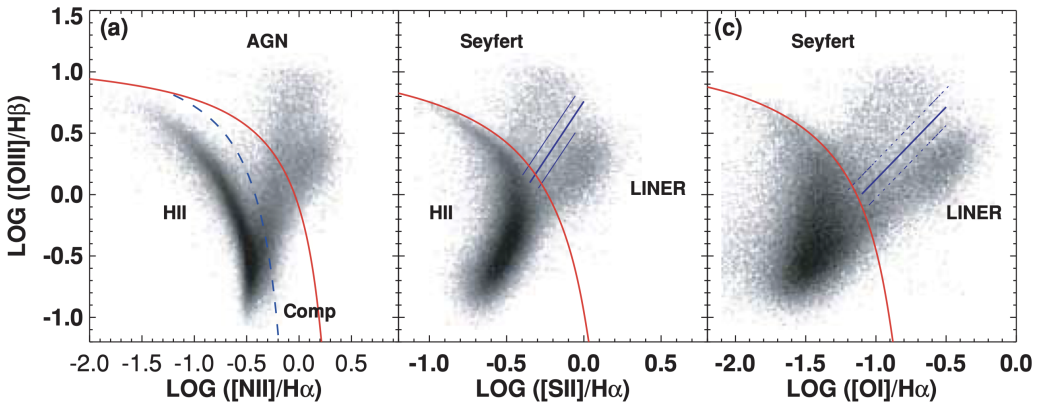

Figure 11. The three used BPT diagrams taken out of Kewley et al. (2006) for the SDSS main galaxy sample. The red demarcation line is the theoretical maximal starburst line from Kewley et al. (2001) while the blue dashed line shows the empirical separation of pure star-forming galaxies and AGN by Kauffmann et al. (2003b). Between the two lines lies the composite region. The blue line in the middle and right panel separating the higher ionized AGN from the lower ionized LINER by Kewley et al. (2006).

To further tackle the problem that LINERs with the weakest emission lines are probably not powered by an AGN (Cid Fernandes et al. 2011) the extra criterion of the equivalent width of the Hα line $W_{H\alpha} > 3$ Å is often superimposed. The equivalent

width:

$$W_\lambda = \left| \int \frac{F_c - F_s}{F_c} d\lambda \right| \tag{16}$$

is a measure of the strength of the spectral feature F_s compared to the underlying continuum intensity F_c.

Alternatively or in addition another diagnostic diagram, The WHAN diagram that takes these difficulties into account is applied (Cid Fernandes et al. 2011). Using only the stongest optical lines Hα and [NII] it can be done for galaxies with lower quality and also shows the population of passive galaxies that show no or only weak emission lines.

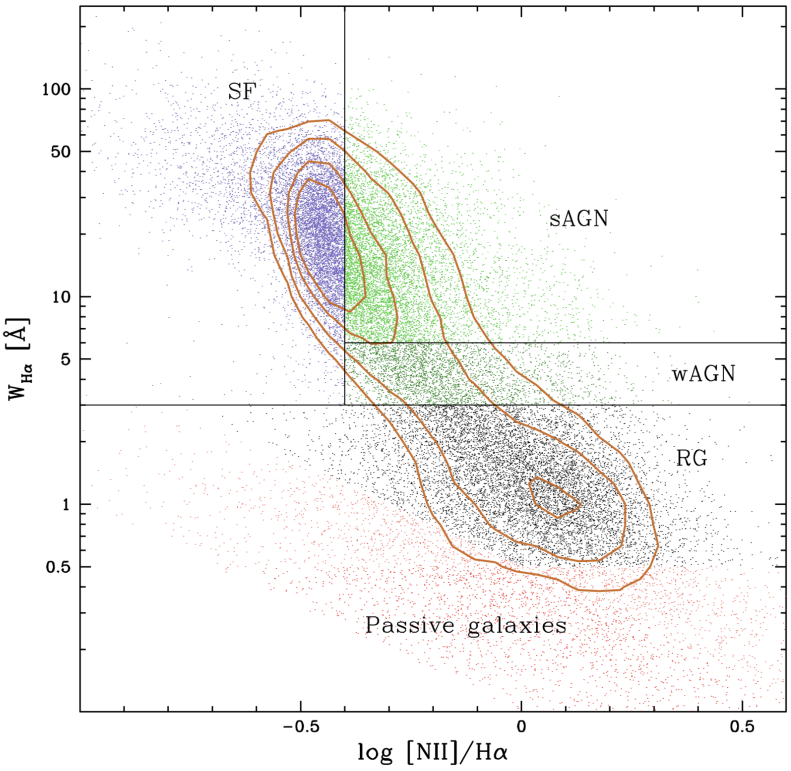

Figure 12. The WHAN diagram with classified galaxies of the SDSS main galaxy sample taken from Cid Fernandes et al. (2011). The vertical line represents the optimal transposition of the Kauffmann et al. (2003b) line and the horizontal line dividing sAGN (strong AGN) and wAGN (weak AGN) the optimal transposition of the Kewley et al. (2006) line into the $W_{H\alpha}$ vs. [NII]/Hα plane. Deviding again star forming galaxies from AGN and Seyferts (here sAGN) from LINER (here wAGN). The LINER are further divided from the retired galaxies (RG) which are "fake" AGN.

A similar diagram, the WHAD diagram that uses only the Hα line was proposed by Sánchez et al. (2024). Here the W_λ is plotted against the Hα line disperion $\sigma_{\mathrm{H}\alpha}$. It makes use of the different ionization sources producing different velocity disperions. While SF ionization is associated with lower velocity dispersions (Law et al. 2022), harder ionization by AGN in the NLR and shock ionization by galaxtic winds produce higher velocity

dispersion. Retired galaxies are distinguished in the same way as in the WHAD diagram by their lower Hα equivalent width and can produce a wide range of velocity disperions. This is because their ionization comes from hot-evolved stars which are typically found in bulges or thick disks with higher $\sigma_{\mathrm{H}\alpha}$. The diagram also divides weak and strong AGN with respectively lower and higher W_λ but adds an unknown region at lower $\sigma_{\mathrm{H}\alpha}$ and intermediate W_λ between the SF and the retired region.

The caveats for optical diagnostics in general are that optical emission lines can be substantially affected by dust absorption, shocks and diffuse ionized gas regions (Kewley, Nicholls, and Sutherland 2019).

3.3.2 Radio AGN selection

Radio emissions present a good indicator for AGN activity as the majority of radio luminous objects in the sky are AGN sources. In this wavelength regime galaxies are believed to be dominated by synchrotron radiation, often referred to as non-thermal radiation emitted from relativistic particles accelerating in magnetic fields (see Rybicki and Lightman (1985) Chapter 6). In AGN synchrotron emissions originate in powerful radio jets that range from kpc to Mpc scale. Those Radio-AGN described in section (1.1) will not be selected as AGN at any other wavelength as the bulk of their energy is contained in those radio loud jets (Merloni and Heinz 2007). Here, it needs to be distinguished from the synchrotron radiation produced by SF for example from relativistic electrons accelerated by supernovea.

In this thesis I will adopt a selection independent of radio-loud or radio-quiet classification and whether or not they have a jet. With more sensitive radio surveys it is clear that there is a large overlap region between the two classififcations and AGN are never really radio-quiet (Padovani et al. 2017). It is possible to construct an AGN sample independent of optical diagnostics and other selection techniques. Kauffmann, Heckman, and Best (2008) showed that there is a tight correlation between the Hα luminosity which is a SFR tracer and the radio 1.4 GHz flux density for a sample of SF galaxies. Similarly, AGN can be identified over the excess of SFR estimated from the radio luminosity, assuming that all radio emission is related to SF processes, compared to the Hα-based SFR.

The advantage for ground based radio observations is the fact that the earths atmosphere is transparent to several decades of radio frequency from $\sim$ 10 MHz to $\sim$ 1 THz. Since radio frequencies are larger than the typical dust grain sizes in the ISM it is less affected and travels better through interstellar gas and dust.

3.3.3 Infrared AGN signatures

The dusty torus described in the unified model of AGN absorbs optical/UV light and re-emitts it in IR wavelength peaking around $15 - 60\,\mu$m which falls in the Mid Infrared

(MIR) regime (Mullaney et al. 2011). This reflects the typical temperature of the dust of ~ 100 K. Dust emission from ongoing SF is likely to dominate in the Far Infrared (FIR) regime at typically lower temperatures $\lesssim 40$ K.

I will focus on detection methods by all sky observations in four mid-infrared bands (3.4, 4.6, 12, 22 μm denoted W1, W2, W3 and W4 respectively) from the Wide-field Infrared Survey Explorer (WISE, Wright et al. 2010). The AGN detection is done with color-color diagrams of photometric magnitudes in the observed bands because AGN occupy different spaces on the diagram compared to for example SF galaxies (Wright et al. 2010). For WISE, Assef et al. (2013) developed a selection method using only the simple color indicator W1-W2. If it is bigger than a set threshold it indicates the presence of an AGN which exhibits a power law spectrum with higher flux at higher wavelengths. Only the coolest brown dwarfs or the most heavily dust-reddened stars will exhibit such red WISE colors (Stern, Assef, and Benford 2012).

Tracing the emission of the dust itself, infrared selection is immune to obscuration effects and is able to identify heavily obscured populations that are missed by other selections. But the amount of dust in AGN show a significant variance with some AGN showing little to no obscuring material (Padovani et al. 2017 Chapter 3 and references therein) or dilution from the host galaxy resulting in bluer color making less luminous AGN not longer identifiable (Stern, Assef, and Benford 2012).

3.3.4 X-ray AGN signatures

X-ray emissions are likely produced by inverse compton scattering of UV photons from the accretion disk by a hot compact corona. It creates a X-ray continuum ranging from 10^{-1} to $\sim 10^2$ keV (Barger 2004). Harder X-ray ($\gtrsim 10$ keV) is relatively immune to photoelectric absorption and can therefore be used as an AGN selection method. Especially as other galactic sources such as X-ray binaries or supernova remnants are relatively weak compared to the AGN in the X-ray regime. In the compton thick regime with higher gas column densities, even hard X-rays cannot penetrate without being compton scattered (Alexander et al. 2025).

3.4 Clustering algorithms

When regions with elevated kinematic signatures are found, we have to make sure that the detection is above our reachable resolution and is not only caused by noise detection that has been spread out on the CCD. To group regions that lie over the resolution limit, I make use of two grouping and clustering algorithms.

3.4.1 DBSCAN

The Density-Based Spatial Clustering of Applications with Noise (DBSCAN, Ester et al. 1996) is, as the name suggests, a density based clustering algorithm. Objects or points at high density get clustered, separated through regions with lower object density. Unlike other partitioning cluster methods like the k-means-algorithm or hierarchial clustering methods, no fix number of clusters has to be set in the beginning and it can deal with noise. So, it only detects clusters if special requirements are fulfilled and categorizes the data points as follows:

(i) Core Points: points that have a minimal required number of other points (MinPts) to build a dense region within a set distance (ε) which is the minimal distance between two points to be considered neighbors.

(ii) Border Points: points within the distance ε but that do not have MinPts as neighbors.

(iii) Noise Points: points that are neither Core points nor Border points and are not included in any cluster.

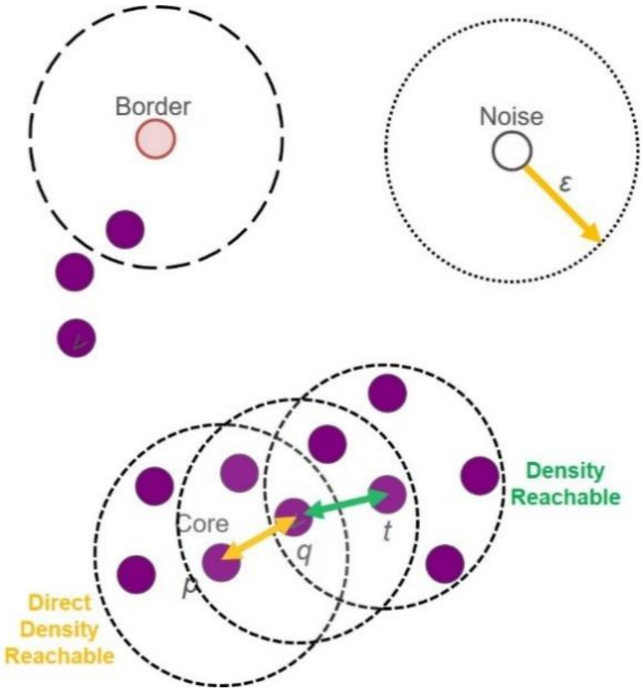

Figure 13. An illustration of the core concepts of the DBSCAN algorithm. Here MinPts = 4 was chosen. The figure is taken from Giacoumidis et al. (2019).

The core concept to build a cluster is *density connectivity* and *density reachability*. Point t is density reachable from core point p if it is possible to step through a chain of

core points with steps $< \varepsilon$. The points p and t are density connected, if there exists a point q, from where p and t are density reachable. A cluster is built if the number of points exceeds MinPts and they are density connected. An illustration of the clustering algorithm is shown in figure (13).

This algorithm poses the possibility, apart from being able to detect noise, to cluster regions together that show a high density of elevated signatures but that are not necessarily directly connected. However, a downside is that if the elevated signatures form a narrow structure that is longer than the resolution limit, the algorithm will not properly detect it because it does not form a dense region. A discussion of these advantages and disadvantages will be done in section (5.3).

3.4.2 Connected component labeling

To overcome the missing detection of these narrow structures, also the Connected Component Labeling (CCL, Zuo and Zhang 2023) algorithm is implemented. In its simplest form, it simply extracts spatially connected regions. I will use 8-connectivity where diagonal components are considered connected as well. When using spaxel, spatially connected means sapxel that share a border or edge. To group objects together, a minimal number of connected objects MinPts also need to be found.

3.5 Kendall τ test

To measure whether two properties show a correlation, a statistical correlation test is needed.

The Kendall τ test (Kendall 1949) is a nonparametric measure of rank correlation. A rank correlation is a statistic that measures the relationship between rankings of ordinal variables. The test measures the number of concordant to disconcordant pairs of observations weighted by the total number of pairs. A pair of observations (x_i, y_i) and (x_j, y_j) with $i < j$ is concordant if both $x_i > x_j$ and $y_i > y_j$ or both $x_i < x_j$ and $y_i < y_j$. Kendall's τ ranges from $-1 \leq \tau \leq 1$ with positive coorelation meaning $\tau > 0$. For independent non constant random variables $\tau = 0$ is expected.

A significant correlation between the properties is assumed if the p-value, which is the probability that the null hypothesis that the the properties show no monotonic correlation, is low ($p < 0.01$).

4 Used Processed Data

Now that the importance of the [OIII] line to analyze the outflow kinematics is established, I will summarize how the [OIII] line fitting was performed and where the data is taken from. This section will first touch on the data of the stellar continuum fitting because it is used for the [OIII] line fitting and also the origin of the SFR maps. Of course, this section also includes a multiwavelength AGN sample obtained with the selection techniques explained above.

4.1 MaNGA Data Analysis Pipeline

The official MaNGA Data Analysis Pipeline (Westfall et al. 2019; Belfiore et al. 2019) that analyzes the data produced by the DRP uses `pPXF` to fit the stellar continuum. The fit is done in two iterations, first masking the emission lines and performing a `pPXF` fitting only up to moments h_3 and h_4 and in a second iteration fitting the emission lines and the stellar continuum simultaneously while keeping the stellar kinematics fixed. The emission line profiles modeled by a single Gaussian from DAP will not be used for the [OIII] line analysis in this thesis. For the stellar templates they used the `MILES` stellar library (Sánchez-Blázquez et al. 2006; Falcón-Barroso, J. et al. 2011) with 985 stellar spectra. After performing a hierarchial clustering in which they grouped similar spectra together, they were left with 42 different templates to reduce the computation time that they refer to as the `MILES-HC` library. Using them for the `pPXF` yields a good result for stellar kinematics but not for stellar-population properties such as the SF histories.

To achieve a good fit on the data with high enough signal to noise ratio (SNR) especially at larger distances from the galaxy center, where the light drops, Voronoi binning (Cappellari and Copin 2003) is performed. This a spatial binning method that groups spaxel with lower SNR as a set threshold together to increase their SNR with the consequence of loosing spatial resolution. The threshold for the SNR that was reconstructed in the g-band, was chosen to be $\mathrm{SNR}_g = 10$. But since the spatial resolution that is limited by the PSF FWHM is typically larger than the spaxel (0.5" x 0.5") there exists a significant covariance in adjecent pixel. When accounting for this covariance the number of spaxel needed to reach the target SNR_g dramatically increases. This is shown in figure (14).

The stellar velocity dispersion returned by the `pPXF` σ_{obs} is:

$$\sigma_{obs}^2 = \sigma_\star^2 + \delta\sigma_{inst}^2 \tag{17}$$

where $\sigma_\star$ is the true stellar velocity dispersion and $\delta\sigma_{inst}$ is an effective difference in the instrumental dispersion of the template and MaNGA data. For this difference, a first-order estimate is given in a separate extension.

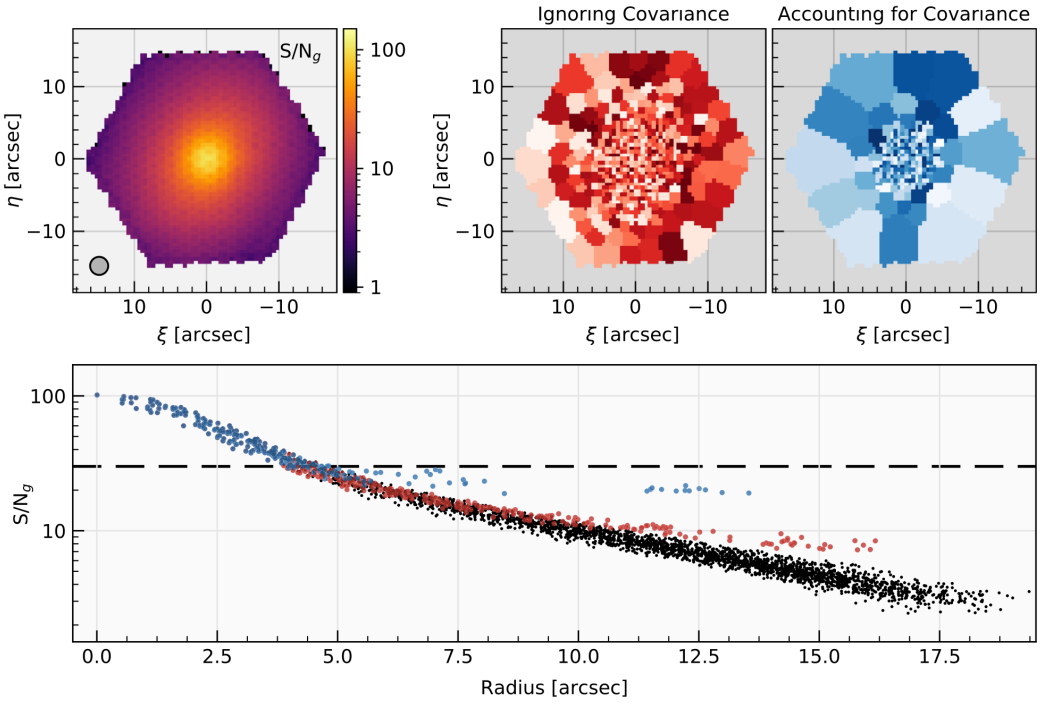

Figure 14. Display of the effect of spatial covariance on the results of the Voronoi binning algorithm. This illustration is done for data cube 8249-12705 and with a SNR_g threshold of 30 to accentuate the effect. The *top-left panel* shows the SNR_g measurements. The *top-middle panel* and the *top-right panel* shows the Vornoi bin distribution without and with accounting for covariance respectively. The different colors are only used to differentiate between spaxel in a given bin. It can be seen that in the center at higher SNR almost no spatial resolution is lost. The *bottom panel* shows the formally correct SNR_g as a function of radius for the individual spaxel (black), the bins derived assuming no covariance (red), and the bins that include the covariance (blue). Without acoounting for covariance the Voronoi algorithm expects the red data to have SNR above the chosen threshold but the formally correct SNR is way below. It is noted that for higher radii the formally correct SNR for the binning that includes covariance also falls short. The figure is taken from Westfall et al. (2019).

Resulting products from the DAP are LOGCUBES with the fitted stellar continuum and emission lines but also MAPS of stellar kinematics and emission line fluxes and more. An example output is shown in figure (15)

4.2 [OIII] line fits

The [OIII] line fits are taken from Albán et al. (2024). They produced maps of the line fit properties of a single and double Gaussian fit to the [OIII] doublet to account for the asymmetric shape of the emission lines that is not captured well by a single Gaussian fit. In a first step, they subtracted the stellar continuum provided by the DAP from the spectra in each pixel and moved them to the rest frame. To account for any additional continuum contribution that is left, a 1D polynomial is fitted to two spectral windows left and right from the [OIII] doublet and subtracted from the entire spectral window

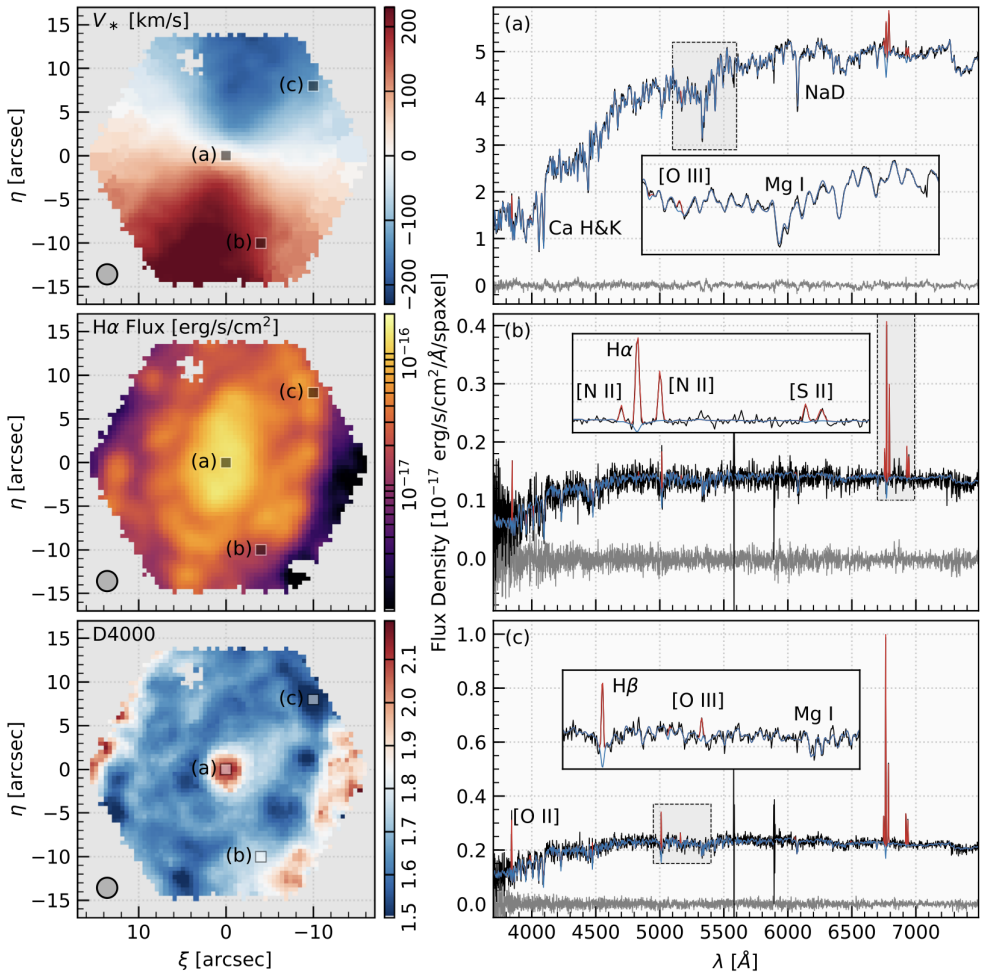

Figure 15. Example data output from the DAP for galaxy 8138-12704. In the *left column* from top to bottom the maps of stellar velocity, the Hα flux and the spectral break index D4000, which is a proxy for stellar population age, are shown. At each panel the grey circle in the bottom left corner shows the effective PSF FWHM$\sim$ 2".5. The spectrum for the highlighted spaxel with a), b) and c) are shown in the *right column*. Each spectrum panel shows the observed MaNGA spectrum (black), stellar-continuum-only model (blue), and best-fitting (stars + emission lines) model (red); the residuals between the data (black) and the model (red) are shown in gray. Inset panels show a spectral region highlighted with the grey box in more detail. The figure is taken from Aguado et al. (2019).

(6920 − 5080 Å in the rest frame) where the line fitting will be performed. Now the Gaussian function:

$$G(x; A, \mu, \sigma) = A \cdot exp(-\frac{(x-\mu)^2}{2\sigma^2}) \tag{18}$$

with expected rest frame position of the emssion line x in Å is fitted simultaneously to the [OIII] line doublet for which same kinematics are assumed . Therefore, the offset from the restframe position μ and the dispersion σ are taken as equal and with known flux ratio of the doublet of 2.98 (Dimitrijević et al. 2007) only three free fitting parameters are

left. Equally, for the second fit with two Gaussians, only six free parameters are fitted. It is imortant to take into account that all SDSS data, including MaNGA, are stored at vacuum wavelengths, which shifts the position of the emission lines by some Å. Following the convention I refer to the emission lines by their air wavelengths as done in section (3.1.1). For details of the constraints placed on the parameters, see Albán et al. (2024).

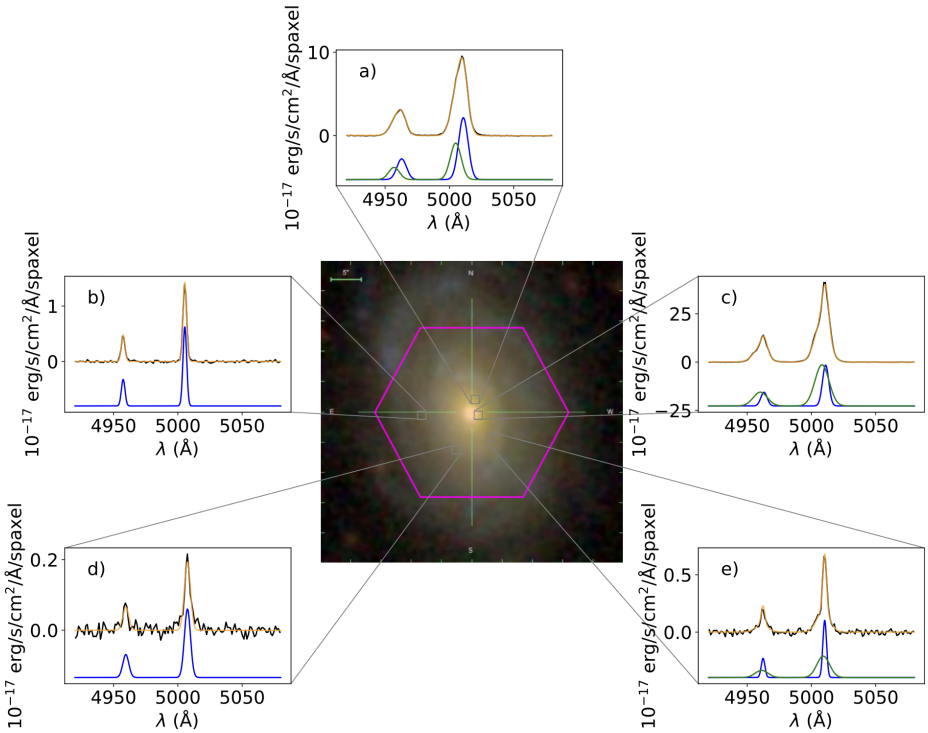

Figure 16. Visualization of the fitting procedure for galaxy 8993-12705. The *central panel* shows the SDSS composite *gri* optical image of the galaxy with the magenta hexagon showing the region probed with the IFU. *Panels a) to e)* show the spectral window of the [OIII] line doublet for different spaxel. The black line shows the original residual spectrum with subtracted stellar continuum and the yellow line shows the fit. With an offset in the y-axis the blue and green lines show the sub-components of the fit. If there is no broad green component present, the single Guassian fit was chosen to be the best model by the described selection algorithm. The figure is taken from Albán (2022).

The resulting parameters of the individual Guassians for just the [OIII]λ5007 line, which are the integrated flux and the LOS velocity offset (μ in velocity space), and the velocity dispersion, are saved in two separate extensions together with their reduced χ^2_{red}. For the fit with two Gaussian moments, the nonparametric W_{80} and v_{med} for the whole fit is also saved. In a third extension, the [OIII]λ5007 line signal quality is saved. This is provided by the DAP in the form of an amplitude of the line over noise ratio (A/N). The Noise is measured over the root mean square of spectral windows in the residual spectrum around the emission line. Given the tight correlation of the SNR corresponding to the flux and flux error and the A/N (Belfiore et al. 2019) I will refer to it as the SNR.

To decide whether the single or double Gaussian fit is used for the final W_{80} map that is being analysed, the model whose χ^2_{red} is closer to 1 is used. To prevent noise fitting, an additional criterion that discards the two-Gaussian model if the second component has a SNR < 3 is implemented. For spaxel with $\mathrm{SNR}_{[\mathrm{OIII}]} < 3$ no fit is performed at all. This combination of the two W_{80} maps to a combined map, saved in an extra extension (W80_BEST) is shown in figure (17) and figure (16) shows a visualization of the fitting procedure.

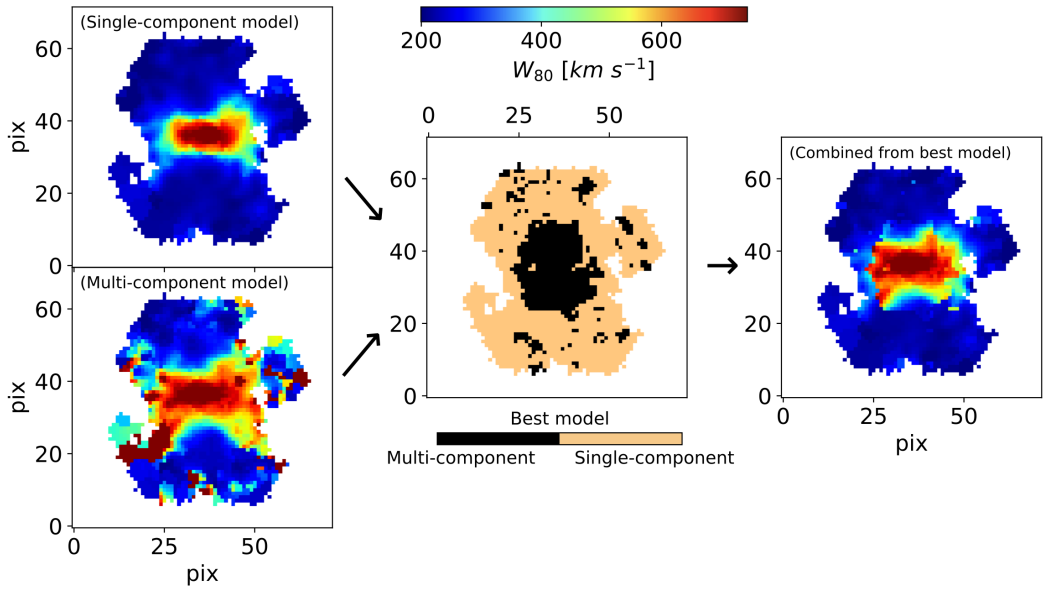

Figure 17. Illustration for the algorithm to choose the best model for the final W_{80} map. The maps are for the same MaNGA galaxy 8993-12705 as in figure (16). The *Left panels* show the W_{80} maps of both fitted models and the *central panel* indicates regions where which model is chosen by the selection algorithm. In the *right panel* the combined best model is shown. The figure is taken from Albán (2022).

4.3 MEGACUBES

The MEGACUBES by Riffel et al. (2023a) provide spaxel-by-spaxel stellar population fits for all MaNGA galaxyies as well as emission line profile fits for all spaxel.

The stellar population fits were done using `MILES` SSP models where the observed stellar continuum was fitted in a similar way as done for the stellar templates in `pPXF`. The differences are that each SSP template spectra is multiplied by a term that accounts for dust absorption and for the LOSVD a simple Gaussian distribution $G(v_\star, \sigma_\star)$ is used without the Hermite polynomials. So, the best fit is chosen with minimizing χ^2 without adding a penalty term. To account for the AGN featureless continuum, a power law term was added $F_\nu \propto \nu^{-1.5}$ so that the model is also reliable for a galaxy where the AGN has a

greater effect on the host galaxy. With the SSP fits, many SFR maps over different time intervals were created.

Emission line fitting was done for the most prominent lines and fitted with a single Gaussian curve. In this work, I will use the MEGACUBES fits of the [SII]$\lambda\lambda$6716,6731 doublet to calculate electron densities.

4.4 AGN sample

The multiwavelength AGN catalog that will be used here totaling 967 AGN is comprised of an optical emission-line-based catalog from Albán and Wylezalek (2023), a broad-line-based catalog from Fu et al. (2023), a mid-infrared-selected catalog and a X-ray-selected catalog from Comerford et al. (2024) and a catalog of radio-selected AGN from Albán et al. (2024). As some AGN are identified by multiple selection methods, a table listing overlapping targets across the catalogs is provided in table 2.1 in Albán et al. (2024), who use the same total AGN catalog for their analysis of ionized gas kinematics in AGN. A complete catalog of 970 AGN after removing double observations is reported there and the discrepancy of 3 AGN may come from the different selection of the multiple observed galaxies. They select the Plate-IFU, which had more available annuli with higher SNR when measuring their W_{80}. In the following, the used catalogs will be presented in more detail.

Optical line diagnostics AGN catalog

This catalog presented by Albán and Wylezalek (2023) uses the BPT line diagnostics diagram to detect AGN in the full MaNGA sample. The AGN were selected if they fall in the Seyfert or LINER region in both the [NII] and [SII] BPT. To minimize the contamination of "fake" AGN the additional cut of $W_{H\alpha} > 3\,\text{Å}$ is used. The authors used different apertures for the classification and I will use the catalog with an aperture of 2 kpc that keeps the balance between the physical extent of the NLR and the MaNGA spatial resolution ($\sim$ 1.37 kpc, Wake et al. 2017) and identifies 399 AGN.

Broad-Line AGN catalog

Fu et al. (2023) present a broad line AGN catalog of 139 AGN that show broad Hα lines originating from the unobscured BLR of Type-1 AGN. They first identified galaxies where the DAP model fit failed with high flux residual from the model fit compared to the actual flux data. They quantified this by first dividing all MaNGA galaxies in 20 SNR bins according to their mean G band weighted SNR. Then they selected all galaxies with residuals $> 1\sigma$ of the residual distribution at each SNR bin and performed a multicomponent gaussian fitting for these galaxies. They were selected as Broad-line AGN if the emission line width σ of the broad component is at least $600\,\text{km}\,\text{s}^{-1}$ larger than the emission line width of the narrow component.

Mid-infrared and X-ray AGN catalogs

Both catalogs are described in Comerford et al. (2024) who crossmatched AGN candidates from multiwavelength surveys. The Mid-infrared catalog comprises 130 AGN and is based on the color indicator from WISE. From 105-month X-ray all-sky (50% in the 14-195 keV band) observations with the Burst Altert Telescope (BAT, Barthelmy et al. 2005) on board the Swift observatory there were 30 AGN crossmatches of the entire Swift-BAT catalog (Oh et al. 2018) with the MaNGA galaxy sample (Comerford et al. 2024).

Radio AGN catalog

The radio-selected AGN catalog is taken from Albán et al. (2024) and comprises 642 galaxies. They used the excess of SFR estimated from the radio luminosity from crossmatched data from the radio surveys NRAO Very Large Array Sky Survey (NVSS Condon et al. 1998) and Faint Images of the Radio Sky at Twenty centimeters (FIRST, Becker, White, and Helfand 1995) to the Hα based SFR from integrated properties in the PIPE3D value added catalog (Sánchez et al. 2022). To avoid only the selection of radio loud AGN a low radio flux cut of > 1 mJy ($1\,\mathrm{Jy} = 10^{-23}\,\mathrm{erg\,s^{-1}\,Hz^{-1}\,cm^{-2}}$) is enforced, which is close to the sensitivity of the surveys.

Resolved BPT AGN catalog

Another optical line diagnostics AGN selection method will be used as a reference but will not be included in the AGN sample. This selection method, developed by Wylezalek et al. (2018), makes use of the spatially resolved BPT diagrams and classifies galaxies as AGN if a fraction of all spaxel in the [NII] and [SII] BPT diagrams fall into the AGN/composite or AGN/LINER region. It therefore also detects galaxies that lack central AGN emissions and might be hidden behind large column densities in the center, off-nuclear AGN or relic AGN. To deal with contamination that mimic AGN-like signatures of photo-ionized gas, a set of additional selection criteria are used. These are a cut on the Hα equivalent width to exclude ionization from pAGB stars and a cut on the Hα surface brightness, which is the flux per area, to exclude regions ionized by diffuse ionized gas, especially in the outskirts of the galaxy. They also excluded galaxies, their spaxel lie too close to the SF demarcation line to account for uncertainty in the demarcation line and contamination of hot young stars with high SFR. Because this selection was only performed for 2727 galaxies from the MaNGA product launch 5, the classification of Jaison et al. (in preparation) will be used, who performed this method for the total MaNGA sample of DR17. In addition to the BPT diagrams, they also use the WHAN and WHAD diagrams for the spatially resolved AGN selection.

5 Search for fossil outflow candidates

Now I want to describe the search for fossil outflow candidates in the SDSS MaNGA galaxies. The data analysis was performed in Python. To handle the flexible image transport system (FITS) file format, in which most astonomical data is saved, the `astopy` (The Astropy Collaboration et al. 2013, 2018, 2022) package is used. Other used packages are `matplotlib` (Hunter 2007) to plot and visualize the data, `numpy` (Harris, Millman, and van der Walt 2020) for calculations and array handling, `scipy` (Virtanen, Gommers, and Oliphant 2020) for fitting, labeling and correlation testing, `pandas` (McKinney 2010) for data handling, and `scikit-learn` (Pedregosa et al. 2011) for clustering.

5.1 Data quality analysis

Before starting the search for fossil outflow candidates the quality of the data sample has to be inspected. As mentioned, some galaxies have been observed multiple times and I want to get rid of the doubles with lower signal and also those galaxies where the DRP gave the galaxy a critical flag because of some problem in the reduction. Most importantly, I also want to assess, at which SNR the [OIII] line fits give reliable parameters because for many galaxies and especially in the outskirts of the galaxies the SNR drops to low values. Here, the risk of fitting noise, resulting in unreliable kinematic parameters is high.

5.1.1 Cleaning of initial sample

First, I get rid of all data from multiple observed galaxies. To do so the `drpall` catalog is checked, which contains information for the MaNGA galaxies like Plate-IFU number ("plateifu" extension), MaNGA-ID ("mangaid" extension), redshift ("Z" extension) and also DRP flags ("drp3qual" extension). Since the MaNGA-ID is unique for one galaxy, the Plate-IFU numbers from observations with the same MaNGA-ID can be checked and those with fewer spaxel with SNR > 7 can be discarted. This SNR cut is discussed in the next section. To ensure completeness, I perform the same selection for the selection of multiple observations reported in the appendix of Albán et al. (2024). Next, galaxies with a CRITICAL flag by the DRP are removed. It indicates a critical failure in the reduction, such as bad astrometry or calibration. There is also a caveat, where some unique galaxies have different MaNGA-IDs so these doublicates together with galaxies from the Coma, IC342, M31, and globular cluster ancillary programs are excluded. Also, three Plate-IFUs had no data stored on them (11939-1901, 11949-1901 and 8626-9102).

In this way from 11273 Plat-IFUs found in the `drpall` 1,265 galaxies are excluded, resulting in an initial unique galaxy sample of 10,008 galaxies. For all of those galaxies, there exist [OIII] line fits (Albán et al. 2024). In the AGN sample, no critical quality was found but some doublicates, resulting in a sample of 967 AGN as reported in section

(4.4). This leaves us with an initial non-AGN sample of 9,041 galaxies.

5.1.2 Signal to noise selection

The SNR has a big impact on the measurement of the W_{80} line width. With decreasing SNR it tends to get underestimated (Liu et al. 2013), especially if a faint broad component is present (Zakamska and Greene 2014). On the other hand, at low SNR the risk of fitting noise which results in bigger line widths rises. To analyze the dependency of the W_{80} best fit measurements on the SNR, the mean and median W_{80} values of all fitted spaxel for all galaxies that pass different SNR cuts are calculated. The curves of W_{80} against the SNR cut were calculated for the initial AGN and non-AGN sample and can be seen in figure (18).

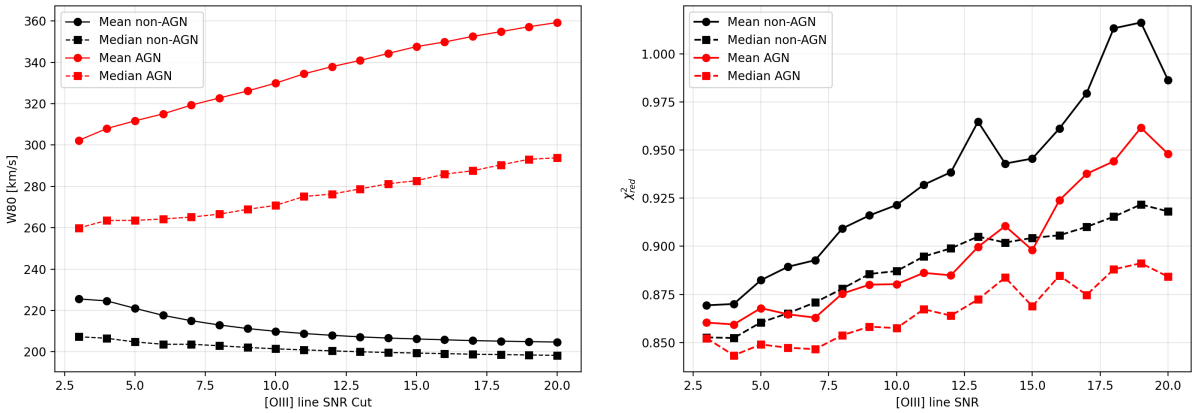

Figure 18. In the *left panel* the W_{80} [OIII] line width as a function of SNR cut is presented. The black curves correspond to the non-AGN sample and the red curves for the AGN-sample. For the solid lines the mean W_{80} value over all remaining spaxel after the SNR cut is depicted and for the dashed lines similarly the median W_{80} value. In the *right panel* the χ^2_{red} of all fits as a function of individual SNR is presented. For the solid lines the mean χ^2_{red} value over all spaxel with the corresponding SNR is depicted and for the dashed lines similarly the median χ^2_{red} value.

For the initial AGN sample, both the mean and median W_{80} value rise with increasing SNR cut, while for the non-AGN sample they fall with increasing SNR cut. The rise for the AGN sample may be explained by a better fit of the broad component with increasing SNR and therefore higher line widths. The big gap between the mean, which is more sensitive to outliers at high values and the median indicates many kinematically elevated regions, which is expected for AGN. Because elevated kinematics in AGN can be found especially in central regions where SNR is typically much higher, the W_{80} values rise with increasing SNR cut as well. The inverse trend for the non-AGN sample may be explained by fitting noise at regions with low SNR, which results in higher W_{80} values. As the SNR cut increases, including only spaxel with higher signal, the median approaches the limit of spectral resolution. This is expected because typical neutral and molecular gas

dispersions in nearby galaxys lie far below the spectral resolution limit (Mogotsi et al. 2016). When observing the χ^2_{red} values for the [OIII] line best fits at individual SNR, a mean and median $\chi^2_{red} < 1$ over all spaxel can generally be seen, which is a sign of overfitting (figure (18)). It indicates too large errors or noise to evaluate whether our model is a good fit. This reinforces our picture of possible noise fitting at lower SNR values. With increasing SNR, χ^2_{red} rises as well towards the desired $\chi^2_{red} = 1$.

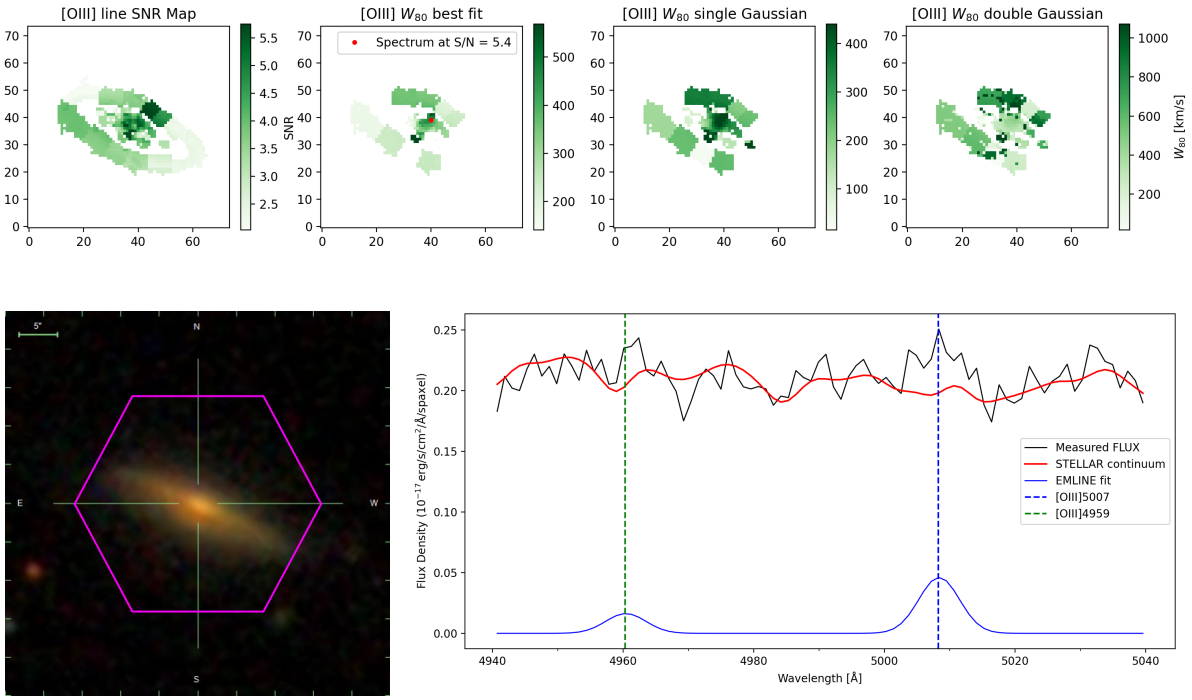

Figure 19. The *top panel row* are from left to right the spaxel maps of the [OIII] line SNR, the [OIII] W_{80} best fit map, the [OIII] W_{80} single Gaussian fit map and the [OIII] W_{80} double Gaussian fit map of galaxy 9036-12702. The *bottom left panel* shows the SDSS *gri* composite image and the *bottom right panel* the [OIII] doublet rest frame spectral window of the in red highlighted spaxel in the W_{80} best fit map. The black line corresponds to the measured flux from the DAP cubes "FLUX" extension, the red line to the DAP cubes stellar continuum fit from the "STELLAR" extension and the blue line to the DAP emission line fit from the "EMLINE" extension. The dashed blue and green vertical lines correspond respectively to the [OIII]λ5007 and [OIII]λ4959 rest frame position. Here it can be seen, that the high W_{80} best fit values come from noise fitting in the SNR ≈ 5 regime.

It is important to note that with rising SNR cut, less and less galaxies are still included from our initial 9,041 galaxies. At the SNR > 5 cut 7,370 galaxies are left with at least one spaxel showing SNR over this cut and at SNR > 9 almost twize as many are excluded with only 5828 non-AGN galaxies left. So I want to set the SNR cut as low as possible in order not to exclude too many galaxies because the focus lies on not excluding possible fossil outflow candidates. To further inspect the reliability of the [OIII] line fits in the $5 <$ SNR < 7 regime, individual fits to spaxel that show elevated W_{80} values in many

galaxies with SNR in this regime are visually inspected. This can be seen in figures (19), (20) and (21). The emission line fits visualized there are from the DAP but showcase the extended width because of noise fitting as seen in the fits by Albán et al. 2024 well.

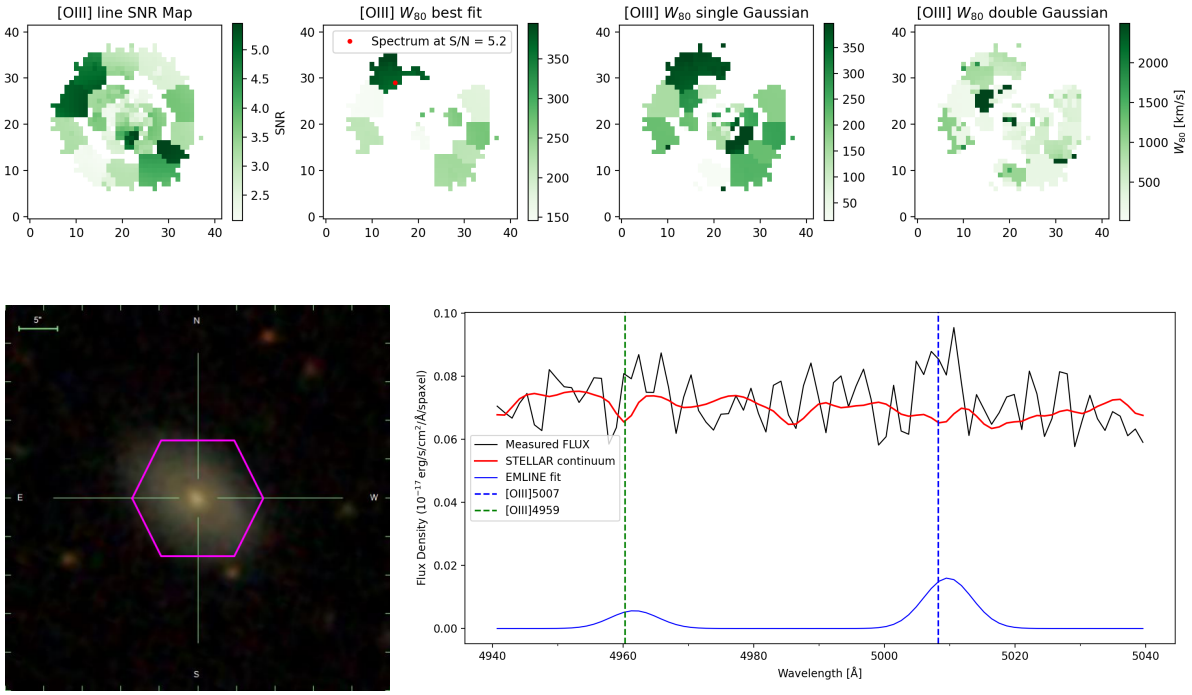

Figure 20. Same panels as in figure (19) for galaxy 8994-3704. Here it can be observed again that the high W_{80} best fit values is a result of noise fitting in the SNR ≈ 5 regime.

The SNR cut is chosen to be SNR > 7 to balance a reliable fit but also not to exclude too many galaxies. Now 6,499 non-AGN galaxies are left with at least one spaxel over this cut. Since we recide still at low χ^2_{red} values we have to be careful with the selection results when getting close to the chosen SNR cut.

5.2 Elevated ionized gas kinematics

Now that a non-AGN galaxy sample with suitable quality is found, the selection of kinematically elevated regions in those galaxies that hint towards fossil outflows can begin. To do so, no high absolute W_{80} width cut like Wylezalek et al. (2020) (with $W_{80} > 500\text{km}\,\text{s}^{-1}$) or Gatto et al. (2024) (with $W_{80} > 380\text{km}\,\text{s}^{-1}$) is applied, because fossil outflows can show lower line dispersions than driven ones. Therefore, a low absolute cut combined with a relative cut to the stellar kinematics that points towards non-gravitational motion of the gas is used.

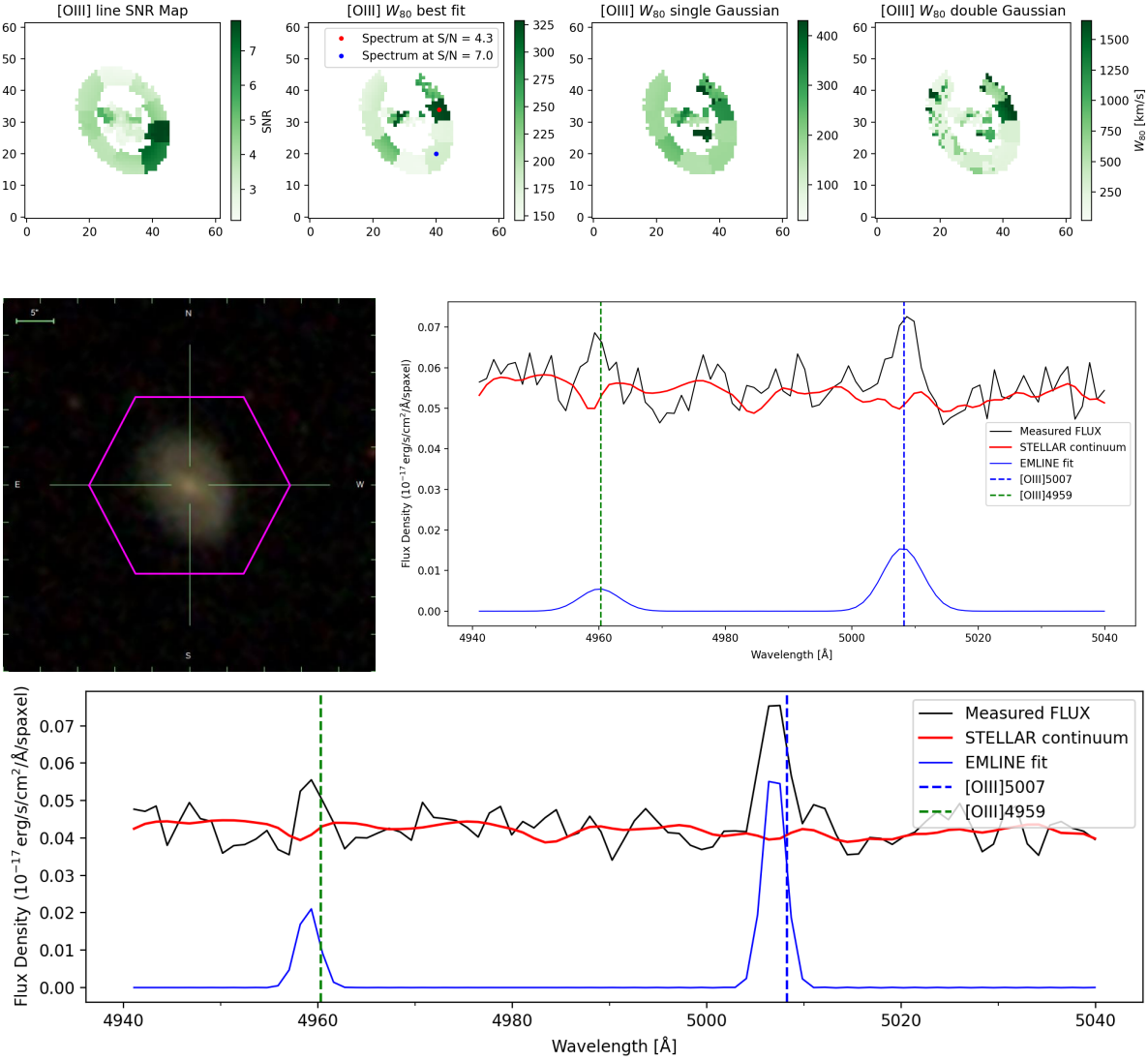

Figure 21. Same panels as in figure (19) for galaxy 8721-9101 with additional spectrum at the bottom of the blue highlighted spaxel in the W_{80} best fit map. Here it can be seen that the emission line fit for the spaxel with SNR = 7 is more accurate than the fit for the spaxel with SNR $\approx$ 4. This trend was confirmed in more visual inspections.

5.2.1 Relative elevation with respect to stellar dispersion

The stellar $W_{80,\star}$ dispersion with which I want to work with, is calculated from the DAP binned stellar kinematic fits ("STELLAR_SIGMA" extension) keeping in mind that $\sigma_\star$ has to be corrected for the instrumental dispersion ("STELLAR_SIGMACORR" extension). I choose the DAP stellar kinematic fits over other fits such as from the MEGACUBES, because it includes binned values, achieving a good SNR even in the outer parts of the galaxy and because those binned fits were also used to subtract the stellar continuum in the [OIII] line fitting by Albán et al. (2024). The quality DAP mask ("STELLAR_SIGMA_MASK" extension) has to be applied for both the [OIII] and stellar W_{80} maps. This reduces the total number of valid spaxel in the non-AGN sample that can be analysed, which pass all quality criteria, from 3,410,934 spaxel to 3,201,292 spaxel.

The fractional cut with fraction of elevation x is defined by:

$$W_{80,[\mathrm{OIII}]} > x \cdot W_{80,\star} \qquad \text{with} \qquad x > 1. \tag{19}$$

So, a spaxel is considered as kinematically elevated if their corresponding $W_{80,[\mathrm{OIII}]}$ is x times higher than $W_{80,\star}$. If this fractional cut is now applied together with the SNR cut to all galaxies in the initial non-AGN sample even with a high fraction of $x = 1.8$ the distribution of elevated values peaks at low W_{80} values close to the spectral resolution ($\sim 180\,\mathrm{km\,s^{-1}}$) as can be seen in figure (22). The same goes for the mean W_{80} per galaxy. Many galaxies have maximal W_{80} values not even surpassing $300\,\mathrm{km\,s^{-1}}$.

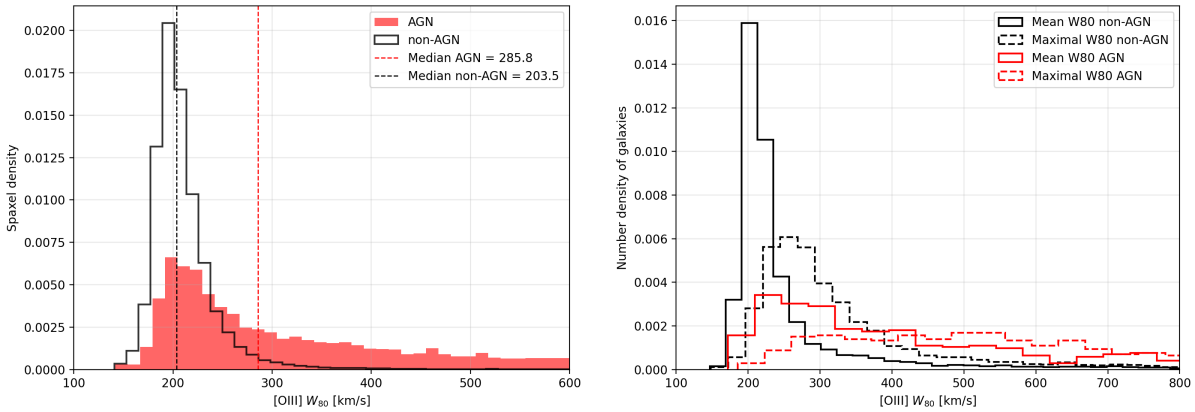

Figure 22. The *left panel* shows the normalized distribution of [OIII] line W_{80} across all spaxel that pass the fractional ($x = 1.8$) and SNR cut. It is normalized to show both the AGN (red) sample and the non-AGN (black) sample in the same histogram. The dotted black and red vertical lines correspond respectively to the median elevated W_{80} values of the non-AGN and the AGN sample. The *right panel* shows in solid lines the normalized distribution of mean [OIII] line W_{80} per galaxy across all galaxys in the respective samples that pass the same cuts. The dotted distributions show the normalized distribution of maximnal [OIII] line W_{80} per galaxy across all galaxys in the respective samples that pass the cuts.

If some galaxies that show the most elevated spaxel according to the defined cuts are

inspected, mostly galaxies are found, where the elevated regions are uniformly distributed in the galaxy. They show none of the expected outflow geometries that are expected from AGN outflows. If those galaxies are checked on SIMBAD, almost all of them are classified as emission line galaxies. That means emission lines from ionized gas are present, which typically indicates feedback either from SF galaxies or from AGN. SIMBAD is an astronomical database operated by the Centre de Données astronomiques de Strasbourg. It provides cross-identifications, basic data, bibliographic references, and measurements for objects outside the solar system. If their ionizing source with the resolved BPT and WHAN diagrams (Jaison et al. in preparation) is checked, almost comletely SF dominated galaxies are found. The W_{80} distributions over all elevated spaxel of those galaxies show that they hardly surpass $300\,\mathrm{km\,s^{-1}}$. Examples for three of those galaxies can be seen in figures (23), (24) and (25).

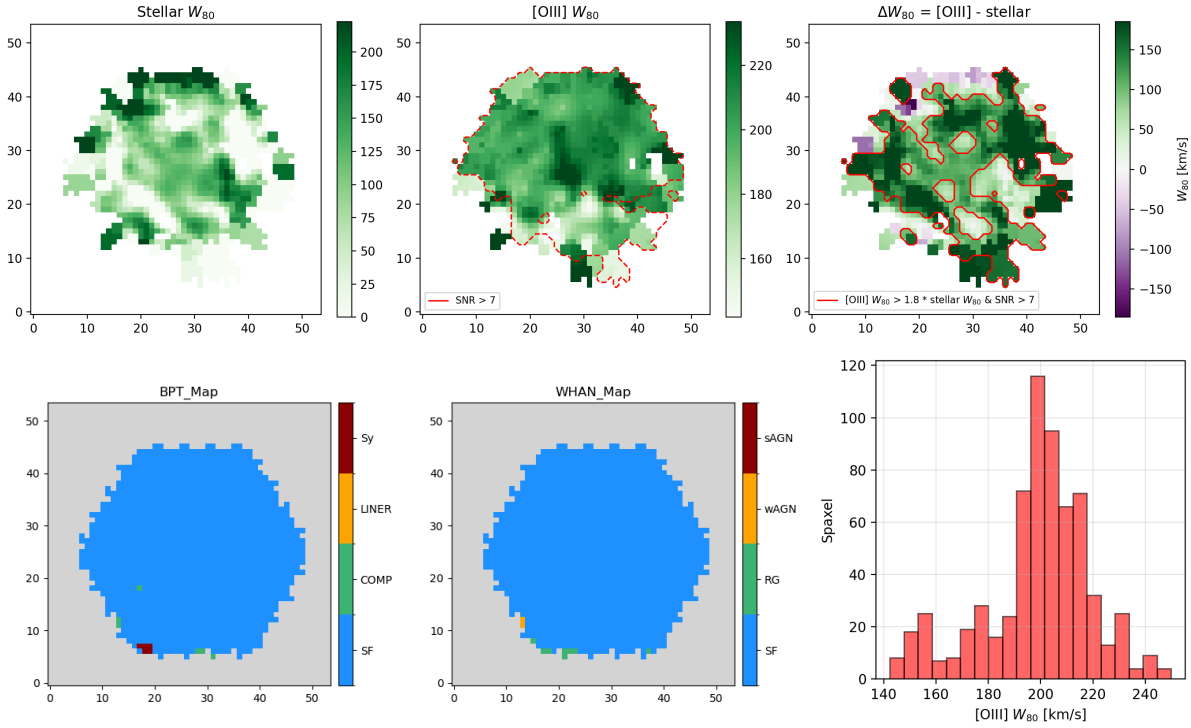

Figure 23. Kinematical elevation for galaxy 9496-6101. The *top panels* show from left to right the stellar W_{80} map, the [OIII] W_{80} map and the residual gas width $\Delta W_{80} = W_{80,[\mathrm{OIII}]} - W_{80,\star}$. The red dashed line in the [OIII] W_{80} map indicates the region with which passes the SNR cut and the solid red line in the ΔW_{80} map the regions that pass the additional fractional elevation cut. The two *bottom left panels* show the resolved BPT and WHAN diagrams (Jaison et al. in preparation) and the *bottom right panel* shows the [OIII] W_{80} distributions over all spaxel in the galaxy. No outflows because of past AGN activity are expected because the emission line diagnostic diagrams show no AGN signatures.

The left panel in figure (26) shows that a significant fraction of all valid spaxel in the non-AGN sample pass this cut. At $x \approx 1.4$ 50% and at $x \approx 2.1$ still 20% of all valid spaxel pass these cuts. In the right panel in figure (26) it can be seen that increasing

x even results in a drop in mean and median [OIII] W_{80} values that pass the cut. The reason for that may be that more spaxel with higher W_{80} values towards the center get dropped where the stellar dispersion is also high. We can conclude that increasing x does not get rid of the many low elevated values that are suspected not to originate from AGN activity. Therefore, an additional absolute W_{80} cut is applied.

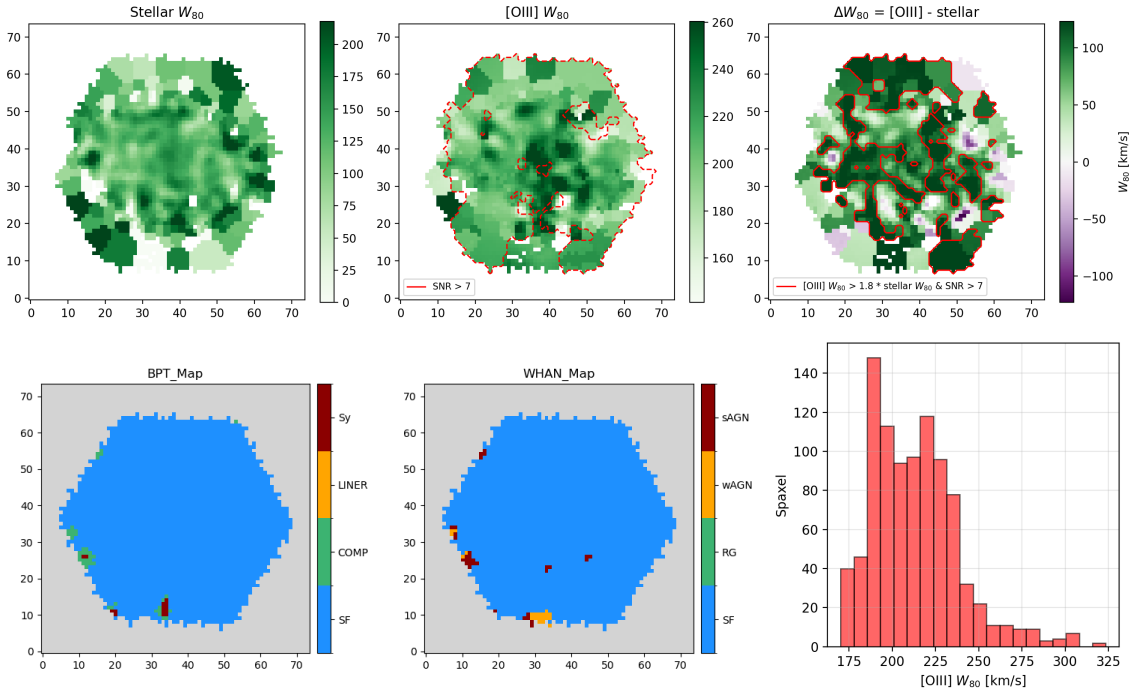

Figure 24. Same as in figure 23 but for galaxy 8568-12705.

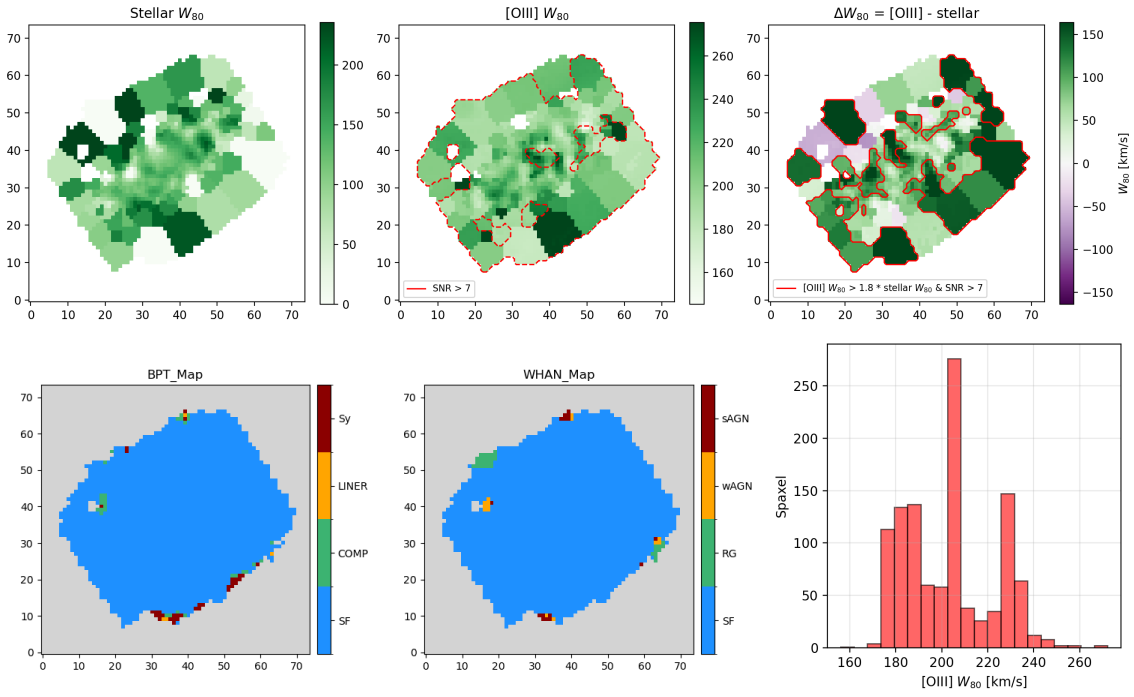

Figure 25. Same as in figure 23 but for galaxy 12510-12701.

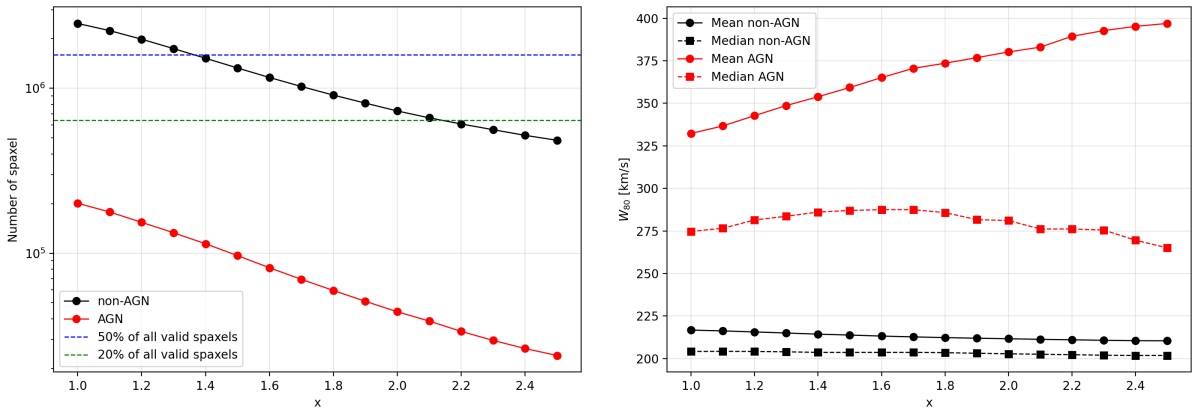

Figure 26. The *left panel* shows the absolute number of all valid spaxel of the non-AGN sample (black) and the AGN sample (red) that pass the fractional and SNR cut. Indicators through dotted horizontal lines for 50% and 20% of all valid spaxel of the non-AGN sample are depicted in blue and green respectively. Note that the number of spaxel is logarithmically spaced. The *right panel* shows mean (solid) and median (dotted) W_{80} values of all spaxel that pass the cuts as a function of the fractional cut x for the non-AGN and AGN sample.

5.2.2 Absolute elevation

In a sample of $\sim$ 160,000 BPT selected SF galaxies with properties $z < 0.7$, $8 < log(M_\star/M_\odot) < 11.5$ and $-3 < log(\mathrm{SFR}/M_\odot \mathrm{yr}^{-1}) < 2$, Cicone, Maiolino, and Marconi (2016) showed that the gas velocity dispersion hardly exceeds a corresponding $W_{80} \sim 380\,\mathrm{km\,s^{-1}}$. Because I do not want to exclude fossil AGN outflows, whose W_{80} lie below this value, a lower absolute cut of $W_{80} > 300\,\mathrm{km\,s^{-1}}$ is implemented since this already excludes most of the galaxies that are suspected not to show relative elevation because of relic AGN activity. But this also means that there is some contamination of highly ionizing stellar feedback. After implementing this absolute width cut, the inspection of the influence of the choice of x on the number of spaxel and W_{80} can be done again. The results are shown in figure (27).

The left panel shows that the absolute number of spaxel that pass all cuts is reduced

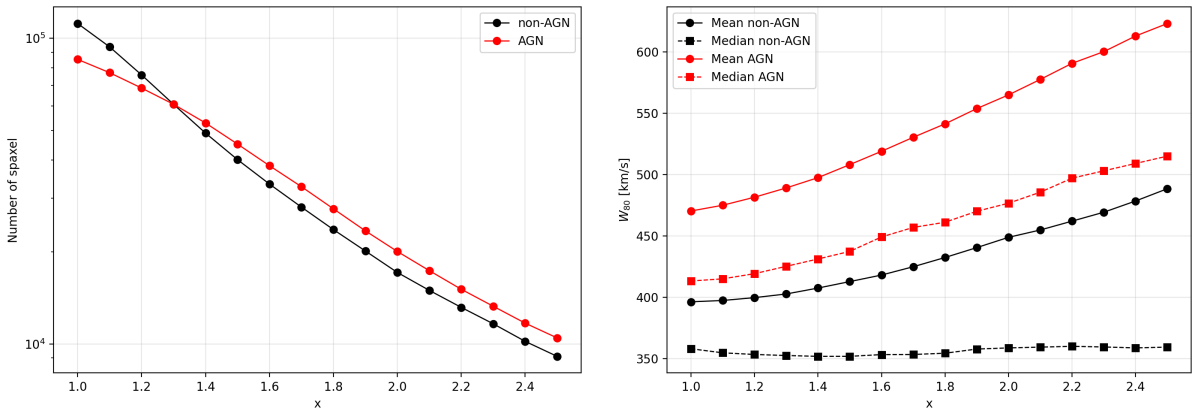

Figure 27. Same as in figure 26 but with additional absolute width cut $W_{80} > 300\,\mathrm{km\,s^{-1}}$.

by over one order of magnitude, being in the same region as the only 526 AGN that pass all cuts (at $x = 1.5$). The median W_{80} value does not rise significantly with x for the non-AGN sample unlike the AGN sample, because there are still many elevated values close to the absolute cut. However, an increase in the mean W_{80} can be seen, which is more prone to outliers in the right panel, which indicate that those low elevated values do not completely suppress the selection. Balancing again not to exclude to many galaxies but assuring a high enough fractional cut, I choose $x = 1.5$. At this x value 97.0% of spaxel from non-AGN galaxies that are considered elevated without the absolute width cut are excluded whereas only 53.4% of spaxel from AGN galaxies are excluded. The so far implemented criteria select 2,835 galaxies from the initial non-AGN sample, showing at least one spaxel that has kinematically elevated gas signatures.

5.3 Clustering of elevated regions

In the next step, I want to make sure that the detected kinematically elevated regions are not only a result of noise detection. Therefore, the spatial resolution that is achieved by MaNGA (median 2.54") is used which only has a standard deviation of 0.12" among the initial non-AGN galaxies. Because this translates to a large spread of physical distances at different galaxy redshifts, I want to discuss the choice of the minimal resolved region and the subsequent clustering in this section.

5.3.1 Choice of minimal resolved region

The spatial resolution in arcsec, in the form of the reconstructed PSF FWHM which includes all spatial limiting factors, is an output of the DRP and can be extracted from the header of the LOGCUBES. The r-band PSF FWHM ("RFWHM" in the header) is used since the [OIII] line recides in this regime. The physical extent of the PSF FWHM $d_{\mathrm{PSF,kpc}}$ from the PSF FWHM in arcssec θ can be calculated with simple trigonometry using the small angle approximation:

$$\theta_{\mathrm{PSF}} = \frac{d_{\mathrm{PSF,kpc}}}{D_A(z)} \tag{20}$$

with the angular distance D_A (6) and the redshift z from the `drpall` file. A close to linear relationship between $d_{\mathrm{PSF,kpc}}$ and the redshift of the galaxy can be observed (see figure (28)). The physical resolution limit ranges from $\sim 0.5\,\mathrm{kpc}$ to $\sim 7\,\mathrm{kpc}$ depending on z with most of the galaxies in the sample reciding in the lower redshift end. This introduces a bias towards galaxies with lower redshift, since a bigger physical extent $d_{\mathrm{PSF,kpc}}$ for galaxies is needed that have a larger distance $D_A(z)$ from us to lie over the spatial resolution limit.

To select galaxies that have kinematically elevated regions, we need to know the minimal number of spaxel in this region for it to be over the spatial resolution limit. Making

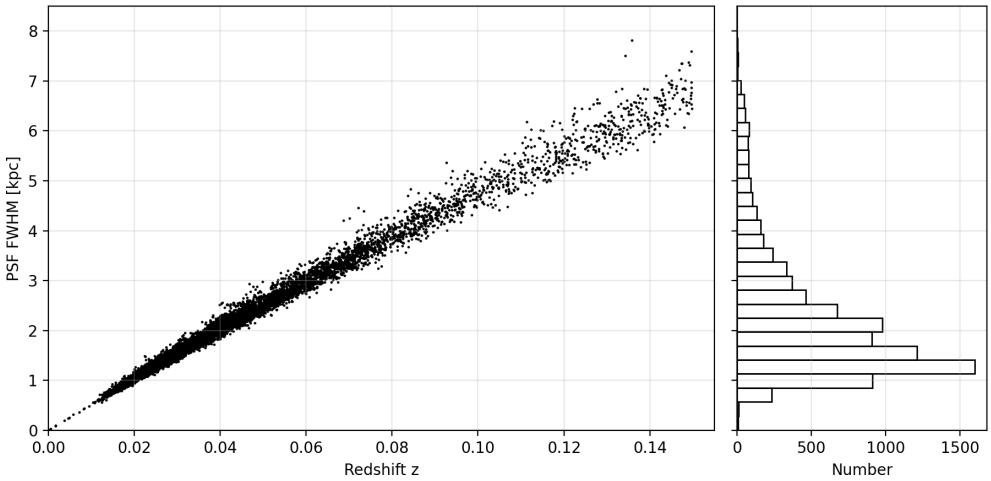

Figure 28. Dependence of the physical extent of the PSF FWHM on the redshift of the galaxies in the initial non-AGN sample. The distribution of the PSF FWHM in kpc in the *right panel* shows that most galaxies have spatial resolution of $\sim 1-2\,\mathrm{kpc}$ and recide at lower redshifts.

use of the spaxel spacing, where 1 px width corresponds to 0.5", the minimal number of spaxel MinPts that lie in a circular area with radius $d_{\mathrm{PSF,px}}/2$ can be calculated. The value is then rounded up to the next integer. Here $d_{\mathrm{PSF,px}}$ is the extent of the PSF FWHM in pixel, calculated from the individual reconstructed PSF FWHM in arcsec. In this way perfectly circular kinematically elevated regions are detected and if they deviate from a circular shape, the minimal number of spaxel still ensures a sufficiently dense region, that is not only a small filament with length over $d_{\mathrm{PSF,px}}$. Since MinPts only depends on the PSF FWHM in arcsec that does not show a large deviation, it varies from MinPts = 14 for a minimal achieved PSF FWHM ≈ 2.14" to MinPts = 32 for the maximal PSF FWHM ≈ 3.19" and takes a mean value of MinPts = 19.7.

If a fixed physical extent of the spatial resolution at the median redshift $d_{\mathrm{PSF,kpc}} = 1.8\,\mathrm{kpc}$ would be selected to account for the bias towards galaxies with lower z there would be more problems. For galaxies with low redshift with actual physical PSF FWHM $\approx 0.5\,\mathrm{kpc}$ real $\sim 1\,\mathrm{kpc}$ outflow regions would be rejected but regions for galaxies at higher regshift with actual physical PSF FWHM $\approx 4\,\mathrm{kpc}$ would falsly be accepted. Therefore, a bias towards higher redshift galaxies would be introduced which also becomes clear when comparing the MinPts for lower and higher redshift galaxies. For galaxies at $z = 0.01$ MinPts = 226 would be needed with fixed $d_{\mathrm{PSF,kpc}} = 1.8\,\mathrm{kpc}$ which is sometimes even over the total number of valid spaxel in the galaxy, whereas only MinPts = 2 at $z = 0.15$ would be needed. So I will stick to the variable $d_{\mathrm{PSF,kpc}}$ method, since it uses the actual spatial resolution.

5.3.2 Applying clustering

First, I want to focus on grouping the kinematically elevated spaxel with the DBSCAN clustering algorithm and later complete it with the CCL algorithm. Only spaxel that show kinematic elevation are included and all other spaxel will be ignored by the clustering algorithms. The minimal number of spaxel MinPts to build a dense region that will be recognized as a cluster is already discussed above and now the minimal distance ε of two points to be considered neighbors is determined. ε has a lower limit because if ε is chosen too low, no initial core point can be set, which has MinPts $= 32$ (upper range) neighbors within the radius ε. So the lower limit for ε, when only perfectly dense circular regions are detected, is:

$$\text{MinPts} = \pi\varepsilon^2 \qquad \Rightarrow \qquad \varepsilon \geq \sqrt{\frac{32}{\pi}} \approx 3.2. \tag{21}$$

If I want to allow regions that are not perfectly circular, but can be elongated and distorted, a higher ε needs to be chosen. In figure (29) it is illustrated how the size of the clustered region varies with different choices of ε. For this galaxy MinPts $= 25$, which gives us a minimal $\varepsilon = 2.9$. It can be seen that at 2.9 the connected region is not sufficiently dense that the density reachability through core points connect all the elevated values. Moving up in ε, it can be observed that more and more of the connected region is clustered and even some extended, not connected points are included.

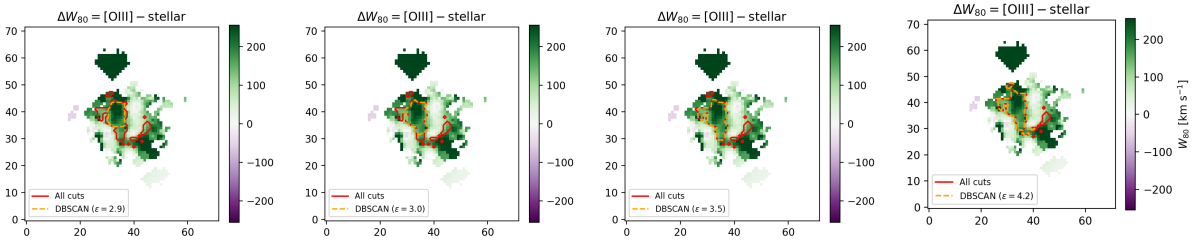

Figure 29. Residual ΔW_{80} map of galaxy 8610-12703 with varying ε. The red contours show the elevated regions selected by the SNR cut, the relative W_{80} cut and the absolute W_{80} cut and the orange dashed contour shows the clustered region by the DBSCAN algorithm. ε takes the values 2.9, 3.0, 3.5 and 4.2 from left to right.

Because the region of kinematic elevation sometimes forms a thinner, less dense region or is cut for example from the SNR cut in a thinner region in some cases, the DBSCAN algorithm does not recognize it as a dense cluster. Therefore, I use the CCL algorithm, which groups the elevated spaxel if it detects MinPts elevated spaxel with 8-connectivity, to include some galaxies that would not have been selected with DBSCAN. Two examples of such galaxies are shown in figure (30). The CCL algorithm detects 357 galaxies with MinPts connected kinematically elevated spaxel.

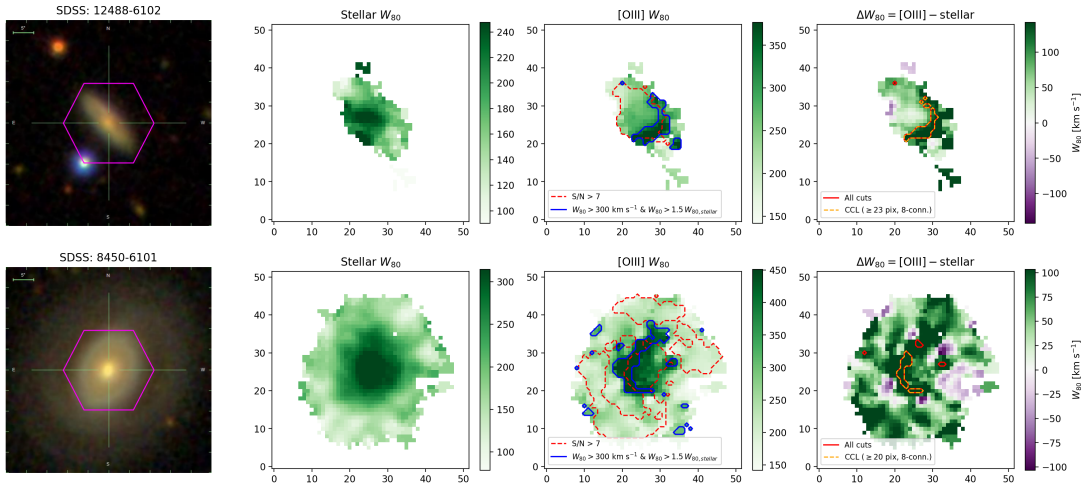

Figure 30. Two examples of galaxies, that have only been selected with the CCL algorithm. The *top panel row* shows from left to right the SDSS *gri* composite image of galaxy 12488-6102, the stellar W_{80} map, the [OIII] W_{80} map and the residual ΔW_{80} map. The red dashed contours in the [OIII] W_{80} map represent spaxel that pass the SNR cut and the blue contours the spaxel that pass the relative and absolute elevation cuts. In the residual ΔW_{80} map all regions can be seen that pass all cuts in solid red contours and clustered region by the CCL algorithm in dashed orange. The *bottom panel row* shows the same panels but for galaxy 8450-6101. This galaxy appears in the resolved BPT AGN catalog of Jaison et al. (in preparation) but not in the BPT catalog of the central 2 kpc by Albán and Wylezalek 2023 and would have been rejected by only using the DBSCAN algorithm. In both galaxies there are regions that seem to be disconnected and still recognized by the CCL algorithm. This is due to the conturing, that rounds the spaxel edges. The regions are connected over the spaxel corners. In the case of 8450-6101 it would not have been detected with 4 connectivity, because here the elevated region connected in this way would be too small.

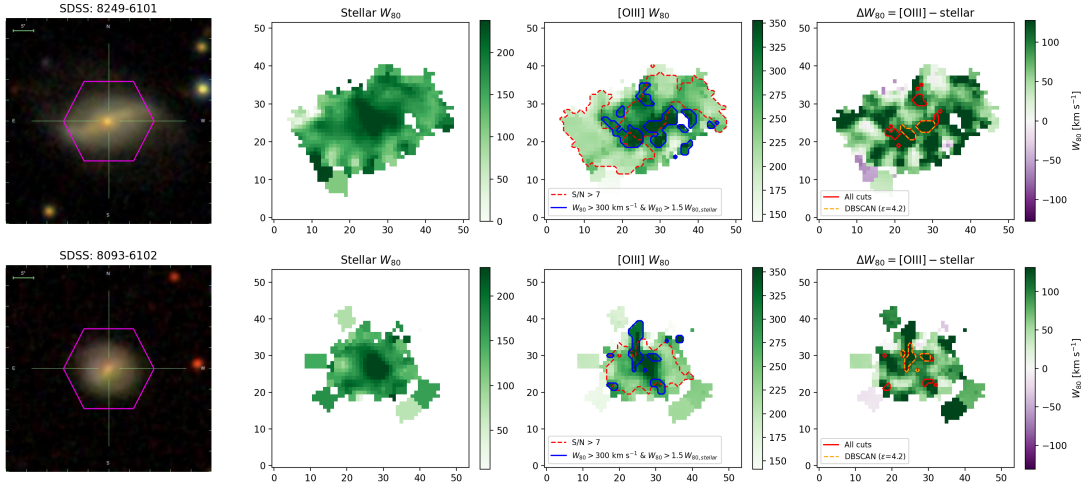

Figure 31. Two examples of galaxies that have only been selected with the DBSCAN algorithm. The panels are the same as for figure (30) but for galaxy 8249-6101 in the *top row* and for galaxy 8093-6102 in the *bottom row*. The only difference is that the orange dashed contours in the ΔW_{80} map shows the region selected by the DBSCAN algorithm. Here, the strength of this algorithm is used that detects an elevated region, if enough elevated spaxel lie sufficiently dense together that are not directly connected.

Now, a ε is chosen that detects most of the connected regions but also shows the advantage of the DBSCAN algorithm that a cluster is recognized if they lie sufficiently dense together, even if there is a spaxel in between two elevated ones. I want to include these regions, since I do not expect noise to lie this dense together. Two examples of galaxies that have only been detected by DBSCAN are shown in figure (31). With $\varepsilon = 4.2$, 33 galaxies are detected that were not detected by CCL and only 6 galaxies are missed, only detected by CCL. The DBSCAN algorithm selects 384 galaxies, where at least one cluster is found. With this choice 90% of the all galaxies that were detected either by CCL or DBSCAN (390), were dected by both CCL and DBSCAN (351).

In the following, all the selection criteria for fossil AGN outflows that are implemented on the initial non-AGN sample are summarized:

(i) Quality cut: [OIII]λ5007 SNR > 7 AND

(ii) Relative cut: $W_{80,[\mathrm{OIII}]} > 1.5 \cdot W_{80,\star}$ AND

(iii) Absolute cut: $W_{80,[\mathrm{OIII}]} > 300\,\mathrm{km\,s^{-1}}$ AND

(iv) Clustering: DBSCAN with $\varepsilon = 4.2$, MinPts $= \pi(d_{\mathrm{PSF,px}}/2)^2$ OR CCL with MinPts

These criteria select 390 unique fossil AGN outflow candidates.

6 Analysis and discussion

In this section, I want to discuss the applied selection method to find the fossil outflow candidates as well as some found promising sources and properties that can be calculated from those found sources.

In a first step, a multiwavelength AGN sample is subtracted to study only the currently non-AGN galaxies. There might be AGN sources in the initial non-AGN sample at a very late stage with lower radio flux $f_{1.4\,GHz} < 1\,mJy$ (White et al. 2015) not detected by the selection of Albán et al. (2024). They suggest that radio selection detects AGN preferentially at very late stage and a connection between kinematic outflow signatures and radio emissions exists since radio selected AGN have more spatially extended outflows. This implies that radio AGN have been experiencing activity for a longer time or went through multiple AGN cycles (Morganti 2017), suggesting a later stage in the lifecycle. Because radio emission can also originate in relic radio jets and lobes it could therefore also be assumed that in the radio selected AGN sample that is selected with total galaxy radio luminosities there are some hidden fossil outflow candidates. Also, the dusty torus that surrounds the SMBH and the accretion disk could still be hot and emit in the MIR for a significant time after the galaxy nucleus turned inactive. Therefore, it is also possible that there might be some galaxies in the MIR AGN sample that experienced recent AGN shutdown.

For fossil outflow selection, I started by selecting a rather low [OIII]λ5007 line SNR > 7 cut, which leads to a couple of false selections, especially in the outskirts of galaxies. This will be further discussed in the next section, where a visual inspection of the entire sample of fossil outflow candidates is performed. Generally the quality of the MaNGA samples biases our search towards galaxies with more gas that can be photoionized and with higher luminosity since a significant fraction of the initial sample does not survive the signal to noise cut. Also, since we are looking for signatures that are expected to lie further away from the galaxy center, even if the galaxy has enough SNR in the center, the fossil outflows could be missed.

In the next step, I selected galaxies that showed relative kinematic elevation of the gas kinematics compared to the stellar kinematics. Here it is important to note that apart from disturbance from outside the galaxy, also galaxy spirals and bars can cause streaming or radial movement and offset between the gas and stellar kinematics (Fathi et al. 2005; López-Cobá et al. 2022). But especially with the absolute W_{80} requirement of the gas kinematics, to be considered kinematically elevated, I expect that this phenomenon does not significantly contribute to the detections. This absolute W_{80} cut could be better motivated in future work with analysis of the correlation of high SFR for galaxies with many low elevated spaxel detected by the relative cut. In this way, the assumption that those regions are a result of stellar feedback mechanisms could be reassured. To avoid

superimposing the absolute cut, in order not to exclude fossil AGN outflows with lower W_{80} ionized gas widths, a selection on the basis of the spatial distribution of the relative elevated regions could also be considered. Galaxies with a broad distribution of the elevated regions over the galaxy could be excluded since fossil outflows are expected to be spatially restricted and the broad distribution is a sign for SF dominated galaxies, as seen in section 5.2.1. This could be measured for example with the Gini-coefficient, which is a statistical measure for dispersion or maldistribution.

For the last step, I chose the minimal number of spaxel MinPts that is needed, to be selected as a significant detection from the maximal dense circular area with the resolution limiting PSF FWHM as the radius. If the shape deviates from a circular area to for example an ellipse, the major axis is longer than the PSF FWHM and therefore MinPts could be set to a lower value for elongated region shapes. So, if a sufficiently dense region can be assured that is not expected from noise with length bigger than the PSF FWHM, MinPts could be reduced and more significant detections could be made.

6.1 Visual inspection of final sample

With a visual inspection of the final fossil outflow candidate sample, I aim to identify false detections and galaxies with kinematical disturbance coming from outside the galaxy like from galaxy mergers. I also want to determine whether the outflows exhibit the shape properties, described in section (1.4), that are expected for fossil outflows. These are mainly detachments from the nucleus and a biconical shape along the galaxy minor axis with asymmetry. For the visual inspection, I used `Marvin`'s web application, which is a tool provided by the SDSS (Cherinka et al. 2019) to quickly retrieve and visualize the MaNGA data and outputs of the DAP. To look for possible interactions from outside the galaxy, the "Navigate" Tool of the SDSS skyserver (Szalay et al. 2002) was used. The SDSS skyserver is a web portal, where SDSS imaging and spectroscopy data can be accessed, and crossidentifications with other catalogs and observations can be made. For further crossidentification and imaging, including from other observations, SIMBAD is used in addition. The galaxies are divided into the following categories:

(i) Kinematically disturbed (58 galaxies) that show signs of current or recent interactions with other galaxies.

(ii) Failed (7 galaxies) where the binning for the stellar kinematics failed (like 11758-1901) or the galaxy had extremely low SNR, which resulted in just one bin for the entire galaxy.

(iii) Improbable fossil outflows (66 galaxies) that show a kinematically elevated region in only one voronoi bin of the stellar kinematic fit in the outskirts of the galaxy.

(iv) Strong central kinematic elevation of the gas kinematics (110 galaxies), where the signatures were found only in the central region.

(v) Promising fossil outflow candidates of second order (109 galaxies) that exhibit at least one but not all properties that are expected for fossil outflows.

(vi) Promising fossil outflow candidates of first order (48 galaxies) that show all the properties in the kinematic elevated regions that are searched for.

An example of a galaxy categorized as an improbable fossil outflow candidate is shown in figure (32). The detected region is from only one vornoi bin in the outskirts of the galaxy with equal stellar kinematics. The [OIII] line fitting is performed spaxelwise but the [OIII] W_{80} map shows that the subtracted stellar continuum from the bins influence the line fits in the binned regions. On the one hand, the detections in those binned regions can be explained by a low fitted stellar dispersion that leads to a quick relative elevation of the [OIII] line width. As explained in section (4.1) for higher distances from the galaxy center the formally correct SNR for the binning falls short which indicates that the stellar kinematic fits at higher radii cannot fully be trusted. On the other hand, here at typically lower SNR the [OIII] line fitting is prone to noise fitting.

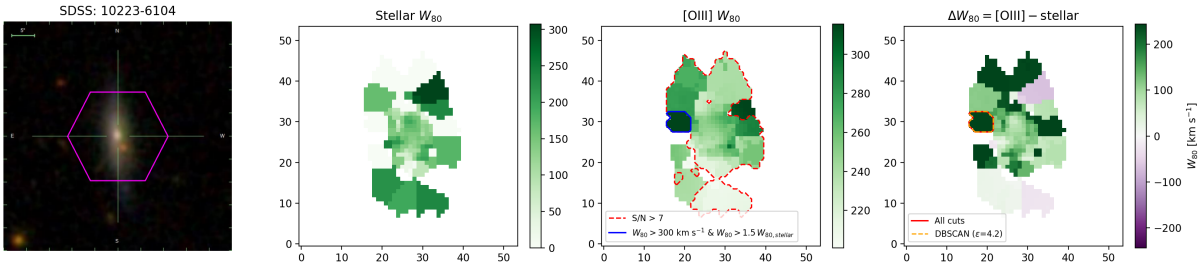

Figure 32. Example of a galaxy classified as improbable fossil outflow candidate. The panels are the same as in figure 31 but for galaxy 10223-6104.

The division into galaxies with only central elevated gas kinematics and promising fossil outflow candidates of first and second order helps to identify promising candidates. The galaxies with only central elevated gas kinematics are often observed face on and an assessment of whether they show detached or biconical outflows is not possible. Sometimes only the center of the galaxy has enough signal and it is not possible to determine whether extended outflows exist (figure (33)). Galaxies are categorized as promising fossil outflow candidates of second order, if they show elevated gas kinematics along the galaxy minor axis but without an detechment from the nucleus like in figure (34). Also in this category there are galaxies, where the elevated regions are detached but lie within the galaxy plane at more face on observed ones or along the galaxy major axis.

In table 1 the category list for the first 10 galaxies in the fossil outflow candidate sample is shown. The full sample can be seen in the appendix (D) and a machine-readable version is available.

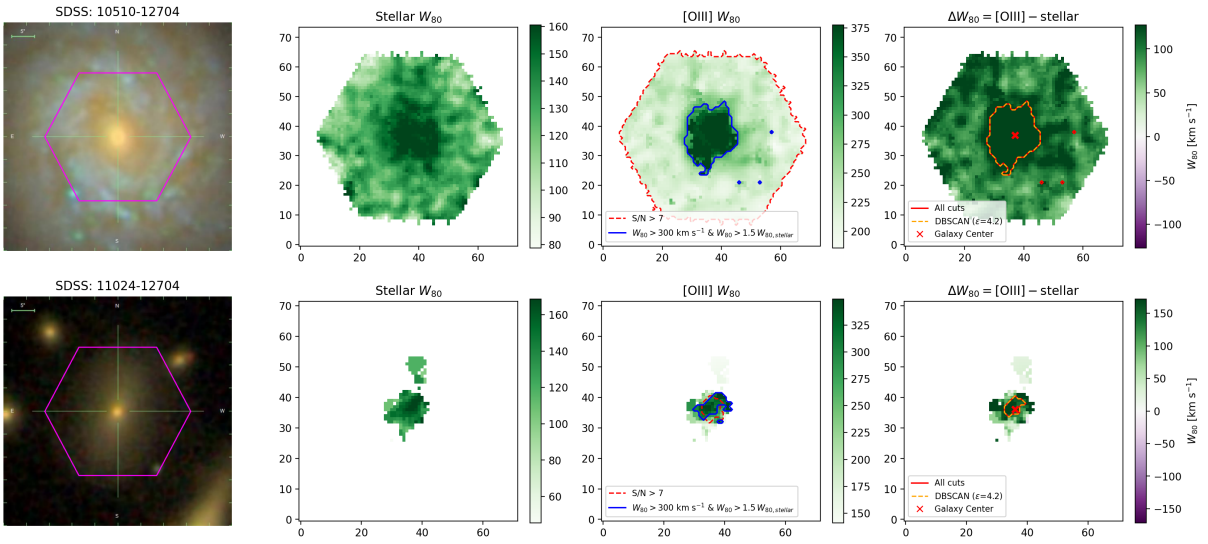

Figure 33. Examples of a galaxies classified as only showing central elevated gas kinematics. The panel rows are the same as in figure 31 with additional marking of the galaxy center in the ΔW_{80} map with a red cross. The *top panels* correspond to galaxy 10510-12704 that is observed face on and *bottom panels* to galaxy 11024-12704, where only the central region has high enough SNR.

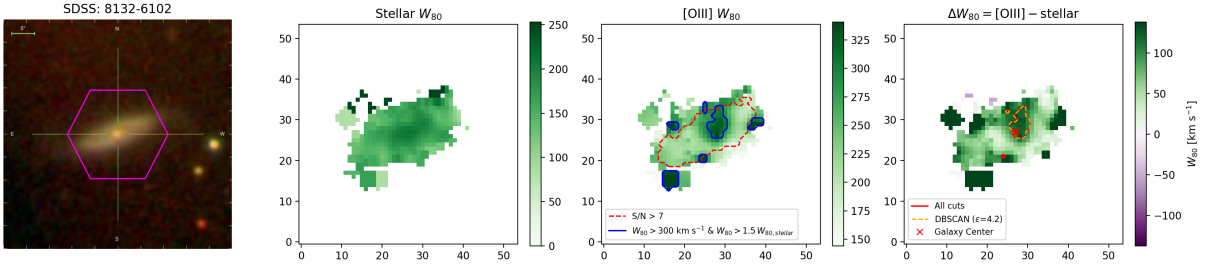

Figure 34. Example of a galaxy classified as a promising fossil outflow candidate of second order. The panels are the same as in figure 33 but for galaxy 8132-6102. Here the detected region extends along the galaxy minor axis but shows attachment to the galaxy center.

Table 1. Category table of the first 10 fossil outflow candidate sample.

PlateIFU	kin. dist.	prom. 1st	prom. 2nd	str. centr.	improb.	failed	AGN
10214-1902	0	0	0	1	0	0	1
10215-1902	0	1	0	0	0	0	0
10215-6102	1	0	0	0	0	0	1
10218-6103	0	0	0	0	1	0	0
10219-12702	0	0	0	1	0	0	0
10221-3701	0	0	1	1	0	0	0
10223-1901	0	0	0	1	0	0	0
10223-3703	0	0	0	1	0	0	1
10223-6104	0	0	0	0	1	0	0
10225-3704	1	0	0	1	0	0	0

Notes. The table is shown as it is stored in the supplementary data. The first column reports the PlateIFU numbers of the galaxies and the second to seventh column show the defined categories. Here a boolean array is stored to indicate that the galaxy belongs in the category if the value is 1 or not if the value is 0. The eighth column shows an additional flag for a possible AGN.

Noise fitting inspections were not performed for the entire sample except for the promising fossil outflow candidates that will be presented in section (6.3). So there could be galaxies in the sample where the elevated regions lie close to the SNR cut that are a result of noise fitting. In addition, I add one flag for the galaxies that were classified as AGN of at least one catalog on SIMBAD (153 galaxies). These galaxies have to be dealt with with more caution. It should be noted that many older catalogs are listed on SIMBAD as well and galaxies are denoted AGN even if they were detected as LINER by the Albán and Wylezalek (2023) optical BPT catalog but did not pass the equivalent width cut. So, whether the galaxy is refused or not has to be decided in each special case. The relative fraction of galaxies that are both in the strong central category and were listed in some AGN catalog is with $52/110 \sim 0.47$ the highest fraction of all categories. The relative fraction of galaxies with an AGN flag is $0.35 - 0.40$ for the other categories except for the failed category, where it is 0.

6.1.1 Crossmatches with resolved BPT catalog

The resolved BPT AGN catalog by Jaison et al. (in preparation) found 776 AGN candidates with a low SNR > 1 criteria but additional checks to avoid noise fitting. As mentioned in section (4.4) because of its resolved nature it should also detect galaxies that lack central AGN emissions and might be hidden behind large column densities in the center, off-nuclear AGN or relic AGN. In theory, if the multiwavelength AGN sample is subtracted from this resolved AGN catalog only off-center AGN or relic AGN galaxies should be left. After the subtraction, 442 galaxies of the resolved AGN catalog remain. If those galaxies are compared with the fossil outflow candidate sample, only 79 coinciding galaxies are found. This small overlap can be explained by multiple reasons. First, 13 of the 442 galaxies were discarded due to quality reasons in my analysis. Further 46 galaxies do not have ≥ 20 valid spaxel with [OIII] line SNR > 7 and therefore cannot be clustered. Many more galaxies that were classified as AGN by the resolved BPT method because of AGN signatures in the outer parts of the galaxy show too low [OIII] line SNR in those regions to analyze them for kinematical ionized gas elevation. An example for this is shown in figure (35). Having said that, in some galaxies that show AGN line diagnostic signatures in shapes, expected for fossil outflows no elevated gas kinematics were detected despite high enough SNR (figure (36)). Because of the low required SNR, there could also be some false AGN classifications in the resolved AGN catalog.

As anticipated, there is no overlap with the galaxies that were classified as failed and only a low overlap with the galaxies categorized as improbable fossil outflow candidates (4/66). The relative overlap with the galaxies categorized as promising fossil outflow candidates second (30/109) and first order (17/48) is the highest out of the categories.

The remaining fossil outflow candidates do not show a high enough fraction of line diagnostic AGN signatures to be classified as AGN by the resolved BPT method. This

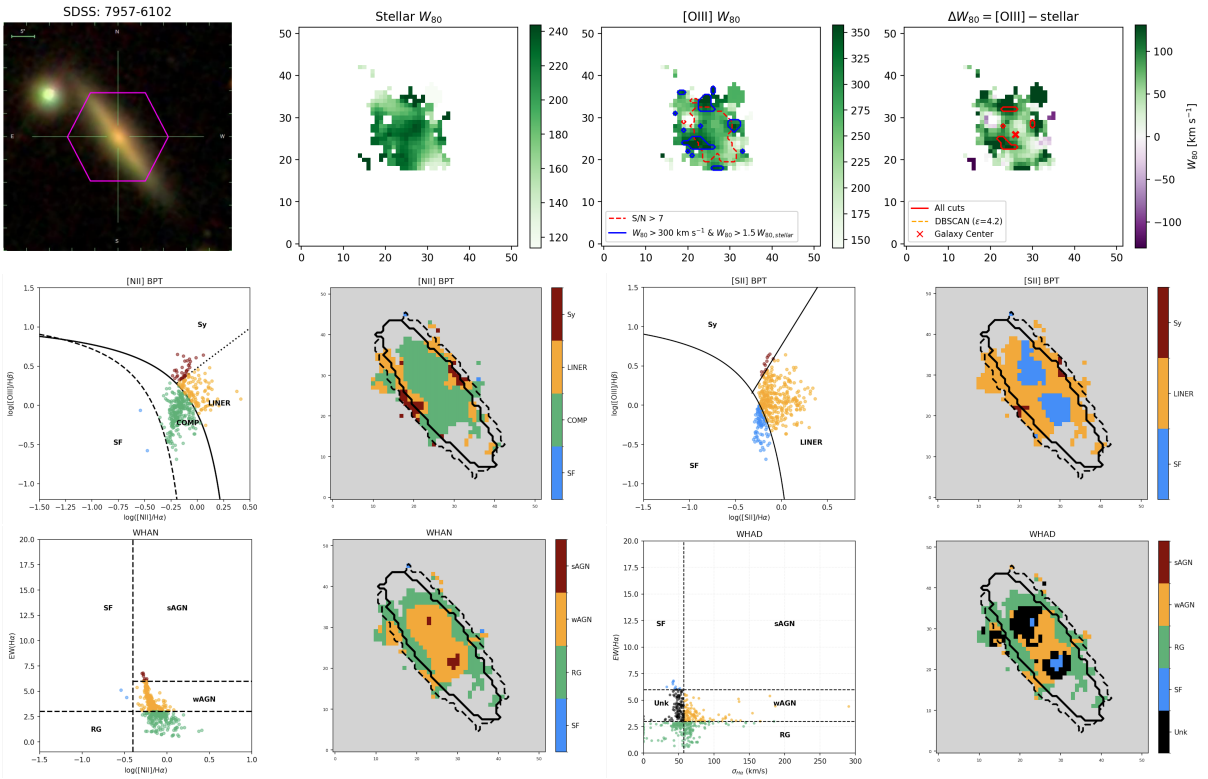

Figure 35. Example for a galaxy with AGN line diagnostic signatures expected for fossil outflows but too low [OIII] line SNR to analyse the ionized gas kinematics. The *top panel row* is the same as in figure (33) but for galaxy 7957-6102. In the residual ΔW_{80} map no clustered region by the DBSCAN algorithm (and also none by CCL)) can be seen. The *second panel row* shows the [NII] BPT and [SII] BPT diagrams and their resolved counterparts next to it and the *Third panel row* similarly shows the WHAN and WHAD diagram from Jaison et al. (in preparation). The black dashed and solid contours respectively show the general MEGACUBES SNR > 5 and SNR > 10 masks. Especially in the resolved [NII] BPT map in the center of the galaxy there is a composite region but along the galaxy minor axis with detachement from the center LINER or Seyfert signatures are detected. In the [OIII] W_{80} map elevated spaxel in those regions can be seen but because of the signal quality and the SNR cut they cannot be detected as a large enough cluster.

is often the case, because fossil outflows are spatially restricted and partly lopsided and only visible in one ionization cone. Examples for such galxies can be seen in the section (6.3), where promising fossil outflow candidates will be presented. Some of these sources were not classified as AGN by Jaison et al. (in preparation).

6.2 Outflow properties

To investigate the impact of the outflow on the galaxy and to compare the fossil outflow properties to those found in currently active galaxies, mass outflow rates $\dot{M}_{\rm out}$ and energy rates $\dot{E}_{\rm out}$ can be calculated. The comparison is made to the properties from a sample of 293 AGN out of the MaNGA galaxies derived by Gatto et al. (2024). The AGN are optically selected with a combination of the BPT and WHAN diagnostic diagrams using

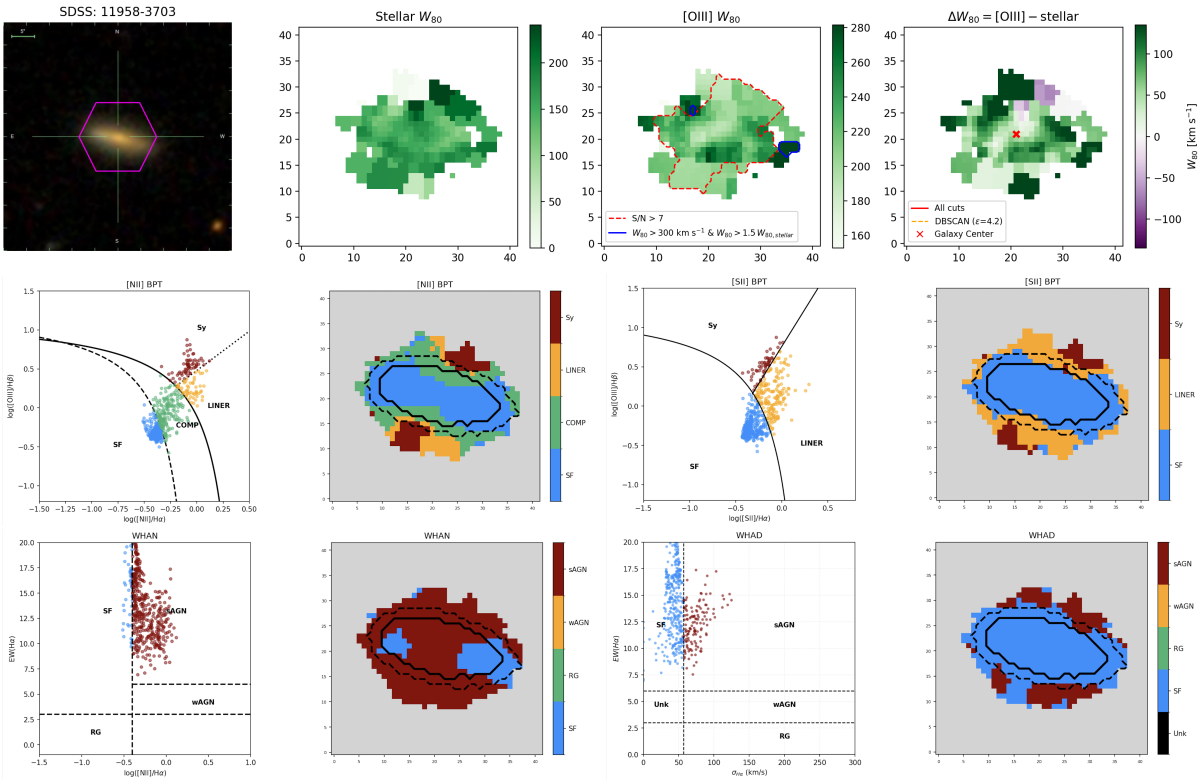

Figure 36. Example for a galaxy with AGN line diagnostic signatures that are expected for fossil outflows but no detected elevated ionized gas kinematics. The *panels* are the same as in figure (35) but for galaxy 11958-3703. Here despite the LINER and Seyfert signatures along the galaxy minor axis with detachement from the nucleus there are no detections of ionized gas kinematics in those regions.

only nuclear spectra. In order to calculate outflow properties, a kinematically disturbed region (KDR) is defined, where the AGN significantly affects the gas kinematics. In Gatto et al. (2024) this is defined over the region where the [OIII] line width $W_{80,\mathrm{cut}} > 315\,\mathrm{km\,s^{-1}}$ and the BPT diagram shows AGN or composite signatures. Because some promising fossil AGN outflow sources in section (6.3) suggest that the BPT line diagnostic does not reliably detect fossil outflows, the second criterion is neglected. Following the derivations in Gatto et al. (2024) the outflow properties will be calculated as follows.

Gas mass. The ionized gas mass M^i_{gas} in spaxel i can be calculated using the expression (Carniani et al. 2015):

$$M^i_{\mathrm{gas}} = 0.8 \cdot 10^8 M_\odot \frac{1}{10^{[\mathrm{O/H}]-[\mathrm{O/H}]_\odot}} \frac{L^i_{[\mathrm{OIII}]}}{10^{44}\,\mathrm{erg\,s^{-1}}} \frac{\langle n_e \rangle}{500\,\mathrm{cm^{-3}}} \tag{22}$$

assuming a typical temperature for the narrow line $T_e \sim 10^4\,\mathrm{K}$. Here $M_\odot$ is the solar mass, [O/H] the metallicity that is assumed to be equal to the solar oxygen abundance $[\mathrm{O/H}] = [\mathrm{O/H}]_\odot$, $L_{[\mathrm{OIII}]}$ is the integrated [OIII] line luminosity and n_e the electron density.

For the luminosity $L^i_{[\mathrm{OIII}]}$ only the integrated wings of the line profile of each spaxel i

in the KDR with absolute velocities larger than $W_{80,\mathrm{cut}}/2$ are considered. In this way the contribution of the lower velocity gas that should be dominated by the galaxy gravitational potential is excluded (figure (37)).

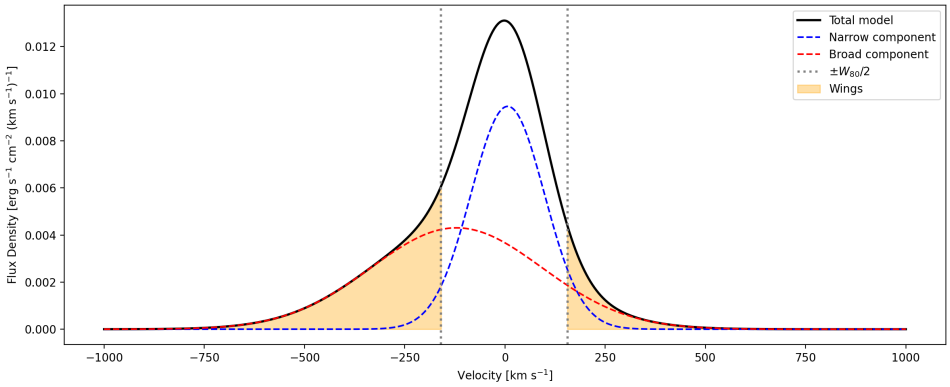

Figure 37. Visualization of the [OIII] line wings in emission lines with a secondary component in the velocity space. Only the emission line fit without the observed spectrum is shown in black with the narrow component in blue dashed and the broad component in red dashed lines. The orange highlighted area corresponds to the wing flux which is integrated to the outflow luminosity $L_{[\mathrm{OIII}]}$.

To calculate the electron density, the forbidden [SII] lines are used. The single ionized [SII]$\lambda\lambda$6716,6731 doublet de-excites between $1 \lesssim n_e \lesssim 10^5\,\mathrm{cm}^{-3}$ by photon emission. In this region, their relative emission line intensity is a function of electron density and can therefore be used to calculate n_e (Osterbrock and Ferland 2006). The following expression is used (Sanders et al. 2016; Kakkad, D. et al. 2018):

$$n_e(R) = \frac{cR - ab}{a - R}, \qquad R = \frac{F([\mathrm{SII}]\lambda 6716)}{F([\mathrm{SII}]\lambda 6731)} \tag{23}$$

with the line flux ratio R. The coeffecients are $a = 0.4315$, $b = 2,107$ and $c = 727.1$. The line flux ratio is theoretically restricted to $R_{min} = 0.4475$ and $R_{max} = 1.4484$ (Sanders et al. 2016) for the high and low density limit where the [SII] doublet de-excites. A mean electron density $\langle n_e \rangle$ is calculated for all valid spaxel with valid R and where the [SII]λ6716 line has A/N > 3. The noise is calculated over the standard deviation of the observed residual flux with subtracted stellar continuum in a spectral window beside the emission line. The stellar continuum as well as the emission line model fits for the [SII] lines to calculate the flux ratio is taken from the MEGACUBES as it was done in Gatto et al. (2024).

The total mass of ionized gas is calculated over the sum over the spaxel in the KDR $M_{\mathrm{gas}} = \sum_i M^i_{\mathrm{gas}}$.

Outflow velocity. Calculating the outflow velocity v_{out} is a difficult task because the outflow direction relative to the observing angle is unknown. The observed line width

is less dependent on the orientation and is therefore a better indicator for the outflow velocity than the LOS velocity for emission lines. This is discussed in the appendix (A). Following Riffel et al. (2023b) and Gatto et al. (2024) the flux weighted mean of the [OIII] line W_{80} is adopted as the outflow velocity:

$$v_{\rm out} = \frac{\langle W_{80,\rm KDR} F_{\rm KDR} \rangle}{\langle F_{\rm KDR} \rangle}. \tag{24}$$

Because of the weight with the average flux $\langle F_{\rm KDR} \rangle$ over the KDR, a lower contribution is given to spaxel with lower fluxes that are typically noisier. The [OIII] line W_{80} best fit values described in section (4.2) are used and a SNR > 3 cut following Gatto et al. (2024) is implemented.

Radius of kinematic impact. Similarly, the radius of kinematic impact $R_{\rm out}$ is calculated with a flux weighted mean over all spaxel in the KDR:

$$R_{\rm out} = \frac{\langle R_{\rm KDR} F_{\rm KDR} \rangle}{\langle F_{\rm KDR} \rangle}. \tag{25}$$

Mass outflow rate and kinetic power. With these properties, the mass flow rate can now be computed assuming spherical symmetry (Dall'Agnol de Oliveira et al. 2021; Riffel et al. 2023b; Gatto et al. 2024):

$$\dot{M}_{\rm out} = \frac{M_{\rm gas} v_{\rm out}}{R_{\rm out}} \tag{26}$$

The kinematic power or energy rate of the outflow is then calculated with:

$$\dot{E}_{\rm out} = \frac{1}{2} \dot{M}_{\rm out} v_{\rm out}^2. \tag{27}$$

In table (2) the outflow properties for some promising fossil outflow candidates that will be discussed in the next section are presented. A large variance in ionized gas masses and resulting mass outflow rates and energy rates can be observed. The outflow velocities do not significantly differ because for most of these galaxies it is averaged over a large region where only smaller parts show high W_{80} values. The table for the outflow properties for the entire fossil outflow candidate sample can be seen in the appendix (D) and a machine-readable version is available.

If the derived mass outflow rate and energy rate for the fossil outflow candidate sample are compared to those found for the optically selected AGN sample (Gatto et al. 2024) a generally broader distribution is found streching to generally lower values (figure (38)). When looking closer at this lower mass outflow rate and lower energy rate tail for the fossil outflow candidate sample mostly galaxies classified as improbable fossil outflow candidates are found. These galaxies only show small spatially restricted outflow regions with large

Table 2. Ionized-gas outflow properties for promising fossil outflow candidates.

PlateIFU	$L_{\mathrm{OIII,wing}}$ (10^{39} erg s^{-1})	n_e (cm^{-3})	M_{gas} ($10^3\,M_\odot$)	R_{out} (kpc)	v_{out} (km s^{-1})	$\dot{M}$ ($10^{-5}\,M_\odot$ yr^{-1})	$\dot{E}$ (10^{36} erg s^{-1})
8138-6101	8.43	822	11.09	1.23	367	338.84	143.71
9511-3704	5.86	292	2.73	1.50	367	68.28	28.97
10215-1902	1.25	295	0.59	3.25	375	6.97	3.08
9885-1901	1.47	176	0.41	1.26	349	11.70	4.49
8080-3702	1.51	983	2.38	0.74	455	150.05	97.72
8250-6101	1.85	200	0.59	2.31	348	9.13	3.49
8723-1902	0.70	685	0.76	1.15	366	24.75	10.43
8442-1901	7.84	677	8.49	1.23	442	311.77	191.47

distances to the outflow center. It is notable that the tail towards higher mass outflow rates and energy rates reach similar maximal values as observed for AGN. This indicates that after the AGN shutdown comparable mass outflows sometimes persist that can have comparable kinematic power.

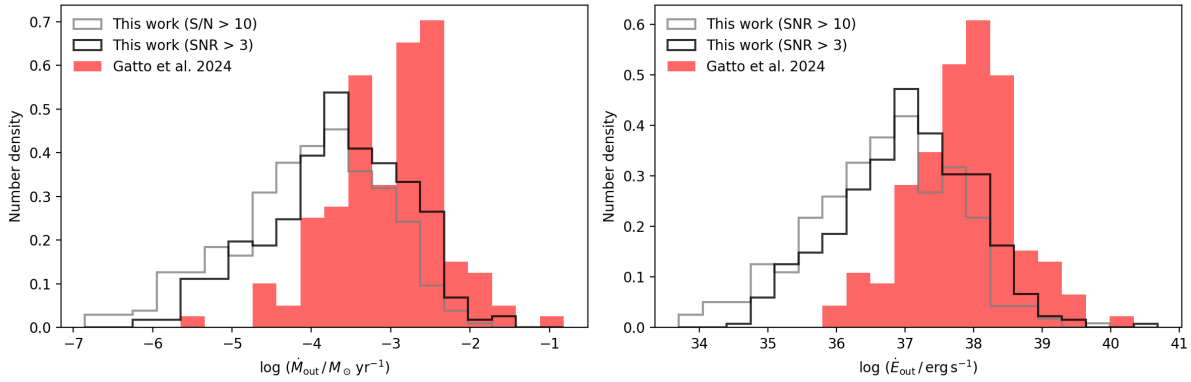

Figure 38. Normalized distribution of the mass outflow velocity in the *left panel* and energy rates in the *right panel*. The outflow properties of the fossil outflow candidates calculated with emission line SNR > 3 are shown in black and with emission line SNR > 10 in grey. The distributions for the AGN sample from Gatto et al. (2024) are shwon in red. Here the emission line SNR > 3 cut was used.

The low SNR requirement for the [SII] lines and the [OIII] line sometimes result in extremely high average outflow velocities (e.g. $v_{out} = 3289\,\mathrm{km\,s^{-1}}$ for galaxy 8483-12704) or overestimates in the electron density. Here, the emission line fits failed because of the signal that is too low. When a higher SNR cut is implemented for the calculation with the emission lines like SNR > 10 the outflow properties systematically shift towards smaller values. An example for a drastic change in the mean electron density with higher SNR cut is displayed in figure (39). Additionally, the sperical symmetric outflow assumption could be approved for fossil outflows since detached boconical or one sided outflows are often observed.

In a next step, energy coupling efficiencies could be calculated with the relation of the AGN bolometric luminosity to the energy rate. This gives a good estimate of the

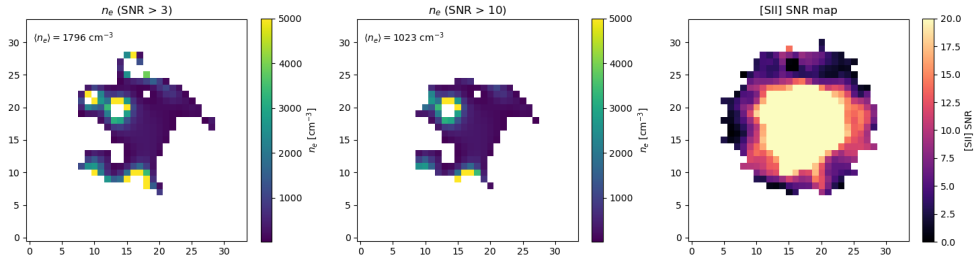

Figure 39. Electron density maps and [SII]λ6716 SNR map for galaxy 10214-1902. In the *left panel* the electron density map is displayed showing only spaxel with valid [SII] line flux ratios and SNR > 3. The average electron density over the galaxy is shown in the upper left corner. This average value drastically reduces when considering only spaxel that pass SNR > 10 cut which is shown in the *second panel*. In the *third panel* the [SII]λ6716 SNR map is displayed. The variance of electron density values in the galaxy suggest that a mean electron density is not a good assumption for the whole galaxy to calculate the outflow mass (Kakkad, D. et al. 2018)). It will still be used in this work because the electron density is observed to locally diverge to extreme values.

influence of the outflow on the host galaxy. The bolometric luminosity can be estimated with the [OIII] line luminosity $L_{[\mathrm{OIII}]}$ triggered by the AGN (Heckman et al. 2004; Trump et al. 2015). It has to be discussed to which extent this measurement is true to infer the bolometric luminosity of remnant AGN. Since fossil AGN outflows are a multiphase structure and have a strong atomic and molecular component, the here calculated ionized gas outflow properties only pose a part of the total outflow.

6.3 Promising sources

In this section I will discuss some of the first order promising sources in further detail. This is not a complete list but rather a selection of fossil outflow candidates, where the in section 1.4 described properties match best. For all the following galaxies no significant correlation between the spaxel that show elevated [OIII] line widths and their SFR is observed and they are not classified as an AGN by any catalog on SIMBAD.

Galaxy 8138-6101 (MaNGA ID: 1-339010) is classified as a spiral galaxy from the Galaxy Zoo 1 project (Lintott et al. 2011) and is at a redshift $z = 0.031$. In the W_{80}-Maps figure (40) multiple properties expected for fossil outflows can be seen. The regions with elevated line widths show a clear detachement from the nuclues and are lopsided towards the east side of the galaxy. The predominance of the outflow on the east side is more clear from the two spectra in the lower panels, where a more dominant broad component in point A is observed. Looking at the relative elevation of the line width with respect to the stellar kinematics in the top right panel, a biconical shaped outflow along the minor axis of the galaxy can be observed. Even tho for this galaxy a moderate outflow velocity is reported in table (2) compared to the other candidates it reaches large [OIII] line widths

well over $W_{80} > 500\,\mathrm{km\,s^{-1}}$ in the outflow on the east side of the galaxy.

The SFR map with contours for the detected kinematically elevated regions and SNR masks is shown for completeness. An analysis of the dependence of the outflow velocities from the SFR for all galaxies in the fossil outflow candidate sample will be performed in the next section. In the stellar velocity map in figure (40) the relative velocity profile map that is expected for rotation is seen. A rotation axis in the LOS velocity along the galaxy minor axis is observed because the galaxy is observed relatively edge on. The [OIII] velocities seem to follow the rotation with some differences. These differences are visible in the residual Δv map, where it can be seen that the central region shows a redshift of the ionized gas compared to the stellar velocity. This can be interpreted as inflowing gas that separates the outflow from the galaxy center and is also observed for fossil outflows (Zubovas and Maskeliūnas 2023) in simulations. In the residual velocity map the two outflow regions being represented by the blue and redshifted east and west side can also be located. Note that the maps and pictures are oriented north up, east left.

This galaxy is also in the AGN sample of Jaison et al. (in preparation). Especially their resolved BPT diagrams, also shown in figure (40) show similar regions with AGN signatures that the kinematic analysis suggested. While the [NII] BPT classifies the central region as composite, the [SII] BPT detects a SF region in the galaxy center. In the WHAN and WHAD diagrams the sAGN signatures are not detached from the nucleus but they do not include a composite region. Here further analysis could be done to investigate whether those spaxel lie closer to the SF demarcation line. In the WHAD diagram gas turbulences as a result of the remnant AGN activity could cause higher Hα velocity dispersions and could push the region into the sAGN domain.

Galaxy 9511-3704 (MaNGA ID: 1-213820) is at a redshift $z = 0.027$. In figure (41) a clear detachment from the nucleus with polar outflows along the galaxy minor axis are observed again. The outflow towards the south east side seems to be collimated at larger distances from the nucleus with larger line widths.

For this galaxy the direction of the velocity gradient of the [OIII] LOS velocity is shifted by approximately 90°. While the stellar velocity map coincides with the expectations for rotation the shifted axis for the [OIII] velocity map suggests a biconical outflow of the gas along the minor axis, what can be seen in the [OIII] W_{80} map as well. This suggests outflow dominated movement of the ionized gas.

9511-3704 is not in the AGN sample of Jaison et al. (in preparation), but the [NII] BPT shows many spaxel in the composite region and the WHAN and WHAD diagram show indications for AGN signatures along the same axis where they are observed in the kinematic analysis.

Galaxy 10215-1902 (Manga ID: 1-153901) has a redshift of $z = 0.040$. Again a detachement from the nucleus is given and a lopsided main outflow along the south-east oriented minor axis with a clear secondary component in the emission line (figure

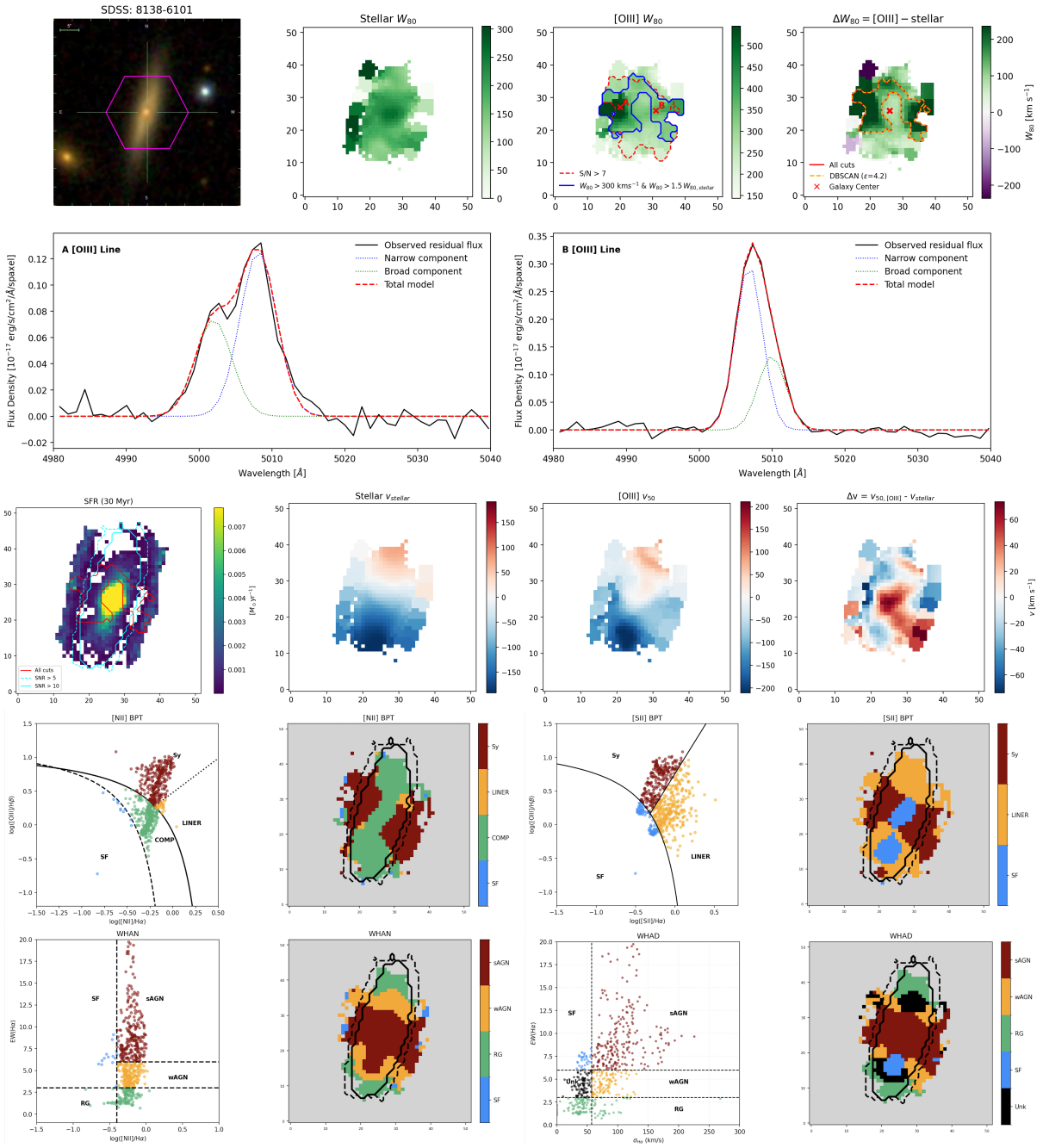

Figure 40. Maps and spectra of promising fossil outflow candidate 8138-6101. The *top panel row* are the same as in figure (33). The *panels in the second row* show zoomed in spectra of the [OIII] line in the rest wavelength frame of the with a red cross highlighted spaxel on the [OIII] W_{80} map. Here elevated line widths can be observed. In black the observed residual flux with subtracted stellar continuum is plotted and in dotted blue and green respectively the fitted narrow and broad component. The red dashed line shows the total fitted model. In the *third panel row* the SFR over the last 30 Myr on the left and LOS velocity maps in the other three panels are shown. The red contours in the SFR map shows the region with detected elevated gas kinematics and the cyan dashed and solid contours respectively show the general MEGACUBES SNR > 5 and SNR > 10 masks. The first velocity map shows the stellar velocity, the second the best fit [OIII] LOS velocity and the third velocity map shows the residual velocity $\Delta v = v_{50,[\mathrm{OIII}]} - v_{\mathrm{stellar}}$. The *fourth panel row* shows the [NII] BPT and [SII] BPT diagrams and their resolved counterparts next to it and the *fifth panel row* similarly shows the WHAN and WHAD diagram from Jaison et al. (in preparation).

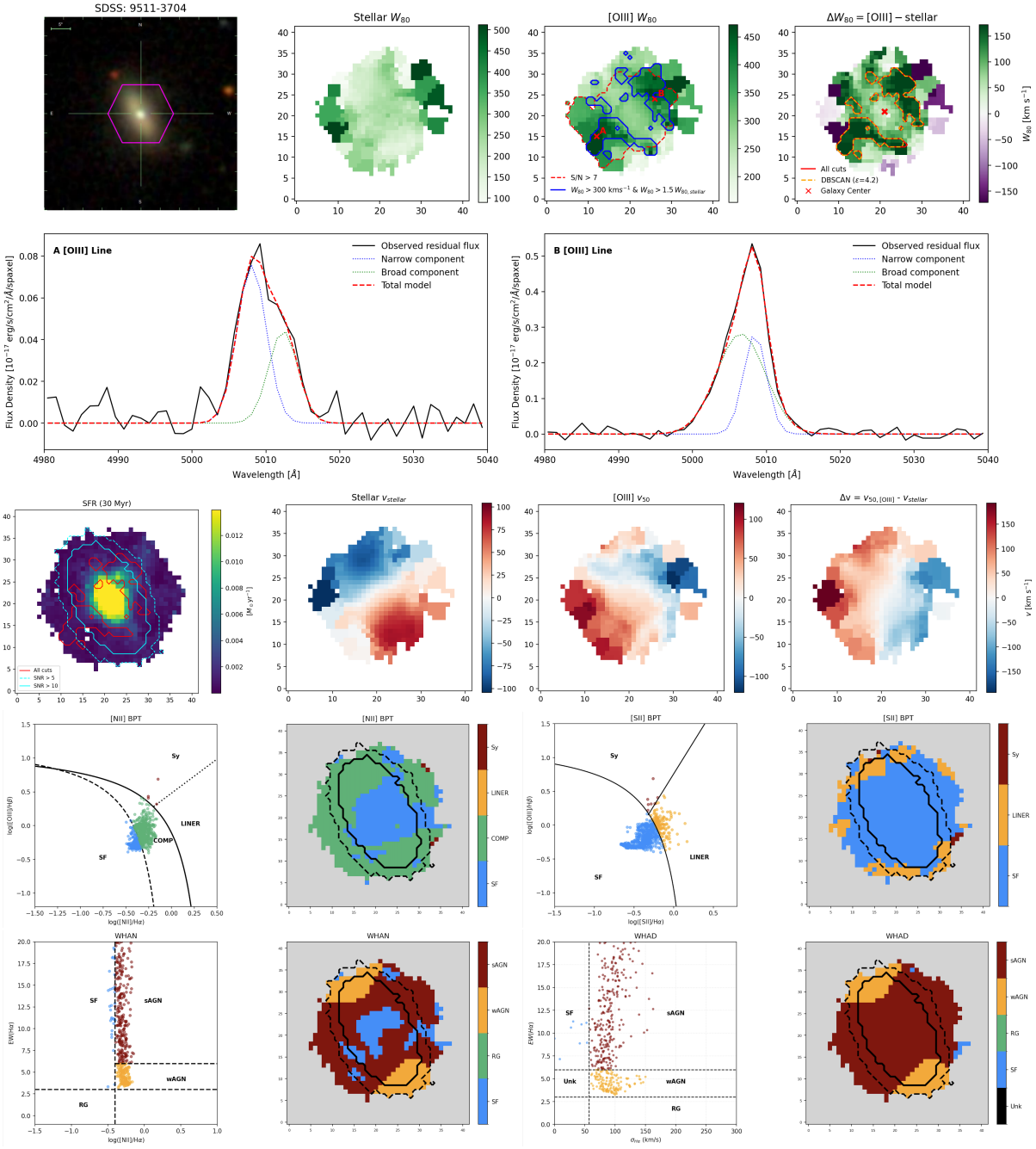

Figure 41. Maps and spectra of promising fossil outflow candidate 9511-3704. Same panels as in figure (40).

(42)). The [OIII] velocity map generally shows lower velocity offset compared to the stellar velocity except in the south east direction, where the elevated gas kinematics are detected. For this galaxy, the ionized gas movement does not seem to follow the stellar rotation as well. In the galaxy center there is a subtle red shifted region, which indicates an inflow. This results in a curved axis in the residual velocity map with a redshifted region in the center.

This fossil outflow candidate was also classified as an AGN by the resolved line diagnostic metod by Jaison et al. (in preparation) and again especially the [NII] BPT shows Syfert like ionization in the regions where elevated gas kinematics are detected. Here the galaxy nucleus is still classified as LINER and even Syfert like in the [SII] BPT. The WHAN and WHAD maps also show wAGN like ionization in the galaxy center but further out sAGN signatures in a biconical shape.

Galaxy 9885-1901 (MaNGA ID: 1-376102) is at redshift $z = 0.023$. In figure (43) a relatively symmetric biconical shaped outflow along the minor galaxy axis with detachment from the galaxy core is displayed. Although large regions with elevated kinematic signatures are detected, the absolute [OIII] line width is relatively low compared to the other promising fossil outflow candidates. Maybe because of the smaller ionized gas density ($\langle n_e \rangle = 176\,\mathrm{cm}^{-3}$) a larger fossil outflow can be formed as predicted by Zubovas and Maskeliūnas (2023). But without knowing the degree of ionization it is not possible to infer the actual gas density.

Resolved diagnostic diagrams show a mainly SF dominated galaxy in the BPT with some wAGN and sAGN signature detections in the WHAN diagram. Only the resolved WHAD diagram, which is also sensitive to broader line widths shows a similar biconical outflow but without a detachment in the center. The rotation axis of the stellar velocity is offset by 90° for the [OIII] LOS velocity reinforcing the biconical outflow picture.

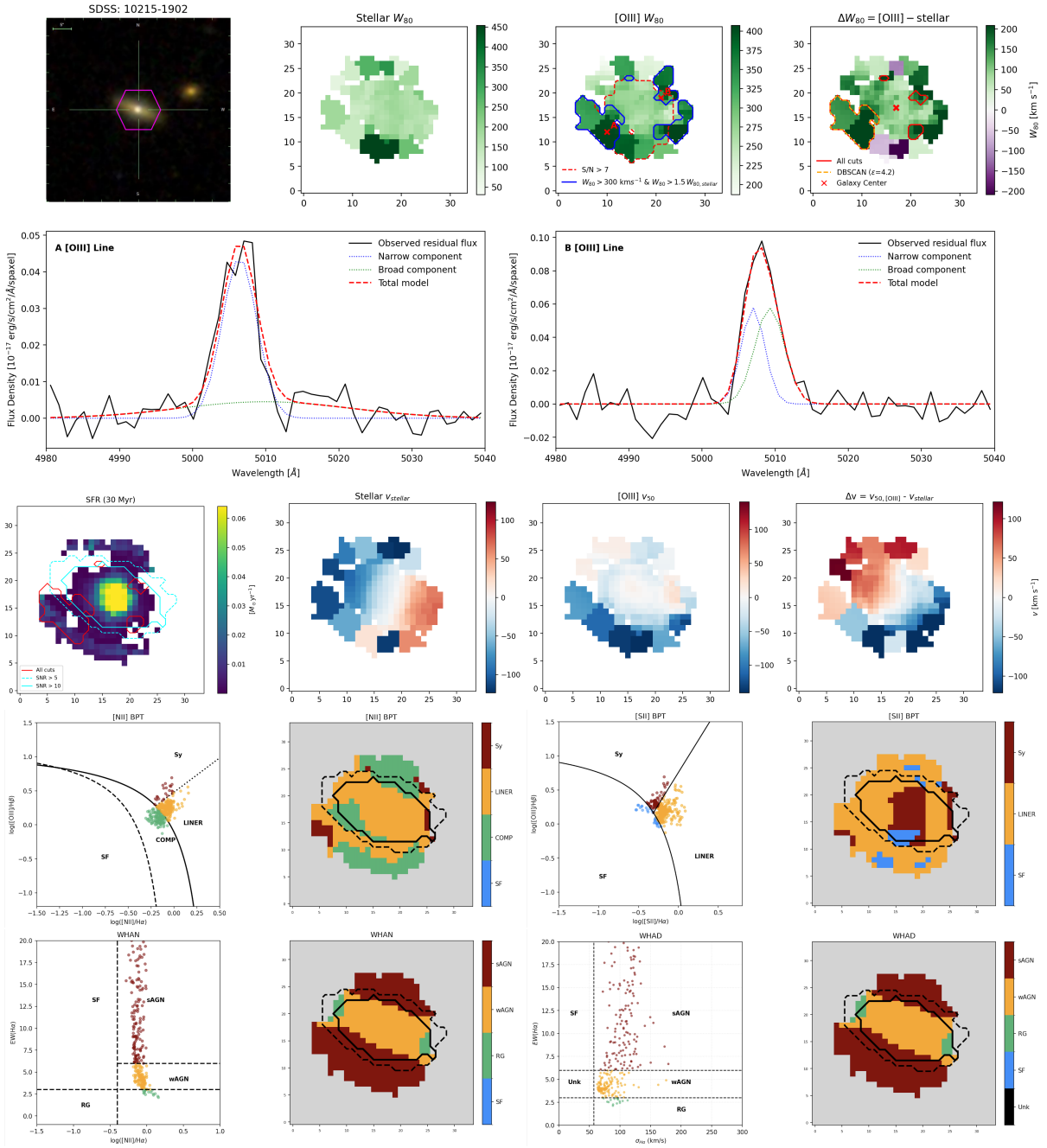

Figure 42. Maps and spectra of promising fossil outflow candidate 10215-1902. Same panels as in figure (40). In spectrum A it can be seen that the secondary component is not a good fit. Checking the selection, it is clear that here a single component gas fit was chosen as a better fit and the analysis was performed with this line width although a clear secondary component in the observed line profile is observable. Generally in the plots in this section the double Gaussian fits are showcased to highlight the asymmetry of the emission lines. Sometimes when the outflows are located at lower signal regions the single component gaussian was a better fit and was used for the analysis.

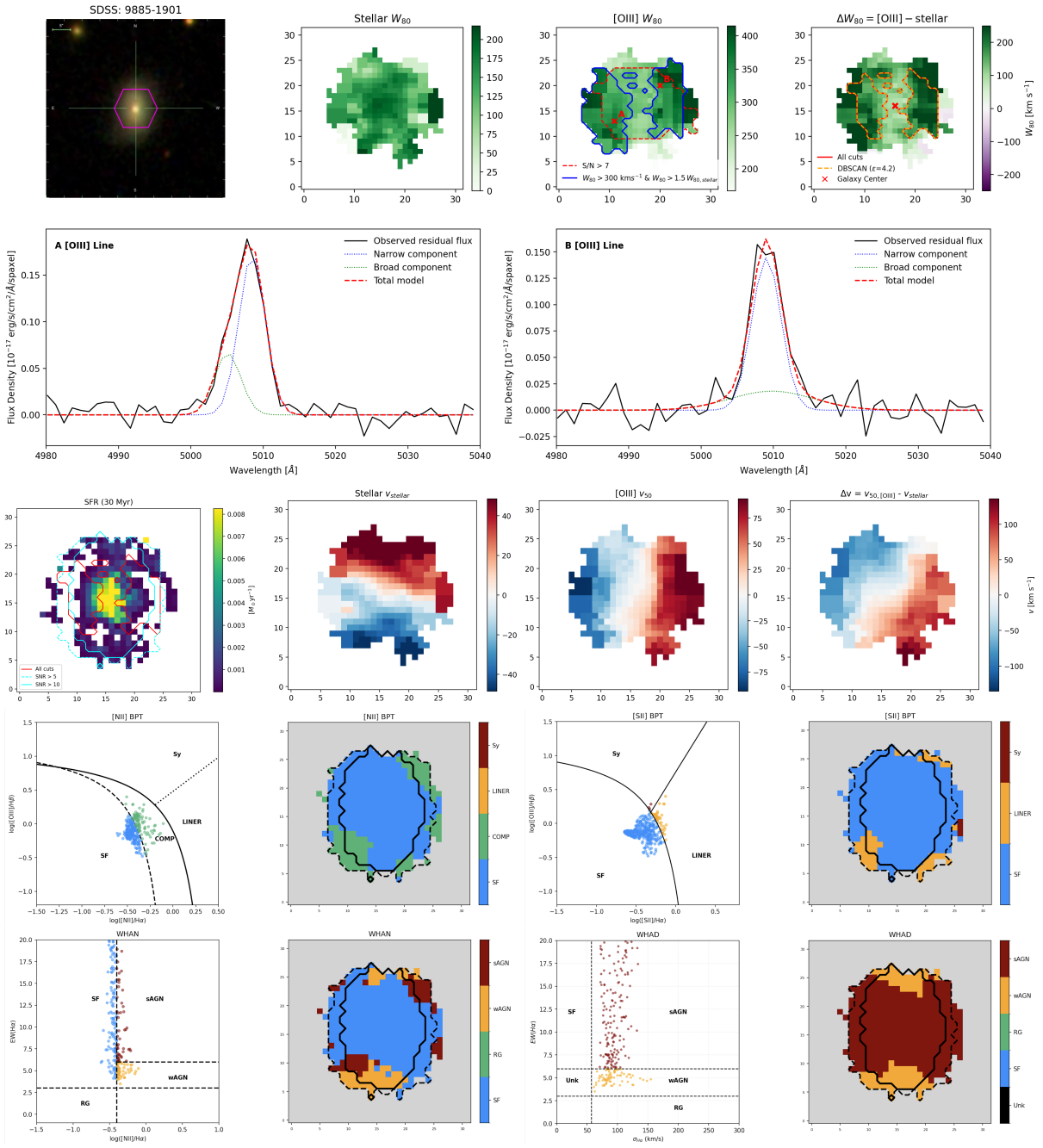

Figure 43. Maps and spectra of promising fossil outflow candidate 9885-1901. Same panels as in figure (40).

6.4 Possible SF driven winds

With the chosen selection method for fossil outflow candidates it is still possible that strong SF driven winds which pass the absolute cut cause the detected elevated ionized gas kinematics. To analyse, whether the outflow velocities correlate with SF driven winds, which are a result of a high SFR, for each galaxy a spaxelwise correlation of the outflow velocity with the SFR is checked. In addition, the global value trend of this correlation for the entire fossil outflow sample is checked. For the SFR the MEGACUBES maps over the

last 30 Myr are chosen. This timespan is selected because especially supernova feedback takes some time to be effective and is mostly covered with this time span (Leitherer et al. 1999). The correlation is measured with the Kendall tau test.

6.4.1 Spaxelwise correlation for each galaxy

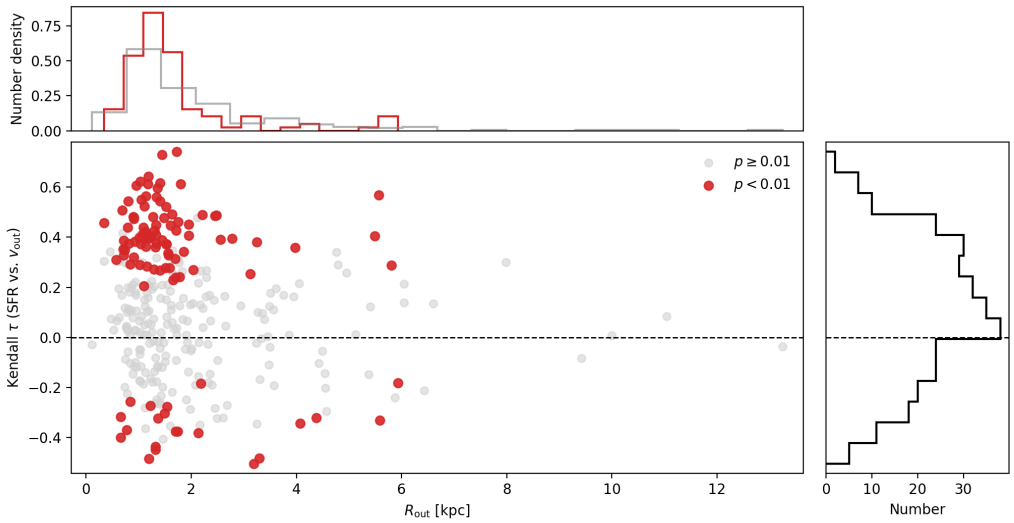

Figure 44. The *lower left panel* shows the Kendall τ values for correlation of v_{out} and the SFR plotted against the flux weighted average of the outflow radius R_{out} for each galaxy in the fossil outflow sample. Here the red dots show the galaxies with a significant spaxelwise correlation with $p < 0.01$ and the grey dots the galaxies with $p \geq 0.01$. The *top left panel* shows the distribution of the average outflow radius among the galaxies showing significant and non-significant correlation. No immediate deviation, where the outflow is on average located for the galaxies with significant correlation is observed compared to the galaxies showing non-significant correlation. In the *right panel* the Kendall τ distribution of the analysed correlation for the total sample is shown. The clear shift towards positive values indicates a real trend of a positive correlation.

First, a correlation between the SFR and the kinematically elevated spaxel of ionized gas is checked for every galaxy in the fossil outflow sample. The filter for the elevated spaxel as in section (5.2) is applied as well as the general SNR > 5 MEGACUBES mask on the SFR map. In addition, the requirement of at least 10 matched valid spaxel is superimposed to investigate the correlation. Of the 321/390 galaxy in the sample that pass these criteria, 85 galaxy show a significant ($p < 0.01$) positive correlation with $\tau > 0$. As can be seen in figure (44), there are also galaxies that show negative correlation between the outflow velocity and the SFR. This physically unplausible result might be due to an artificial setup. Typically galaxies show higher SFR in the central region. If these measurements are now compared with a fossil outflow candidate that has larger outflow velocities towards the galaxy outskirts and lower velocities towards the center a negative

correlation is observed by construction. This might explain the trend that can be seen in figure (45) for galaxy 9891-1901 that shows the lowest p-value for negative correlation.

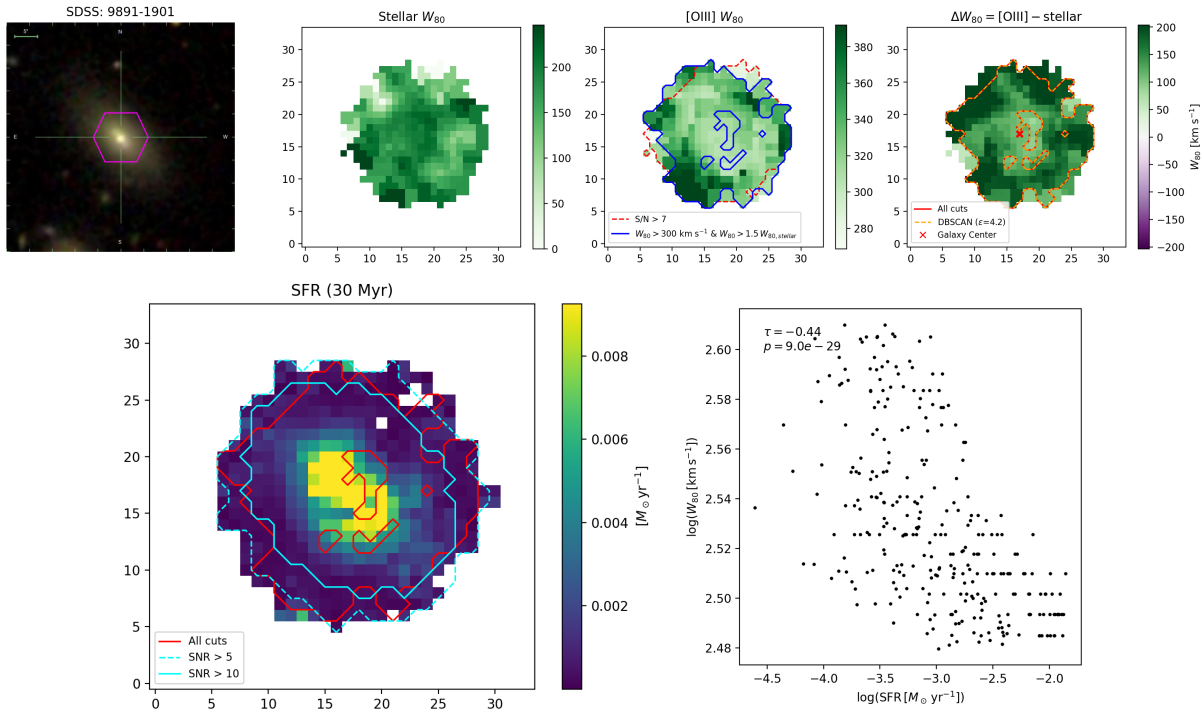

Figure 45. Example for a galaxy showing negative correlation between the outflow velocity and the SFR. The *top panel row* is the same as in figure (33) but for galaxy 9891-1901. In the lower left panel the SFR map is shown with the kinematically elevated region contoured in red and respectively SNR > 10 and SNR > 10 in solid and dashed cyan contours. The spaxelwise elevated W_{80} values against the SFR in a double log plot is shown in the *bottom right panel*. The corresponding τ correlation value and p-value are exhibited in the top left corner of the panel and show a significant negative correlation.

Similarly, one can assume a positive correlation is constructed, when only strong central ionized gas kinematics are detected that drop with distance to the center. But the fact that galaxies with positive correlation have elevated gas kinematics similarly spatially spread over comparable distances to the galaxy center as for the galaxies not showing significant correlation (figure (44) top panel) does not support this picture. Also, the shifted distribution of τ towards positive values, which can be seen in the right panel in figure (44), indicates a real trend of a positive correlation for some galaxies. Examples for galaxies that show a positive correlation can be seen in figure (46).

6.4.2 Global correlation for fossil outflow sample

Because outflows caused by SF over a larger timespan propagate away from the origin region it is useful to also look on globally integrated values for the individual galaxies in the sample. As mentioned in section (1.2.2), Heckman et al. (2015) found a correlation between the global outflow velocities of starburst galaxies and the SFR. They used a sam-

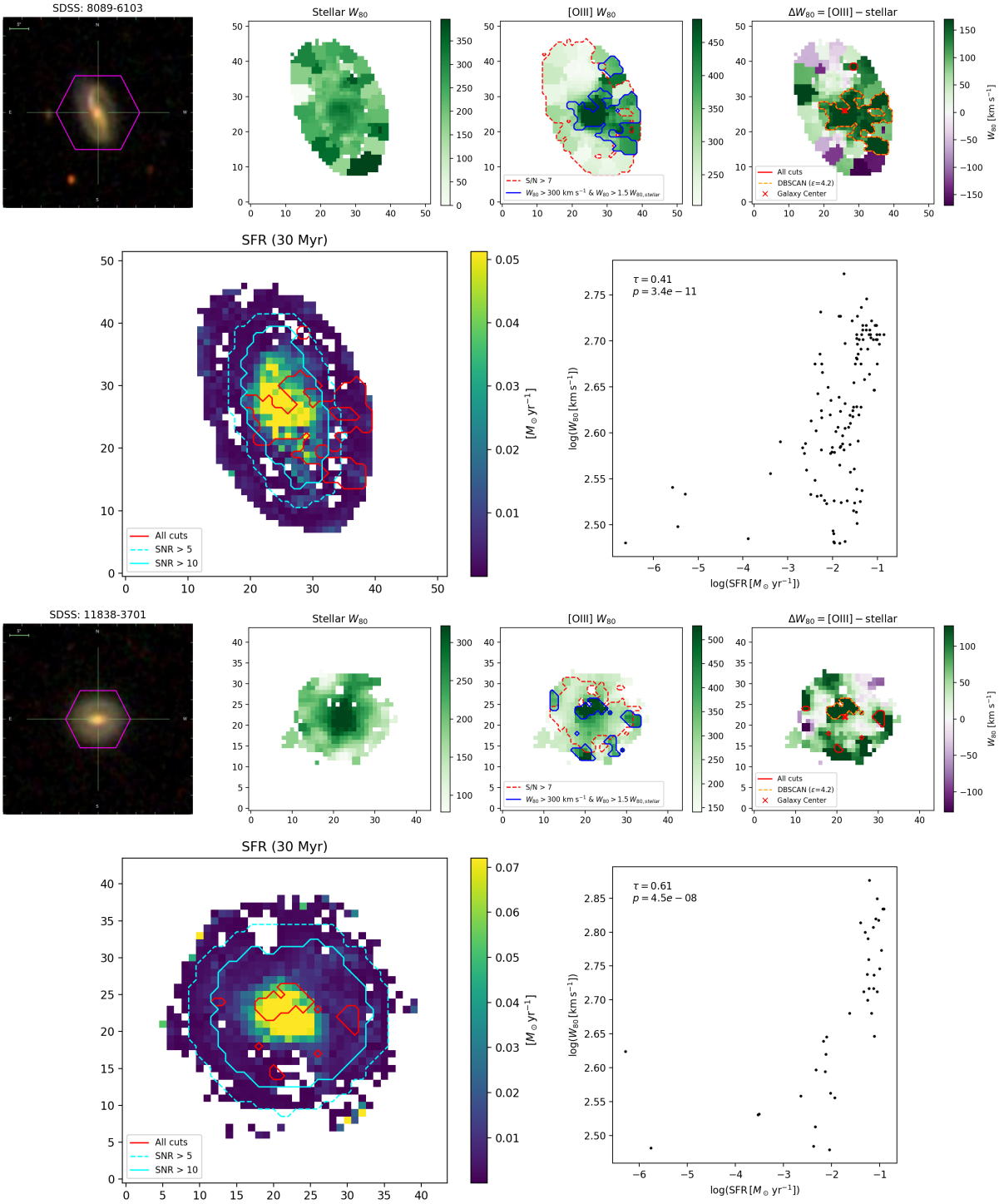

Figure 46. Examples for galaxies showing a positive spaxelwise correlation between v_{out} and the SFR. The same panels as in figure (46) are shown except for galaxies 8089-6103 and 11838-3701. In galaxy 8089-6103 a lobsided galaxy wide kinematically elevated gas outflow is observed that correlates well with the SFR. In galaxy 11838-3701 the elevated region is more constraint to a small region right above the galaxy core. Here also a significant correlation is determined but only a smaller number of spaxel contribute to the relation and the outflow is mainly detetcted at central regions at generally higher SFR.

ple of low redshift ($z < 0.2$) starburst galaxies observed in UV. They defined the outflow velocity measure based on the non-parametric flux-weighted line centroid of prominent absorption lines relative to the systemic velocity of the galaxy. This difference in measurement should not affect the qualitative result of the comparison (Heckman et al. 2015). The SFR here was calculated with a combination of far-UV and infrared luminosities (Kennicutt Jr. and Evans 2012). This method traces the gas over $\sim 100\,\mathrm{Myr}$ and bases on massive young stars that strongly emit in the far UV and the infrared luminosities are used for dust correction. The alternative selection of the SFR over the last 100 Myr from the MEGACUBES does not change the qualitative results. Minor differences due to the choice of different time intervals for the SFR are discussed in the appendix.

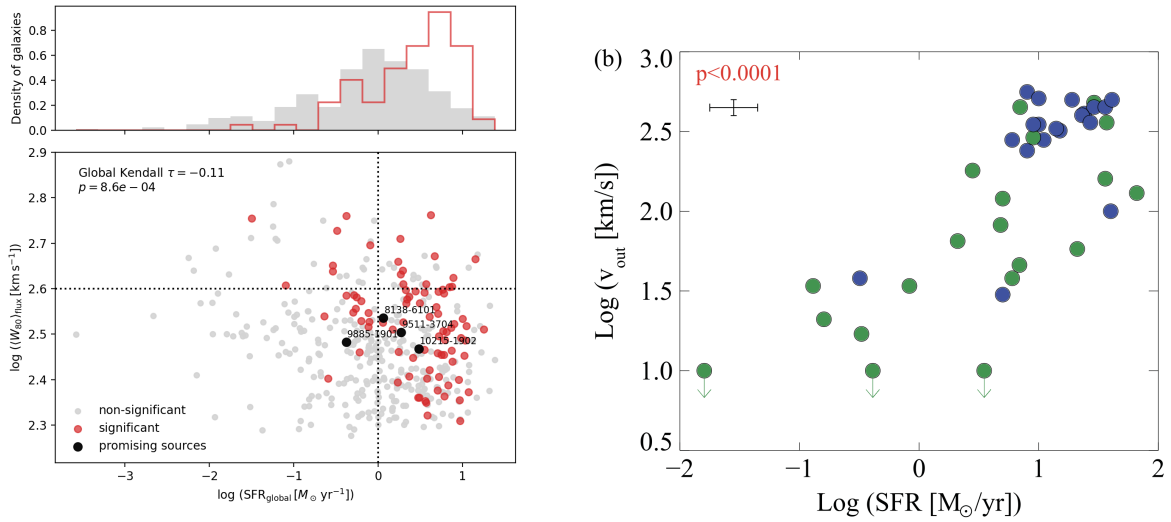

Figure 47. Global outflow properties of the flux averaged W_{80} values against the global SFR for the fossil outflow candidate sample are shown in the *lower left panel*. The red and grey dots represent respectively the galaxies in the sample that show significant and non-significant spaxelwise correlation. With also non-significant spaxelwise correlation, the black dots represent the in section (6.3) presented promising fossil outflow candidates annotated with their respective Plate-IFU number. The distribution of the global SFR show a clear tendency for the galaxies with significant spaxelwise correlation reciding at higher SFRs. In the *right panel* the global outflow velocities against the SFR are shown for a sample of starburst galaxies and show a clear positive correlation. The figure is taken from Heckman et al. (2015).

Now the global outflow velocity for the fossil outflow candidates can be calculated over flux weighted means of all spaxel with $\mathrm{SNR}_{[\mathrm{OIII}]} > 7$. For the SFR (30 Myr) again the SNR > 5 MEGACUBES mask is applied and for each galaxy all remaining spaxel are summed to a global value. Figure (47) does not show a positive correlation between the global outflow velocity and the SFR as seen for the starburst sample of Heckman et al. (2015). This implies that the kinematic elevated region in the gas in the fossil outflow candidate sample is not dominated by SF driven feedback. The sample even shows a negative correlation, which could tentatively be interpreted as a negative feedback of

stronger AGN outflows on the SFR. What is interesting is that even the galaxies that showed significant spaxelwise correlation of v_{out} and SFR follow the global negative trend. This is also not resolved when using the SFR over the past 100 Myr. But the upper left panel in figure (47) shows that as expected, these sources gather at higher global SFRs. Maybe a reason for this behavior is that through the absolute W_{80} cut the galaxies where SF driven winds play a role with lower values were removed. Those galaxies would be located in the lower left part of the scatterplot.

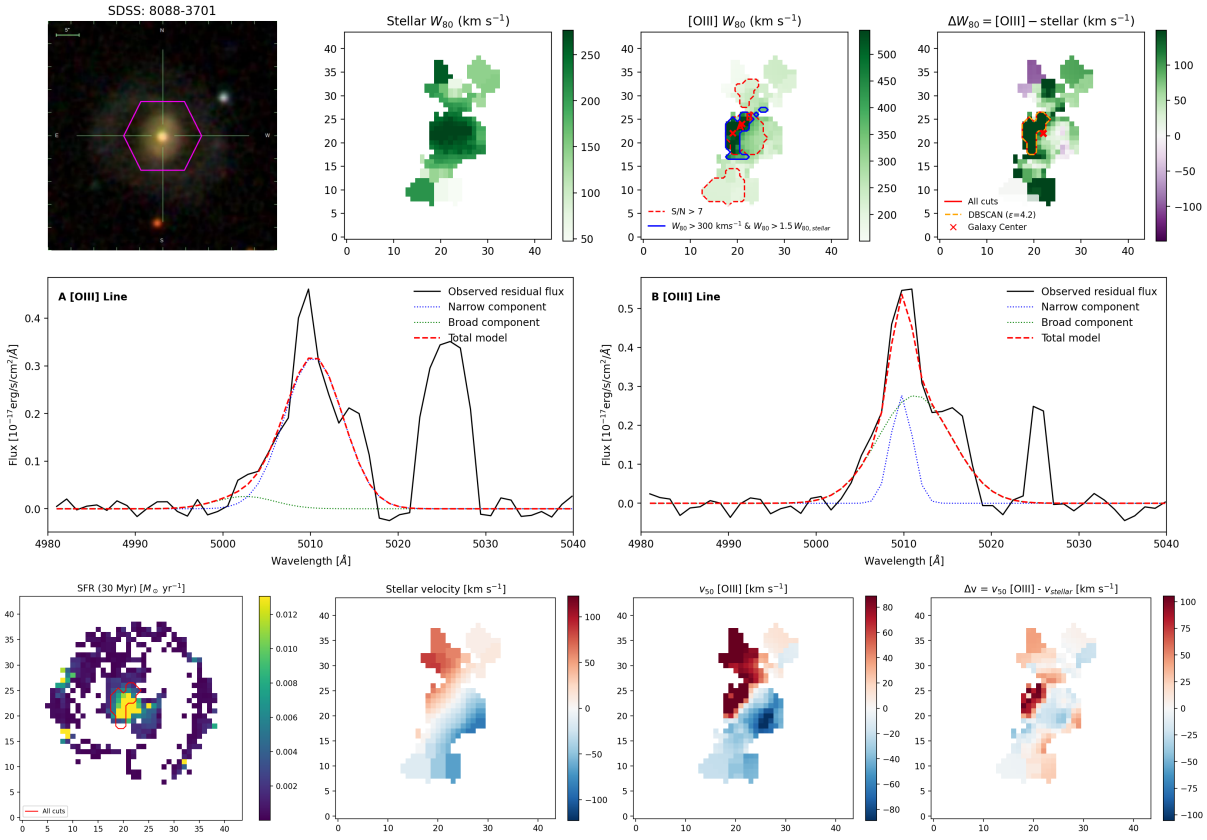

Figure 48. Maps and spectra of galaxy 8088-3701 with high outflow velocities and low SFR. The panels are the same as in figure (40) without the resolved line diagnostic diagrams.

In a last step, the sources that reside in the top left region of the plot in the lower left panel of figure (47) can be inspected. Those galaxies show low gloabl $SFR < 1 M_\odot yr^{-1}$ and a high global outflow velocity $\langle W_{80} \rangle_{flux} > 10^{2.6} \sim 400 km/s$. It shows that most galaxies in this region show strong central elevated gas signatures and overall low SNR. In this way, the outflow velocity is averaged only over high absolute values in the galaxy center and only a small region with enough SNR contributes to the SFR. Nevertheless, very interesting sources are identified in the sample like 8088-3701 in figure (48). In this galaxy a kinematically elevated gas region is detected slightly east of the galaxy center with extreme [OIII] line widths. Inspections of the line fits as seen in the spectral windows A and B show a completely detached redshifted outflow component of the [OIII] line that was not even successfully fitted. Additional inspection of other emission lines

(figure (49)) show that this secondary component is not visible in other prominent lines and the [OIII]λ4959 does not have enough signal to make a statement for a secondary component as well. Part of the large line width of $W_{80} \sim 1200\,\mathrm{km\,s^{-1}}$ can be explained with the rather face on observing angle of the galaxy. Given the minor detachment from the galaxy nucleus and the lacking detection as an AGN by any selection technique, 8088-3701 could be a candidate for a recent drastic shut down of the AGN. Another explanation could be that heavy obscuration hides central elevated gas kinematics or even ongoing AGN activity.

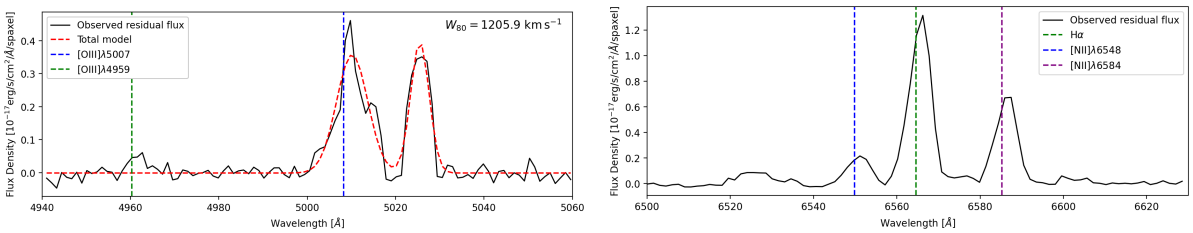

Figure 49. Spectral windows of highlighted spaxel A in figure (48) of galaxy 8088-3701. The *left panel* shows the [OIII] line doublet with the observed residual flux without the stellar continuum in black and a double Guassian fit for just the [OIII]λ5007 line resulting in a W_{80} value presented in the upper right corner. The [OIII]λ5007 and [OIII]λ4959 line vacuum rest frame positions are respectively indicated with a dashed blue and green line. In the *right panel* the spectral window around the Hα line is shown. The restframe position of Hα is showcased by a dashed green line and the two near [NII] lines in dashed blue and purple. Here no clear secondary component is visible.

6.5 Outflow age

A simple estimate of the outflow age can be calculated using $t_{age} \sim R_{out}/v_{out}$. This can be considered as the upper limit for the fossil AGN outflow since the outflow slowed down since the AGN switched off (Zubovas and Maskeliūnas 2023). However, only the projected outflow distance can be measured. The real distance is probably larger.

The outflow velocity was calculated again using the flux weighted mean of the W_{80} [OIII] line width over a 2.5" x 2.5" square, ensuring it is averaged over a region that is bigger than the PSF FWHM. For R_{out} the distance from the galaxy core to the center of the outflow region visualized by a square aperture in figure (50) is calculated. This was done for the promising sources that show a clear detachment of the nucleus.

Looking at the results in table (3) it can be seen that the outflows span a wider range in kpc scale and can be detected up to $\sim 8\,\mathrm{Myr}$ after the switch off. This is over an order of magnitude higher than the estimated typical livetime of one AGN cycle ($\sim 10^5\,\mathrm{yr}$, Schawinski et al. 2015). Of course, this estimate has to be taken with caution as no information about earlier outflow velocities and little information about the projected direction of the outflow exist.

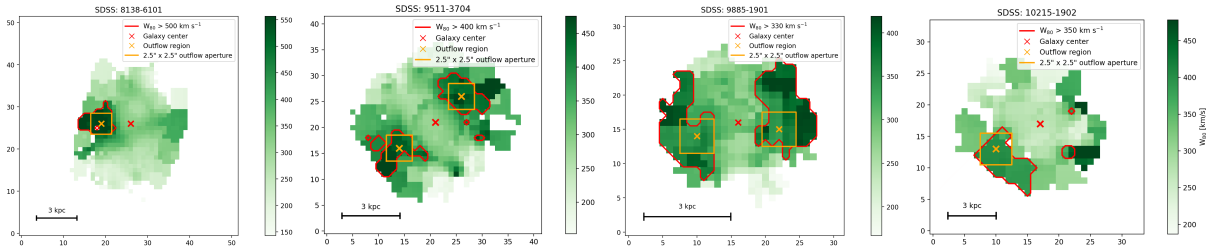

Figure 50. Visualization of the detached outflows from the galaxy center. From left to right the [OIII] W_{80} maps for the promising fossil outflow candidates 8138-6101, 9511-3704, 9885-1901 and 10215-1902 are shown. In the bottom left corner of each panel a 3 kpc physical scale for comparison is included. The galaxy center is indicated by a red cross and the orange cross and square depict the outflow region. The red outflow contours for each galaxy were chosen at a high enough absolute W_{80} value to be seperated by the less elevated regions and high enough to be considered the main outflow.

Table 3. Outflow ages for selected nucleus detached outflows.

Galaxy	R_{out} [kpc]	v_{out} [km/s]	t_{age} [Myr]
8138-6101	1.92	588	3.20
9511-3704	2.18	435	4.90
9511-3704	1.63	432	3.68
9885-1901	1.31	355	3.59
9885-1901	1.27	348	3.57
10215-1902	3.18	394	7.88

Notes. Additionally to the outflow age the flux weighted mean distance to the outflow bubble and its flux weighted mean outflow velocity is displayed. Galaxies 9511-3704 and 9885-1901 are displayed twice because two similarly strong outflow cones can be identified.

7 Conclusion and outlook

In this thesis I presented a methodic selection method for fossil outflows in the low-redshift MaNGA galaxy sample. The method uses the absolute and relative kinematic elevation of the [OIII]λ5007 emission line compared to the stellar kinematics. In this way AGN driven ionized gas outlfows can be detected that are not dominated by the galaxy gravitational potential. The absolute elevation criterion was superimposed to remove most of the detections from SF galaxies. To measure the kinematic elevation also produced by a broader secondary component, a double Gaussian emission line fit was adopted. After the selection of ionized gas regions that show kinematic elevation, those regions were clustered to form regions with extend over the spatial resolution. For clustering, a combination of the DBSCAN algorithm and the CCL algorithm was used to select all galaxies with elevated regions that are connected or lie sufficiently dense together. After subtraction of a multiwavelength selected AGN sample, 390 fossil outflow candidates were detected out of the 9,041 initial non-AGN galaxies. In this sample there are a number of disturbed systems from ongoing or recent galaxy mergers where the selection for kinematical disturbances is not valid anymore. Also some probable false detections are discussed in a visual inspection that are a result of a low chosen [OIII] line SNR and voronoi binned regions of stellar kinematics that do not reproduce the desired formally correct SNR in the galaxy outskirts.

To conclude the discussion of the selection method in section (6), the biggest limiting factor is the signal quality of the [OIII] line. In order to detect fossil outflows, it needs to be possible to trace the [OIII] line width away from the galaxy center. The [OIII] SNR > 7 criterion alone excludes 2,542 galaxies, leaving no spaxel above the threshold. For the remaining galaxies it is still possible that they display elevated gas kinematics at larger distances from the galaxy core with not sufficient SNR as showcased in section (6.1.1). Here a galaxy is discussed that shows AGN signatures from line diagnostics in the polar regions and was therefore selected as an AGN by the resolved optical diagnostics method (Jaison et al. in preparation). This caveat for the implemented selection method indicates that the found number of fossil outflow candidates pose a low estimate of the real number of the total number of fossil outflows in the entire sample. Additionally, AGN need to provide sufficient luminosity to be able to push gas out of the galactic potential (Zubovas and King 2012). Since most MaNGA selected AGN are low- to intermediate-luminosity sources with $L_{[\mathrm{OIII}]} \sim 10^{40}\,\mathrm{erg\,s^{-1}}$ (Wylezalek et al. 2018) some lower luminosity candidates were exists discarded by the absolute gas elevation cut. Moreover, smaller scale outflows driven by those lower luminosity sources could be missed because of the limitations in spatial resolution (Wylezalek et al. 2017). Nevertheless, the number of detections hints towards the confirmation that fossil AGN outflows are no rare phanomenon even in nearby low luminosity galaxies. The main conclusions from the analysis of this fossil outflow

candidate sample are summarized below.

(i) The mass outflow rates and energy rates of the fossil outflow candidates show a broader distribution stretching to lower values than found for an optically selected AGN sample. A significant proportion of the fossil outflow candidates show comparable mass outflow and energy rates and the tail towards higher values reach similar maximal values as observed for AGN.

(ii) Some galaxies in the fossil outflow candidate sample show significant spaxelwise correlation between the outflow velocity of the kinematically elevated region and the SFR. Those galaxies generally recide in global higher SFRs compared to the other galaxies in the sample. However, the global trend for the entire sample shows no positive correlation and also none for just the galaxies that show spaxelwise correlation. This indicates no significant contribution of SF driven feedback in the selected sample. If all, a negative correlation between the global outflow velocity and SFR is observed which could tentatively be interpreted as a negative feedback of stronger AGN outflows on the SF.

(iii) Through visual inspection and selection with low global SFR and high outflow velocities some promising fossil outflow candidates in different stages in their lifecycle are discussed. Some show no or minor detachment from the galaxy nucleus with large line widths and for others clear detached and sometimes lobsided biconical outflows are observed. Comparison with resolved line diagnostic maps often show coinciding AGN signatures with the detected kinematically elevated regions but in some cases for those regions just composite or even SF signatures are reported.

(iv) Simple estimates of the outflow age of promising fossil outflow candidates that show clear detachment from the galaxy nucleus hint towards a detactable outflow up $\sim 8\,\mathrm{Myr}$ after the AGN switch off.

In future work the selection method could be improved by avoiding the absolute W_{80} cut so weaker fossil AGN outflows are still detected. The mass and luminosity distribution of the fossil outflow candidate sample among the total MaNGA sample could also be investigated. Since it was only possible to trace the ionized gas kinematics with the MaNGA data, additional data in other wavelengths to analyse the atomic and molecular gas kinematics would be interesting because fossil AGN outflows are predicted to have a multiphase structure.

References

Abdurro'uf et al. (2022). "The Seventeenth Data Release of the Sloan Digital Sky Surveys: Complete Release of MaNGA, MaStar, and APOGEE-2 Data". In: *The Astrophysical Journal Supplement Series* 259.2, 35, p. 35. DOI: 10.3847/1538-4365/ac4414. arXiv: 2112.02026 [astro-ph.GA].

Aguado, D. S. et al. (2019). "The Fifteenth Data Release of the Sloan Digital Sky Surveys: First Release of MaNGA-derived Quantities, Data Visualization Tools, and Stellar Library". In: *The Astrophysical Journal Supplement Series* 240.2, p. 23. DOI: 10.3847/1538-4365/aaf651.

Aird, J. et al. (2010). "The evolution of the hard X-ray luminosity function of AGN". In: *Monthly Notices of the Royal Astronomical Society* 401.4, pp. 2531–2551. DOI: 10.1111/j.1365-2966.2009.15829.x. arXiv: 0910.1141 [astro-ph.CO].

Albán, M. (2022). "Mapping Ionized Gas Outflows in AGNs Selected from the SDSS-MaNGA Survey". Masterarbeit. Heidelberg, Germany: Ruprecht-Karls-Universität Heidelberg, Fakultät für Physik und Astronomie.

Albán, M. and D. Wylezalek (2023). "Classifying the full SDSS-IV MaNGA Survey using optical diagnostic diagrams: presentation of AGN catalogs in flexible apertures". In: *Astronomy & Astrophysics* 674, A85. DOI: 10.1051/0004-6361/202245437.

Albán, M. et al. (2024). "Mapping AGN winds: A connection between radio-mode AGNs and the AGN feedback cycle". In: *Astronomy & Astrophysics* 691, A124. DOI: 10.1051/0004-6361/202451738.

Alexander, D. M. and R. C. Hickox (2012). "What drives the growth of black holes?" In: *New Astronomy Reviews* 56.4, pp. 93–121. DOI: 10.1016/j.newar.2011.11.003. arXiv: 1112.1949 [astro-ph.GA].

Alexander, D. M. et al. (2025). "What drives the growth of black holes: a decade of progress". In: *New Astronomy Reviews*. DOI: 10.48550/arXiv.2506.19166. arXiv: 2506.19166 [astro-ph.GA].

Allington-Smith, J. and R. Content (1998). "Sampling and Background Subtraction in Fiber-Lenslet Integral Field Spectrographs". In: *Publications of the Astronomical Society of the Pacific* 110.752, p. 1216. DOI: 10.1086/316239.

Antonucci, R. (1993). "Unified models for active galactic nuclei and quasars." In: *Annual Review of Astronomy and Astrophysics* 31, pp. 473–521. DOI: 10.1146/annurev.aa.31.090193.002353.

Assef, R. J. et al. (2013). "Mid-infrare selection of active galactic nuclei with the Wide-field Infrared Survey Explorer. II. Properties of WISE-selected active galactic nuclei in the NDWFS boötes field." In: *The Astrophysical Journal* 772.1, p. 26. DOI: 10.1088/0004-637X/772/1/26.

Baldry, I. K. et al. (2004). "Quantifying the Bimodal Color-Magnitude Distribution of Galaxies". In: *The Astrophysical Journal* 600.2, pp. 681–694. DOI: 10.1086/380092. arXiv: astro-ph/0309710 [astro-ph].

Baldwin, J. A., M. M. Phillips, and R. Terlevich (1981). "Classification parameters for the emission-line spectra of extragalactic objects." In: *Publications of the Astronomical Society of the Pacific* 93, pp. 5–19. DOI: 10.1086/130766.

Barger, A. (2004). *Supermassive Black Holes in the Distant Universe*. Dordrecht: Kluwer Academic Publishers. ISBN: 978-90-481-6662-6. DOI: 10.1007/978-1-4020-2471-9.

Barthelmy, S. D. et al. (2005). "The Burst Alert Telescope (BAT) on the SWIFT Midex Mission". In: *Space Science Reviews* 120.3-4, pp. 143–164. DOI: 10.1007/s11214-005-5096-3. arXiv: astro-ph/0507410 [astro-ph].

Becker, R. H., R. L. White, and D. J. Helfand (1995). "The FIRST Survey: Faint Images of the Radio Sky at Twenty Centimeters". In: *The Astrophysical Journal* 450, p. 559. DOI: 10.1086/176166.

Belfiore, F. et al. (2019). "The Data Analysis Pipeline for the SDSS-IV MaNGA IFU Galaxy Survey: Emission-line Modeling". In: *The Astronomical Journal* 158.4, p. 160. DOI: 10.3847/1538-3881/ab3e4e. arXiv: 1901.00866 [astro-ph.IM].

Bell, E. F. et al. (2004). "Nearly 5000 Distant Early-Type Galaxies in COMBO-17: A Red Sequence and Its Evolution since z~1". In: *The Astrophysical Journal* 608.2, pp. 752–767. DOI: 10.1086/420778. arXiv: astro-ph/0303394 [astro-ph].

Brinchmann, J. et al. (2004). "The physical properties of star-forming galaxies in the low-redshift Universe". In: *Monthly Notices of the Royal Astronomical Society* 351.4, pp. 1151–1179. DOI: 10.1111/j.1365-2966.2004.07881.x. arXiv: astro-ph/0311060 [astro-ph].

Bundy, K. et al. (2015). "Overview of the SDSS-IV MaNGA Survey: Mapping Nearby Galaxies at Apache Point Observatory". In: *The Astrophysical Journal* 798.1, p. 7. DOI: 10.1088/0004-637X/798/1/7.

Cappellari, M. (2016). "Improving the full spectrum fitting method: accurate convolution with Gauss–Hermite functions". In: *Monthly Notices of the Royal Astronomical Society* 466.1, pp. 798–811. ISSN: 0035-8711. DOI: 10.1093/mnras/stw3020.

Cappellari, M. and Y. Copin (2003). "Adaptive spatial binning of integral-field spectroscopic data using Voronoi tessellations". In: *Monthly Notices of the Royal Astronomical Society* 342.2, pp. 345–354. ISSN: 0035-8711. DOI: 10.1046/j.1365-8711.2003.06541.x.

Cappellari, M. and E. Emsellem (2004). "Parametric Recovery of Line-of-Sight Velocity Distributions from Absorption-Line Spectra of Galaxies via Penalized Likelihood". In: *Publications of the Astronomical Society of the Pacific* 116.816, pp. 138–147. DOI: 10.1086/381875.

Carniani, S. et al. (2015). "Ionised outflows in z ~2.4 quasar host galaxies". In: *Astronomy & Astrophysics* 580, A102. DOI: 10.1051/0004-6361/201526557. URL: https://doi.org/10.1051/0004-6361/201526557.

Chen, Y. et al. (2010). "Absorption-line Probes of the Prevalence and Properties of Outflows in Present-day Star-forming Galaxies". In: *The Astronomical Journal* 140.2, pp. 445–461. DOI: 10.1088/0004-6256/140/2/445. arXiv: 1003.5425 [astro-ph.GA].

Cherinka, B. et al. (2019). "Marvin: A Toolkit for Streamlined Access and Visualization of the SDSS-IV MaNGA Data Set". In: *The Astronomical Journal* 158.2, p. 74. DOI: 10.3847/1538-3881/ab2634.

Chevalier, R. A. and A. W. Clegg (1985). "Wind from a starburst galaxy nucleus". In: *Nature* 317.6032, pp. 44–45. DOI: 10.1038/317044a0.

Cicone, C., R. Maiolino, and A. Marconi (2016). "Outflows and complex stellar kinematics in SDSS star-forming galaxies". In: *Astronomy & Astrophysics* 588, A41, A41. DOI: 10.1051/0004-6361/201424514. arXiv: 1601.04715 [astro-ph.GA].

Cid Fernandes, R. et al. (2011). "A comprehensive classification of galaxies in the Sloan Digital Sky Survey: how to tell true from fake AGN?" In: *Monthly Notices of the Royal Astronomical Society* 413.3, pp. 1687–1699. DOI: 10.1111/j.1365-2966.2011.18244.x. arXiv: 1012.4426 [astro-ph.CO].

Comerford, J. M. et al. (2024). "An Excess of Active Galactic Nuclei Triggered by Galaxy Mergers in MaNGA Galaxies of Stellar Mass 1011M". In: *The Astrophysical Journal* 963.1, p. 53. DOI: 10.3847/1538-4357/ad1a15.

Condon, J. J. et al. (1998). "The NRAO VLA Sky Survey". In: *The Astronomical Journal* 115.5, pp. 1693–1716. DOI: 10.1086/300337.

Conroy, C. (2013). "Modeling the Panchromatic Spectral Energy Distributions of Galaxies". In: *Annual Review of Astronomy and Astrophysics* 51.1, pp. 393–455. DOI: 10.1146/annurev-astro-082812-141017. arXiv: 1301.7095 [astro-ph.CO].

Dall'Agnol de Oliveira, B. et al. (2021). "Gauging the effect of supermassive black holes feedback on quasar host galaxies". In: *Monthly Notices of the Royal Astronomical Society* 504.3, pp. 3890–3908. ISSN: 1365-2966. DOI: 10.1093/mnras/stab1067.

DeBuhr, J., E. Quataert, and C. Ma (2012). "Galaxy-scale outflows driven by active galactic nuclei: AGN-driven galactic winds". In: *Monthly Notices of the Royal Astronomical Society* 420.3, pp. 2221–2231. ISSN: 0035-8711. DOI: 10.1111/j.1365-2966.2011.20187.x.

Dimitrijević, M. S. et al. (2007). "The flux ratio of the [O III] $\lambda\lambda$5007, 4959 lines in AGN: Comparison with theoretical calculations". In: *Monthly Notices of the Royal Astronomical Society* 374.3, pp. 1181–1188. DOI: 10.1111/j.1365-2966.2006.11238.x.

Dubois, Y. et al. (2016). "The Horizon-AGN simulation: morphological diversity of galaxies promoted by AGN feedback". In: *Monthly Notices of the Royal Astronomical Society* 463.4, pp. 3948–3964. ISSN: 0035-8711. DOI: 10.1093/mnras/stw2265.

Ester, M. et al. (1996). "A Density-Based Algorithm for Discovering Clusters in Large Spatial Databases with Noise". In: *Second International Conference on Knowledge Discovery and Data Mining (KDD'96). Proceedings of a conference held August 2-4*. Ed. by D. W. Pfitzner and J. K. Salmon, pp. 226–331.

Fabian, A. C. (2012). "Observational Evidence of Active Galactic Nuclei Feedback". In: *Annual Review of Astronomy and Astrophysics* 50.1, pp. 455–489. ISSN: 1545-4282. DOI: 10.1146/annurev-astro-081811-125521.

Falcón-Barroso, J. et al. (2011). "An updated MILES stellar library and stellar population models". In: *Astronomy & Astrophysics* 532, A95. DOI: 10.1051/0004-6361/201116842.

Fathi, K. et al. (2005). "A bar signature and central disc in the gaseous and stellar velocity fields of NGC 5448". In: *Monthly Notices of the Royal Astronomical Society* 364.3, pp. 773–782. ISSN: 0035-8711. DOI: 10.1111/j.1365-2966.2005.09648.x.

Ferrarese, L. and D. Merritt (2000). "A Fundamental Relation between Supermassive Black Holes and Their Host Galaxies". In: *The Astrophysical Journal Letters* 539.1, pp. L9–L12. DOI: 10.1086/312838. arXiv: astro-ph/0006053 [astro-ph].

Fiore, F. et al. (2017). "AGN wind scaling relations and the co-evolution of black holes and galaxies". In: *Astronomy amp; Astrophysics* 601, A143. ISSN: 1432-0746. DOI: 10.1051/0004-6361/201629478.

Fu, Y. et al. (2023). "A complete catalogue of broad-line AGNs and double-peaked emission lines from MaNGA integral-field spectroscopy of 10K galaxies: stellar population of AGNs, supermassive black holes, and dual AGNs". In: *Monthly Notices of the Royal Astronomical Society* 524.4, pp. 5827–5843. DOI: 10.1093/mnras/stad2214. arXiv: 2305.02676 [astro-ph.GA].

Gatto, L. et al. (2024). "The extent and power of 'maintenance mode' feedback in MaNGA AGN". In: *Monthly Notices of the Royal Astronomical Society* 530.3, pp. 3059–3074. ISSN: 1365-2966. DOI: 10.1093/mnras/stae989.

Giacoumidis, E. et al. (2019). "A Blind Nonlinearity Compensator Using DBSCAN Clustering for Coherent Optical Transmission Systems". In: *Applied Sciences* 9.20. ISSN: 2076-3417. DOI: 10.3390/app9204398.

Graham, A. W. (2016). "Galaxy Bulges and Their Massive Black Holes: A Review". In: *Galactic Bulges*. Ed. by Eija Laurikainen, Reynier Peletier, and Dimitri Gadotti. Vol. 418. Astrophysics and Space Science Library, p. 263. DOI: 10.1007/978-3-319-19378-6_11. arXiv: 1501.02937 [astro-ph.GA].

Gunn, J. E. et al. (2006). "The 2.5 m Telescope of the Sloan Digital Sky Survey". In: *The Astronomical Journal* 131.4, pp. 2332–2359. DOI: 10.1086/500975. arXiv: astro-ph/0602326 [astro-ph].

Häring, N. and H. Rix (2004). "On the Black Hole Mass-Bulge Mass Relation". In: *The Astrophysical Journal Letters* 604.2, pp. L89–L92. DOI: 10.1086/383567. arXiv: astro-ph/0402376 [astro-ph].

Harris, C. R., K. J. Millman, and S. J. van der Walt (2020). "Array programming with NumPy". In: *Nature* 585, pp. 357–362. DOI: 10.1038/s41586-020-2649-2.

Harrison, C. M. (2014). "Observational constraints on the influence of active galactic nuclei on the evolution of galaxies". PhD thesis. Durham University, UK.

Harrison, C. M. et al. (2012). "Energetic galaxy-wide outflows in high-redshift ultraluminous infrared galaxies hosting AGN activity: IFU spectroscopy of high-zULIRGs hosting AGNs". In: *Monthly Notices of the Royal Astronomical Society* 426.2, pp. 1073–1096. ISSN: 0035-8711. DOI: 10.1111/j.1365-2966.2012.21723.x.

Heckman, T. M. (1980). "An Optical and Radio Survey of the Nuclei of Bright Galaxies - Activity in the Normal Galactic Nuclei". In: *Astronomy & Astrophysics* 87, p. 152.

Heckman, T. M., L. Armus, and G. K. Miley (1990). "On the Nature and Implications of Starburst-driven Galactic Superwinds". In: *The Astrophysical Journal Supplement Series* 74, p. 833. DOI: 10.1086/191522.

Heckman, T. M. and P. N. Best (2014). "The Coevolution of Galaxies and Supermassive Black Holes: Insights from Surveys of the Contemporary Universe". In: *Annual Review of Astronomy and Astrophysics* 52, pp. 589–660. DOI: 10.1146/annurev-astro-081913-035722. arXiv: 1403.4620 [astro-ph.GA].

Heckman, T. M. et al. (2000). "Absorption-Line Probes of Gas and Dust in Galactic Superwinds". In: *The Astrophysical Journal Supplement Series* 129.2, p. 493. DOI: 10.1086/313421.

Heckman, T. M. et al. (2004). "Present-Day Growth of Black Holes and Bulges: The Sloan Digital Sky Survey Perspective". In: *The Astrophysical Journal* 613.1, p. 109. DOI: 10.1086/422872.

Heckman, T. M. et al. (2015). "The Systematic Properties of the Warm Phase of Starburst-Driven Galactic Winds". In: *The Astrophysical Journal* 809.2, 147, p. 147. DOI: 10.1088/0004-637X/809/2/147. arXiv: 1507.05622 [astro-ph.GA].

Ho, L. C. (2008). "Nuclear activity in nearby galaxies." In: *Annual Review of Astronomy and Astrophysics* 46, pp. 475–539. DOI: 10.1146/annurev.astro.45.051806.110546. arXiv: 0803.2268 [astro-ph].

Hogg, D. W. (2000). *Distance measures in cosmology*. arXiv: astro-ph/9905116 [astro-ph].

Horvath, J. (2022). *High-Energy Astrophysics*. English. Springer Cham. ISBN: 978-3-030-92159-0. DOI: 10.1007/978-3-030-92159-0.

Hubble, E. P. (1926). "Extragalactic nebulae." In: *The Astrophysical Journal* 64, pp. 321–369. DOI: 10.1086/143018.

Hunter, J. D. (2007). "Matplotlib: A 2D Graphics Environment". In: *Computing in Science Engineering* 9.3, pp. 90–95. DOI: 10.1109/MCSE.2007.55.

Ilha, G. S. et al. (2019). "The first 62 AGN observed with SDSS-IV MaNGA - III: stellar and gas kinematics". In: *Monthly Notices of the Royal Astronomical Society* 484.1, pp. 252–268. DOI: 10.1093/mnras/sty3373. arXiv: 1903.08071 [astro-ph.GA].

Józsa, G. I. G. et al. (2009). "Revealing Hanny's Voorwerp: radio observations of IC 2497". In: *Astronomy & Astrophysics* 500.2, pp. L33–L36. DOI: 10.1051/0004-6361/200912402.

Kakkad, D. et al. (2018). "Spatially resolved electron density in the narrow line region of z < 0.02 radio AGNs". In: *Astronomy & Astrophysics* 618, A6. DOI: 10.1051/0004-6361/201832790.

Kauffmann, G., T. M. Heckman, and P. N. Best (2008). "Radio jets in galaxies with actively accreting black holes: new insights from the SDSS". In: *Monthly Notices of the Royal Astronomical Society* 384.3, pp. 953–971. ISSN: 0035-8711. DOI: 10.1111/j.1365-2966.2007.12752.x.

Kauffmann, G. et al. (2003a). "The dependence of star formation history and internal structure on stellar mass for 105 low-redshift galaxies". In: *Monthly Notices of the Royal Astronomical Society* 341.1, pp. 54–69. ISSN: 0035-8711. DOI: 10.1046/j.1365-8711.2003.06292.x.

Kauffmann, G. et al. (2003b). "The host galaxies of active galactic nuclei". In: *Monthly Notices of the Royal Astronomical Society* 346.4, pp. 1055–1077. DOI: 10.1111/j.1365-2966.2003.07154.x. arXiv: astro-ph/0304239 [astro-ph].

Keel, W. C. et al. (2012a). "The Galaxy Zoo survey for giant AGN-ionized clouds: past and present black hole accretion events". In: *Monthly Notices of the Royal Astronomical Society* 420.1, pp. 878–900. DOI: 10.1111/j.1365-2966.2011.20101.x. arXiv: 1110.6921 [astro-ph.CO].

Keel, W. C. et al. (2012b). "The History and Environment of a Faded Quasar: Hubble Space Telescope Observations of Hanny's Voorwerp and IC 2497". In: *The Astronomical Journal* 144.2, 66, p. 66. DOI: 10.1088/0004-6256/144/2/66. arXiv: 1206.3797 [astro-ph.CO].

Kellermann, K. I. et al. (1989). "VLA Observations of Objects in the Palomar Bright Quasar Survey". In: *The Astronomical Journal* 98, p. 1195. DOI: 10.1086/115207.

Kendall, M. G. (1949). "Rank Correlation Methods". In: *Journal of the Institute of Actuaries* 75.1, pp. 140–141. DOI: 10.1017/S0020268100013019.

Kennicutt Jr., R. C. (1992). "The Integrated Spectra of Nearby Galaxies: General Properties and Emission-Line Spectra". In: *The Astrophysical Journal* 388, p. 310. DOI: 10.1086/171154.

Kennicutt Jr., R. C. and N. J. Evans (2012). "Star Formation in the Milky Way and Nearby Galaxies". In: *Annual Review of Astronomy and Astrophysics* 50.Volume 50, 2012, pp. 531–608. ISSN: 1545-4282. DOI: 10.1146/annurev-astro-081811-125610.

Kewley, L. J., D. C. Nicholls, and R. S. Sutherland (2019). "Understanding Galaxy Evolution Through Emission Lines". In: *Annual Review of Astronomy and Astrophysics* 57, pp. 511–570. DOI: 10.1146/annurev-astro-081817-051832. arXiv: 1910.09730 [astro-ph.GA].

Kewley, L. J. et al. (2001). "Theoretical Modeling of Starburst Galaxies". In: *The Astrophysical Journal* 556.1, pp. 121–140. DOI: 10.1086/321545. arXiv: astro-ph/0106324 [astro-ph].

Kewley, L. J. et al. (2006). "The host galaxies and classification of active galactic nuclei". In: *Monthly Notices of the Royal Astronomical Society* 372.3, pp. 961–976. DOI: 10.1111/j.1365-2966.2006.10859.x. arXiv: astro-ph/0605681 [astro-ph].

Kormendy, J. and R. Bender (1996). "A Proposed Revision of the Hubble Sequence for Elliptical Galaxies". In: *The Astrophysical Journal Letters* 464, p. L119. DOI: 10.1086/310095.

Kormendy, J. and R. C. Kennicutt Jr. (2004). "Secular Evolution and the Formation of Pseudobulges in Disk Galaxies". In: *Annual Review of Astronomy and Astrophysics* 42.1, pp. 603–683. DOI: 10.1146/annurev.astro.42.053102.134024. arXiv: astro-ph/0407343 [astro-ph].

Law, D. R. et al. (2016). "The Data Reduction Pipeline for the SDSS-IV MaNGA IFU Galaxy Survey". In: *The Astronomical Journal* 152.4, p. 83. DOI: 10.3847/0004-6256/152/4/83.

Law, D. R. et al. (2022). "SDSS-IV MaNGA: Understanding Ionized Gas Turbulence Using Integral Field Spectroscopy of 4500 Star-forming Disk Galaxies". In: *The Astrophysical Journal* 928.1, p. 58. DOI: 10.3847/1538-4357/ac5620.

Leitherer, C. et al. (1999). "Starburst99: Synthesis Models for Galaxies with Active Star Formation". In: *The Astrophysical Journal Supplement Series* 123.1, pp. 3–40. DOI: 10.1086/313233. arXiv: astro-ph/9902334 [astro-ph].

Lilly, S. J. et al. (2013). "Gas Regulation of Galaxies: The Evolution of the Cosmic Specific Star Formation Rate, the Metallicity-Mass-Star-formation Rate Relation, and the Stellar Content of Halos". In: *The Astrophysical Journal* 772.2, 119, p. 119. DOI: 10.1088/0004-637X/772/2/119. arXiv: 1303.5059 [astro-ph.CO].

Lintott, C. J. et al. (2008). "Galaxy Zoo: morphologies derived from visual inspection of galaxies from the Sloan Digital Sky Survey". In: *Monthly Notices of the Royal Astronomical Society* 389.3, pp. 1179–1189. DOI: 10.1111/j.1365-2966.2008.13689.x. arXiv: 0804.4483 [astro-ph].

Lintott, C. J. et al. (2009). "Galaxy Zoo: 'Hanny's Voorwerp', a quasar light echo?" In: *Monthly Notices of the Royal Astronomical Society* 399.1, pp. 129–140. DOI: 10.1111/j.1365-2966.2009.15299.x. arXiv: 0906.5304 [astro-ph.CO].

Lintott, C. J. et al. (2011). "Galaxy Zoo 1: data release of morphological classifications for nearly 900 000 galaxies". In: *Monthly Notices of the Royal Astronomical Society*

410.1, pp. 166–178. DOI: 10.1111/j.1365-2966.2010.17432.x. arXiv: 1007.3265 [astro-ph.GA].

Liu, G. et al. (2013). "Observations of feedback from radio-quiet quasars - II. Kinematics of ionized gas nebulae". In: *Monthly Notices of the Royal Astronomical Society* 436.3, pp. 2576–2597. DOI: 10.1093/mnras/stt1755. arXiv: 1305.6922 [astro-ph.CO].

López-Cobá, C. et al. (2022). "Exploring Stellar and Ionized Gas Noncircular Motions in Barred Galaxies with MUSE". In: *The Astrophysical Journal* 939.1, 40, p. 40. DOI: 10.3847/1538-4357/ac937b. arXiv: 2207.07906 [astro-ph.GA].

Madau, P. and M. Dickinson (2014). "Cosmic Star-Formation History". In: *Annual Review of Astronomy and Astrophysics* 52.1, pp. 415–486. ISSN: 1545-4282. DOI: 10.1146/annurev-astro-081811-125615.

Madau, P. et al. (1996). "High-redshift galaxies in the Hubble Deep Field: colour selection and star formation history to z~4". In: *Monthly Notices of the Royal Astronomical Society* 283.4, pp. 1388–1404. DOI: 10.1093/mnras/283.4.1388. arXiv: astro-ph/9607172 [astro-ph].

Magorrian, J. et al. (1998). "The Demography of Massive Dark Objects in Galaxy Centers". In: *The Astronomical Journal* 115.6, pp. 2285–2305. DOI: 10.1086/300353. arXiv: astro-ph/9708072 [astro-ph].

Marconi, A. and L. K. Hunt (2003). "The Relation between Black Hole Mass, Bulge Mass, and Near-Infrared Luminosity". In: *The Astrophysical Journal Letters* 589.1, pp. L21–L24. DOI: 10.1086/375804. arXiv: astro-ph/0304274 [astro-ph].

Marconi, A. et al. (2004). "Local supermassive black holes, relics of active galactic nuclei and the X-ray background". In: *Monthly Notices of the Royal Astronomical Society* 351.1, pp. 169–185. DOI: 10.1111/j.1365-2966.2004.07765.x. arXiv: astro-ph/0311619 [astro-ph].

McKinney, W. (2010). "Data Structures for Statistical Computing in Python". In: *Proceedings of the 9th Python in Science Conference*. Ed. by Stéfan van der Walt and Jarrod Millman, pp. 56–61. DOI: 10.25080/Majora-92bf1922-00a.

Merloni, A. and S. Heinz (2007). "Measuring the kinetic power of active galactic nuclei in the radio mode". In: *Monthly Notices of the Royal Astronomical Society* 381.2, pp. 589–601. ISSN: 0035-8711. DOI: 10.1111/j.1365-2966.2007.12253.x.

Mogotsi, K. M. et al. (2016). "H I and CO Velocity Dispersions in Nearby Galaxies". In: *The Astronomical Journal* 151.1, 15, p. 15. DOI: 10.3847/0004-6256/151/1/15. arXiv: 1511.06006 [astro-ph.GA].

Morganti, R. (2017). "Archaeology of active galaxies across the electromagnetic spectrum". In: *Nature Astronomy* 1, pp. 596–605. DOI: 10.1038/s41550-017-0223-0. arXiv: 1709.01667 [astro-ph.GA].

Mullaney, J. R. et al. (2011). "Defining the intrinsic AGN infrared spectral energy distribution and measuring its contribution to the infrared output of composite galaxies".

In: *Monthly Notices of the Royal Astronomical Society* 414.2, pp. 1082–1110. ISSN: 0035-8711. DOI: 10.1111/j.1365-2966.2011.18448.x.

Murray, N., E. Quataert, and T. A. Thompson (2005). "On the Maximum Luminosity of Galaxies and Their Central Black Holes: Feedback from Momentum-driven Winds". In: *The Astrophysical Journal* 618.2, p. 569. DOI: 10.1086/426067.

NASA (2011). *Hanny's Voorwerp,IC 2497*. https://science.nasa.gov/asset/hubble/hubble-snaps-image-of-space-oddity/. NASA,ESA, W. Keel (University of Alabama), and the Galaxy Zoo Team.

Oh, K. et al. (2018). "The 105-month Swift-BAT All-sky Hard X-Ray Survey". In: *The Astrophysical Journal Supplement Series* 235.1, p. 4. DOI: 10.3847/1538-4365/aaa7fd.

Oh, S. et al. (2022). "The SAMI Galaxy Survey: the difference between ionized gas and stellar velocity dispersions". In: *Monthly Notices of the Royal Astronomical Society* 512.2, pp. 1765–1780. ISSN: 0035-8711. DOI: 10.1093/mnras/stac509.

Osterbrock, D. E. and G. J. Ferland (2006). *Astrophysics of gaseous nebulae and active galactic nuclei-2nd ed.* Mill Valley, California: University Science Books.

Padovani, P. et al. (2017). "Active galactic nuclei: what's in a name?" In: *The Astronomy and Astrophysics Review* 25.1. ISSN: 1432-0754. DOI: 10.1007/s00159-017-0102-9.

Pedregosa, F. et al. (2011). "Scikit-learn: Machine Learning in Python". In: *Journal of Machine Learning Research* 12.85, pp. 2825–2830. URL: http://jmlr.org/papers/v12/pedregosa11a.html.

Riffel, R. et al. (2023a). "Mapping the stellar population and gas excitation of MaNGA galaxies with MEGACUBES. Results for AGN versus control sample". In: *Monthly Notices of the Royal Astronomical Society* 524.4, pp. 5640–5657. DOI: 10.1093/mnras/stad2234. arXiv: 2307.11474 [astro-ph.GA].

Riffel, R. A. et al. (2023b). "Spatially resolved observations of outflows in the radio loud AGN of UGC 8782". In: *Monthly Notices of the Royal Astronomical Society* 521.3, pp. 3260–3272. ISSN: 1365-2966. DOI: 10.1093/mnras/stad776.

Rupke, D. S. N. and S. Veilleux (2013). "The multiphase structure and power sources of galactic winds in major mergers". In: *The Astrophysical Journal* 768.1, p. 75. ISSN: 1538-4357. DOI: 10.1088/0004-637x/768/1/75.

Rupke, D. S. N., S. Veilleux, and D. B. Sanders (2005). "Outflows in Infrared-Luminous Starbursts at z $<$ 0.5. I. Sample, Na I D Spectra, and Profile Fitting". In: *The Astrophysical Journal Supplement Series* 160.1, p. 87. DOI: 10.1086/432886.

Rybicki, G. B. and A. P. Lightman (1985). *Radiative processes in astrophysics*. New York: Wiley & Sons.

Sánchez, S. F. et al. (2022). "SDSS-IV MaNGA: pyPipe3D Analysis Release for 10,000 Galaxies". In: *The Astrophysical Journal Supplement Series* 262.2, p. 36. DOI: 10.3847/1538-4365/ac7b8f.

Sánchez, S. F. et al. (2024). "WHaD diagram: Classifying the ionizing source with one single emission line". In: *Astronomy & Astrophysics* 682, A71. DOI: 10.1051/0004-6361/202347711.

Sánchez-Blázquez, P. et al. (2006). "Medium-resolution Isaac Newton Telescope library of empirical spectra". In: *Monthly Notices of the Royal Astronomical Society* 371.2, pp. 703–718. ISSN: 0035-8711. DOI: 10.1111/j.1365-2966.2006.10699.x.

Sanders, R. L. et al. (2016). "The MOSDEF survey: electron density and ionization parameter at z ~2.3". In: *The Astrophysical Journal* 816.1, p. 23. DOI: 10.3847/0004-637X/816/1/23.

Schawinski, K. et al. (2010). "The sudden death of the nearest quasar". In: *The Astrophysical Journal Letters* 724.1, p. L30. DOI: 10.1088/2041-8205/724/1/L30.

Schawinski, K. et al. (2014). "The green valley is a red herring: Galaxy Zoo reveals two evolutionary pathways towards quenching of star formation in early- and late-type galaxies". In: *Monthly Notices of the Royal Astronomical Society* 440.1, pp. 889–907. ISSN: 0035-8711. DOI: 10.1093/mnras/stu327.

Schawinski, K. et al. (2015). "Active galactic nuclei flicker: an observational estimate of the duration of black hole growth phases of $\sim 10^5$ yr". In: *Monthly Notices of the Royal Astronomical Society* 451.3, pp. 2517–2523. DOI: 10.1093/mnras/stv1136. arXiv: 1505.06733 [astro-ph.GA].

Schiminovich, D. et al. (2007). "The UV-Optical Color Magnitude Diagram. II. Physical Properties and Morphological Evolution On and Off of a Star-forming Sequence". In: *The Astrophysical Journal Supplement Series* 173.2, pp. 315–341. DOI: 10.1086/524659. arXiv: 0711.4823 [astro-ph].

Schirmer, M. et al. (2013). "A sample of seyfert-2 galaxies with ultraluminous galaxy-wide narrow-line regions: quasar light echoes?" In: *The Astrophysical Journal* 763.1, p. 60. DOI: 10.1088/0004-637X/763/1/60.

Schneider, P. (2006). *Einführung in die Extragalaktische Astronomie und Kosmologie*. German. Lehrbuch zu Astronomie der Galaxien und Kosmologie. Berlin, Heidelberg: Springer Berlin Heidelberg, p. 452. ISBN: 978-3-540-30589-7.

Shapley, A. E. (2011). "Physical Properties of Galaxies from z = 2-4". In: *Annual Review of Astronomy and Astrophysics* 49.1, pp. 525–580. DOI: 10.1146/annurev-astro-081710-102542. arXiv: 1107.5060 [astro-ph.CO].

Stern, D., R. J. Assef, and D. J. Benford (2012). "Mid-infrared selection of active galactic nuclei with the Wide-field Infrared Survey Explorer I. characterizing WISE-selected active galactic nuclei in COSMOS". In: *The Astrophysical Journal* 753.1, p. 30. DOI: 10.1088/0004-637X/753/1/30.

Strauss, M. A. et al. (2002). "Spectroscopic Target Selection in the Sloan Digital Sky Survey: The Main Galaxy Sample". In: *The Astronomical Journal* 124.3, p. 1810. DOI: 10.1086/342343.

Su, M., T. R. Slatyer, and D. P. Finkbeiner (2010). "Giant Gamma-ray Bubbles from Fermi-LAT: Active Galactic Nucleus Activity or Bipolar Galactic Wind?" In: *The Astrophysical Journal* 724.2, pp. 1044–1082. DOI: 10.1088/0004-637X/724/2/1044. arXiv: 1005.5480 [astro-ph.HE].

Szalay, Alexander S. et al. (2002). *The SDSS SkyServer: Public Access to the Sloan Digital Sky Server Data*. arXiv: cs/0202013 [cs.DL].

The Astropy Collaboration et al. (2013). "Astropy: A community Python package for astronomy". In: *Astronomy & Astrophysics* 558, A33. DOI: 10.1051/0004-6361/201322068.

The Astropy Collaboration et al. (2018). "The Astropy Project: Building an Open-science Project and Status of the v2.0 Core Package*". In: *The Astronomical Journal* 156.3, p. 123. DOI: 10.3847/1538-3881/aabc4f.

The Astropy Collaboration et al. (2022). "The Astropy Project: Sustaining and Growing a Community-oriented Open-source Project and the Latest Major Release (v5.0) of the Core Package*". In: *The Astrophysical Journal* 935.2, p. 167. DOI: 10.3847/1538-4357/ac7c74.

Trump, J. R. et al. (2015). "The biases of optical line-ratio selection for active galactic nuclei and the intrinsic relationship between black hole accretion and galaxy star formation". In: *The Astrophysical Journal* 811.1, p. 26. DOI: 10.1088/0004-637X/811/1/26.

Urry, C. M. and P. Padovani (1995). "Unified schemes for radio-loud active galactic nuclei". In: *Publications of the Astronomical Society of the Pacific* 107.715, p. 803. DOI: 10.1086/133630.

Veilleux, S., G. Cecil, and J. Bland-Hawthorn (2005). "Galactic Winds". In: *Annual Review of Astronomy and Astrophysics* 43.1, pp. 769–826. DOI: 10.1146/annurev.astro.43.072103.150610. arXiv: astro-ph/0504435 [astro-ph].

Veilleux, S. and D. E. Osterbrock (1987). "Spectral Classification of Emission-Line Galaxies". In: *The Astrophysical Journal Supplement Series* 63, p. 295. DOI: 10.1086/191166.

Virtanen, P., R. Gommers, and T. E Oliphant (2020). "Scipy 1.0: fundamental algorithms for scientific computing in python". In: *Nature Methods* 17.3, pp. 261–272. DOI: 10.1038/s41592-019-0686-2.

Wake, D. A. et al. (2017). "The SDSS-IV MaNGA Sample: Design, Optimization, and Usage Considerations". In: *The Astronomical Journal* 154.3, p. 86. DOI: 10.3847/1538-3881/aa7ecc.

Westfall, K. B. et al. (2019). "The Data Analysis Pipeline for the SDSS-IV MaNGA IFU Galaxy Survey: Overview". In: *The Astronomical Journal* 158.6, p. 231. DOI: 10.3847/1538-3881/ab44a2.

Whitaker, K. E. et al. (2012). "The Star Formation Mass Sequence Out to z = 2.5". In: *The Astrophysical Journal Letters* 754.2, L29, p. L29. DOI: 10.1088/2041-8205/754/2/L29. arXiv: 1205.0547 [astro-ph.CO].

White, S. V. et al. (2015). "Radio-quiet quasars in the VIDEO survey: evidence for AGN-powered radio emission at $S_{1.4\,\mathrm{GHz}} < 1$ mJy". In: *Monthly Notices of the Royal Astronomical Society* 448.3, pp. 2665–2686. DOI: 10.1093/mnras/stv134. arXiv: 1410.3892 [astro-ph.GA].

Woo, J. et al. (2016). "The prevalence of gas outflows in type 2 AGNs". In: *The Astrophysical Journal* 817.2, p. 108. DOI: 10.3847/0004-637X/817/2/108.

Wright, E. L. et al. (2010). "The Wide-field Infrared Survey Explorer (WISE): mission description and initial on-orbit performance". In: *The Astronomical Journal* 140.6, p. 1868. DOI: 10.1088/0004-6256/140/6/1868.

Wylezalek, D. et al. (2017). "Zooming into local active galactic nuclei: the power of combining SDSS-IV MaNGA with higher resolution integral field unit observations". In: *Monthly Notices of the Royal Astronomical Society* 467.3, pp. 2612–2624. ISSN: 0035-8711. DOI: 10.1093/mnras/stx246.

Wylezalek, D. et al. (2018). "SDSS-IV MaNGA: identification of active galactic nuclei in optical integral field unit surveys". In: *Monthly Notices of the Royal Astronomical Society* 474.2, pp. 1499–1514. ISSN: 1365-2966. DOI: 10.1093/mnras/stx27844.

Wylezalek, D. et al. (2020). "Ionized gas outflow signatures in SDSS-IV MaNGA active galactic nuclei". In: *Monthly Notices of the Royal Astronomical Society* 492.4, pp. 4680–4696. DOI: 10.1093/mnras/staa062. arXiv: 1911.10212 [astro-ph.GA].

York, D. G. et al. (2000). "The Sloan Digital Sky Survey: Technical Summary". In: *The Astronomical Journal* 120.3, pp. 1579–1587. DOI: 10.1086/301513. arXiv: astro-ph/0006396 [astro-ph].

Zakamska, N. L. and J. E. Greene (2014). "Quasar feedback and the origin of radio emission in radio-quiet quasars". In: *Monthly Notices of the Royal Astronomical Society* 442.1, pp. 784–804. DOI: 10.1093/mnras/stu842. arXiv: 1402.6736 [astro-ph.GA].

Zubovas, K. (2018). "Massive outflow properties suggest AGN fade slowly". In: *Monthly Notices of the Royal Astronomical Society* 473.3, pp. 3525–3535. ISSN: 0035-8711. DOI: 10.1093/mnras/stx2569.

Zubovas, K., J. Bialopetravičius, and M. Kazlauskaitė (2022). "Determining active galactic nucleus luminosity histories using present-day outflow properties: a neural network-based approach". In: *Monthly Notices of the Royal Astronomical Society* 515.2, pp. 1705–1722. ISSN: 0035-8711. DOI: 10.1093/mnras/stac1887.

Zubovas, K. and A. King (2012). "Clearing out a galaxy". In: *The Astrophysical Journal Letters* 745.2, p. L34. DOI: 10.1088/2041-8205/745/2/L34.

Zubovas, K. and G. Maskeliūnas (2023). "Life after AGN switch off: evolution and properties of fossil galactic outflows". In: *Monthly Notices of the Royal Astronomical Society* 524, p. 4819. DOI: 10.1093/mnras/stad1661. arXiv: 2306.00518 [astro-ph.GA].

Zubovas, K. and S. Nayakshin (2012). "Fermi bubbles in the Milky Way: the closest AGN feedback laboratory courtesy of Sgr A*?" In: *Monthly Notices of the Royal Astronomical Society* 424.1, pp. 666–683. ISSN: 0035-8711. DOI: 10.1111/j.1365-2966.2012.21250.x.

Zubovas, K. et al. (2013). "AGN outflows trigger starbursts in gas-rich galaxies". In: *Monthly Notices of the Royal Astronomical Society* 433.4, pp. 3079–3090. DOI: 10.1093/mnras/stt952. arXiv: 1306.0684 [astro-ph.GA].

Zuo, Y. and D. Zhang (2023). "Connected Components Labeling Algorithms: A Review". In: *2023 9th International Conference on Computer and Communications (ICCC)*, pp. 1743–1748. DOI: 10.1109/ICCC59590.2023.10507420.

Appendix

A Kinematic outflow model

An important outflow property that needs additional discussion is the outflow velocity v_{out}. For emission lines, taking the orientation of the observing angle relative to the ionisation cones into account, the line of sight (LOS) velocity v_{med} offset from the emission line fitting does not represent the true velocity of the outflow. In figure (51) taken out of Harrison et al. (2012) and following their argumentation, it can be seen that the observed line width is less dependent on the orientation and is therefore a better indicator for the outflow velocity.

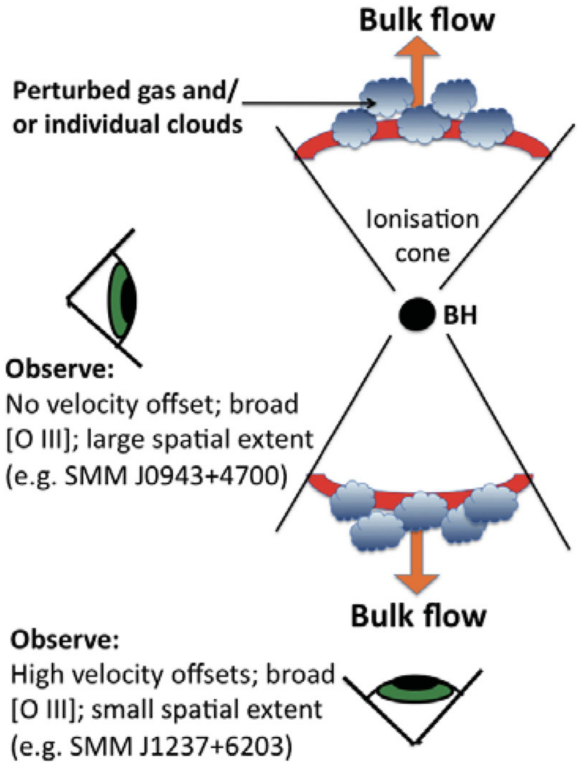

Figure 51. A schematic diagram to illustrate a possible interpretation of the observations of the broad [O III] emission lines. If a fast wind is initially launched around the central BH, it could sweep up clouds of gas in a bipolar outflow (as assumed by some models e.g. DeBuhr, Quataert, and Ma 2012; Zubovas and Nayakshin 2012). The orientation with respect to the line of sight will determine the velocity offsets and spatial extent observed; owever, broad emission lines will always be observed.

The relation between the outflow velocity and the W_{80} line width was explored in a kinematic model by Liu et al. (2013). The emission line profile $I(v_z, \mathbf{R})$ as observed in

our IFU data can be calculated from the following equation:

$$I(v_z, \mathbf{R}) = \int j(\mathbf{r})\delta(\mathbf{v} - \mathbf{v_0}(\mathbf{r}))dv_x dv_y dv_z \tag{28}$$

using the two-dimensional radius vector $\mathbf{R}$ in the image plane (x,y) and z as the coordinate along the line of sight. Assuming a spherical symmetry, a constant outflow velocity $v(r) = v_0 =$ constant and a power law function of radius from the center of the outflow $j(r) = r^{-\alpha}$ for the luminosity density $j(\mathbf{r})$, $I(v_z, R)$ is found to be a separable function of the line of sight velocity v_z and R:

$$I(v_z, R) \propto (1 - v_z^2 - v_0^2)^{\frac{1}{2}(\alpha-3)} R^{1-\alpha} \tag{29}$$

meaning that the total line intensity varies with R over the image plane but the radial velocity profile remains the same. This results in a constant W_{80} width of the line across the image plane in this model. This is due to the fact that for power law luminosity density distributions the relative contribution of the more inclined points to the LOS remains the same. The result is a linear relation of $W_{80} \simeq 1.3v_0$ depending on the slope of the surface brightness profile. It also holds for wide-angle biconical outflow models. In figure (52) the spherical outflow model and the emission line profiles for the assumptions are depicted.

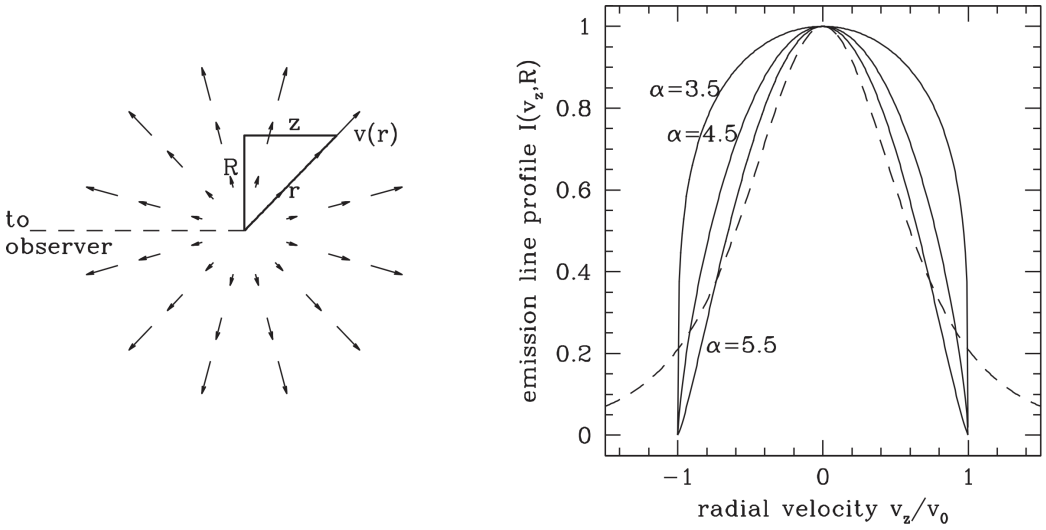

Figure 52. *On the left* a schematic of the spherical outflow models and the notation used in the calculation is depicted. *On the right* emission-line profiles are shown for models with $v(r) = v_0 =$ const. (solid lines for three different values of α which parametrizes the luminosity density profile) and $v(r) \propto r$ (dashed; $\alpha = 4.5$).

It is also important to note that deviations from spherical symmetry are required to produce asymmetric line profiles (Zakamska and Greene 2014). Throughout the literature other definitions for the outflow velocity are also used e.g. taking the tail velocity like v_{95}

of the line profile, assuming the broad component is tracing the outflow and weighting the highest velocity gas that contributes to the wings (Rupke and Veilleux 2013; Fiore et al. 2017; Dall'Agnol de Oliveira et al. 2021).

For absorption lines the bulk outflow velocity can be determined more easily. Since the absorbing material has to be in the LOS in front of the continuous emitter I_0 the observed intensity is:

$$I(v) = I_0 e^{-\tau(v)} \tag{30}$$

with the optical depth τ. Here in absence of the tail emitted behind the emission source like for the emission lines and still absent a good model for the radial dependence of the outflow velocity field, often the flux-weighted centroid of absorption-line profiles are used for the bulk outflow velocities (Heckman et al. 2000; Rupke, Veilleux, and Sanders 2005; Heckman et al. 2015).

B Star Formation Rate over 100 Myr

Here, the minor differences in the choice of the SFR of the MEGACUBES over the last 100 Myr compared to 30 Myr is discussed to justify the comparison to the SFR used by Heckman et al. (2015). In both cases the global outflow velocity and the SFR show negative correlation for the total fossil outflow sample and the galaxies that show significant spaxelwise correlation are predominantly found at larger global SFRs (figure (53)). The negative correlation found with the SFR over the last 100 Myr is even stronger and at lower p-value. The differences are, that for the SFR over 100 Myr 81/325 galaxies show significant spaxelwise positive correlation compared to 85/321 for the SFR over 30 Myr. With the SFR over the last 100 Myr more (41) sources with low global SFR and high average outflow velocity compared to before (32 at SFR over the last 30 Myr) are found.

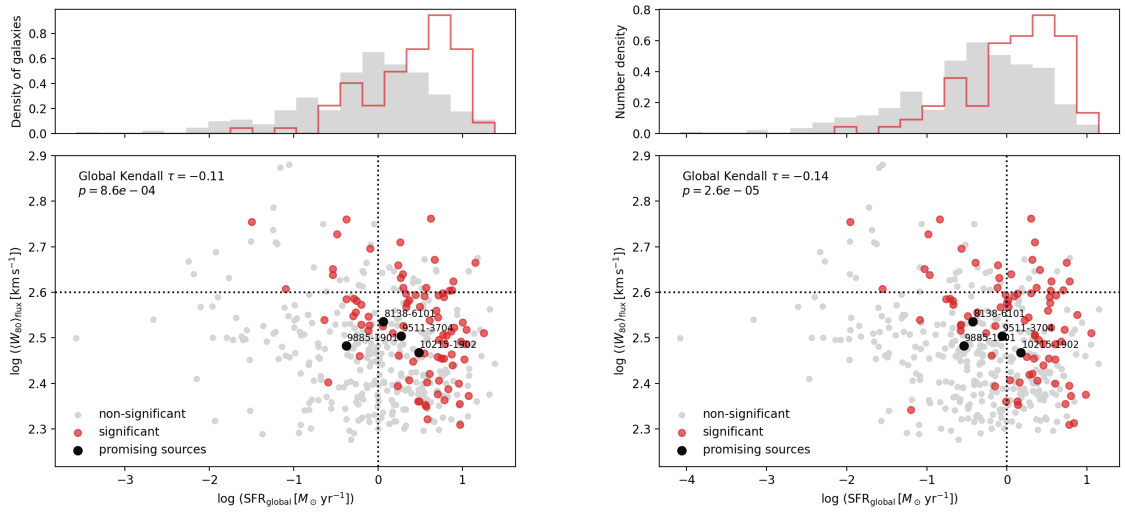

Figure 53. Global outflow properties of the flux averaged W_{80} values against the global SFR for the fossil outflow candidate sample. In the *left panel* the SFR over the last 30 Myr and in the *right panel* the SFR over the last 30 Myr is used.

C Additional promising fossil outflow candidates

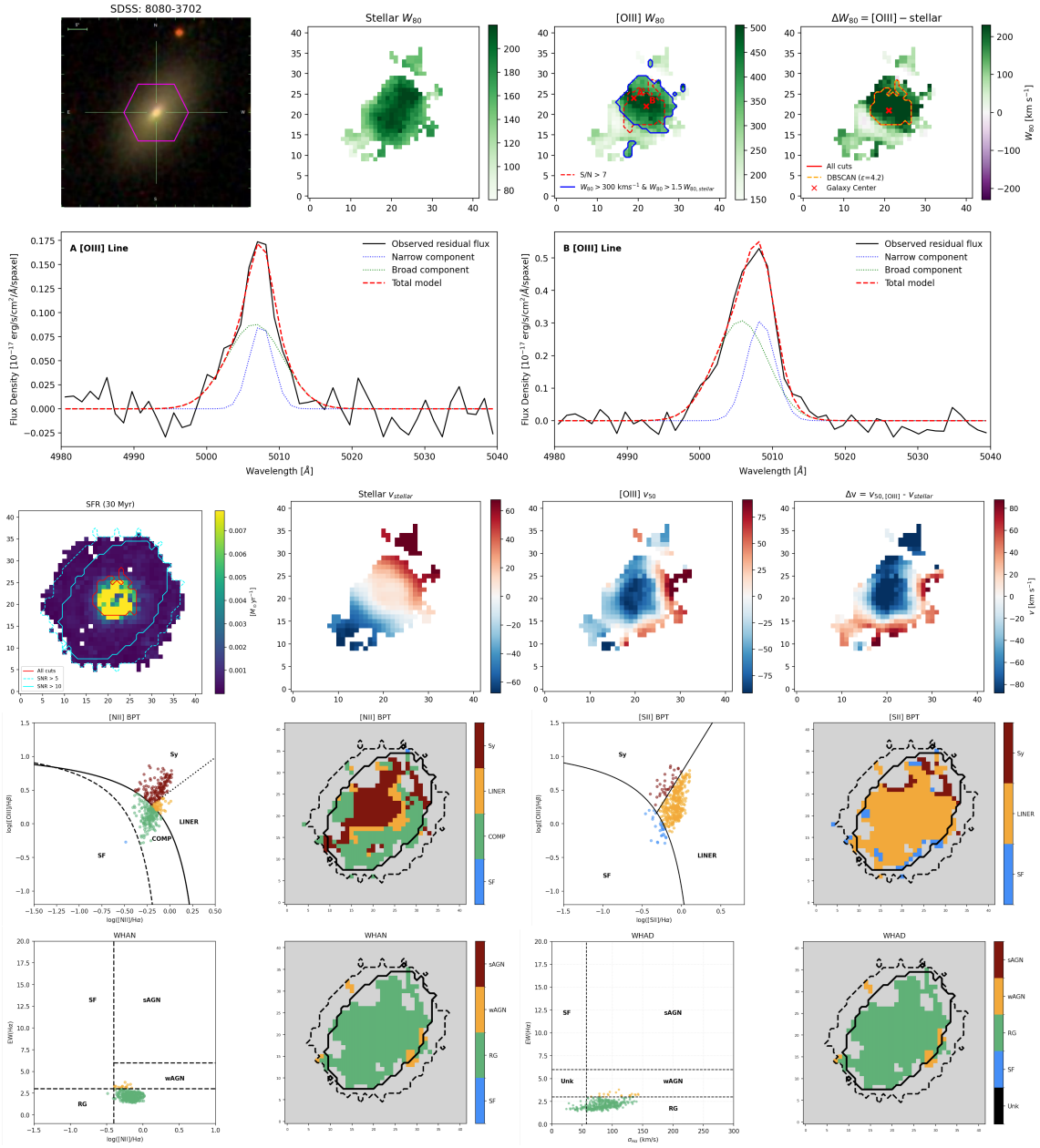

Figure 54. Maps and spectra of promising galaxy 8080-3702 (MaNGA ID: 1-38062). Same panels as in figure (40). This galaxy is a galaxy with low SFR and high mean W_{80} values selected from the upper left square in figure (47). The detected elevated gas kinematics are restrained to the galaxy center maybe also because the signal at larger distances is too low. The extracted spectral windows show clear [OIII] line broadening and in the [OIII] velocity map the central region is heavily blueshifted suggesting an outflow. Since this galaxy is not detected as an AGN by any selection method this could also be an fossil outflow candidate where the AGN shut off more recently. Even tho the WHAN and WHAD diagram show signatures of a retired galaxy, from the classical resolved BPT it is questionable, why this galaxy was not selected in the optical AGN catalog (Albán and Wylezalek 2023). So, further analysis is needed here, whether the golaxy does still host an active nucleus. 8080-3702 is classified as an elliptical galaxy from the Galaxy Zoo 1 project (Lintott et al. 2011) and is at a redshift of $z = 0.023$.

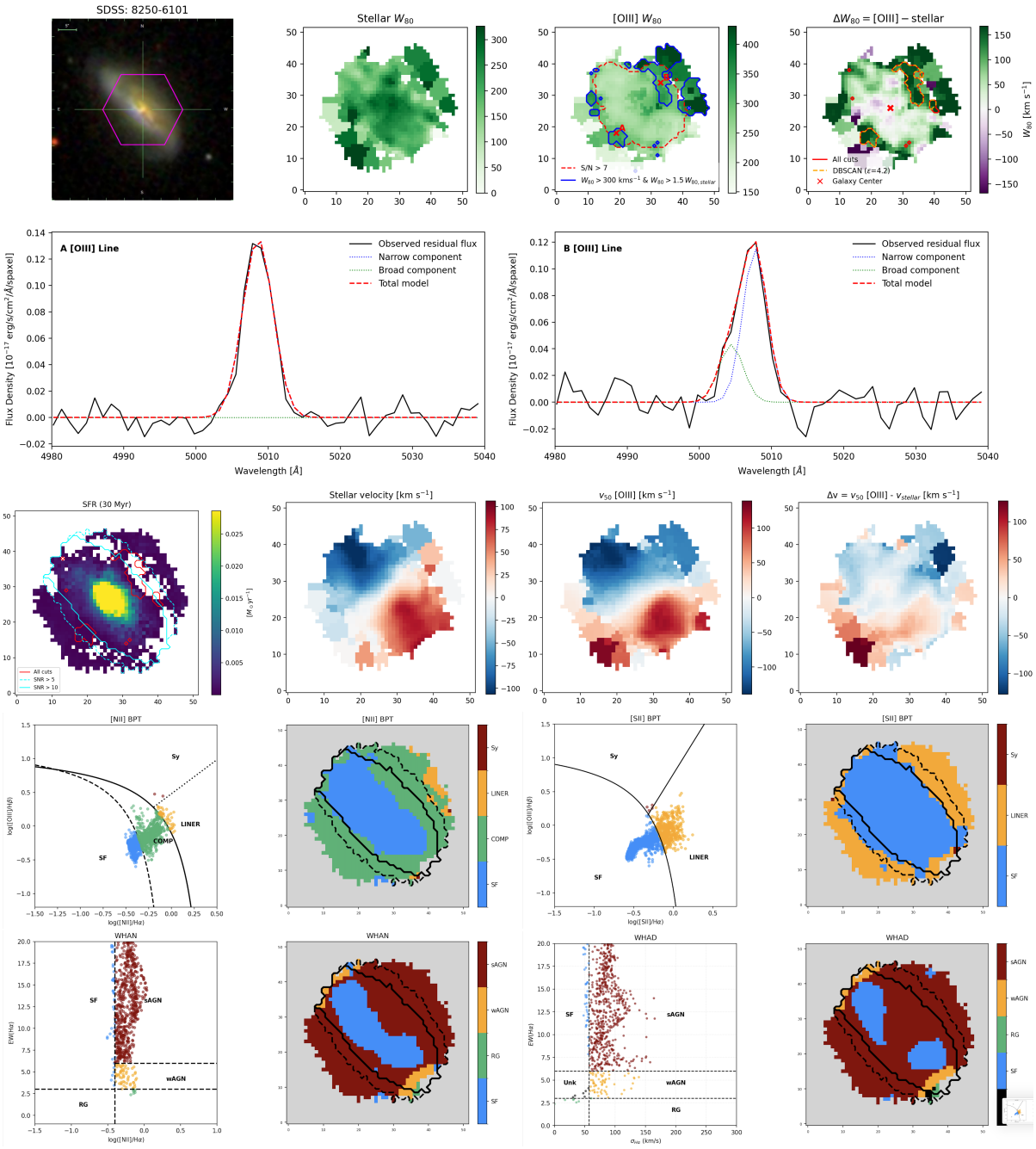

Figure 55. Maps and spectra of promising galaxy 8250-6101 (MaNGA ID: 1-217221). Same panels as in figure (40). Here a detached lobsided outflow along the north west minor galaxy axis is observed. In the spectrum B a more pronounced broad component of the [OIII] line profile, compared to the detected kinematically elevated region in the south east is shown. The asymmetry might also be caused by the observation angle because the other outflow cone should be located behind the galaxy disc. If the [OIII] W_{80} map and the ΔW_{80} map is inspected in more detail, an extension of higher line widths connecting the galaxy center and the detected outflow can be observed. If the absolute cut would be lower, the elevated region would still be attached to the nucleus. In the [OIII] LOS velocity map a curve of the rotational axis and a deviation from the straight rotation axis seen in the stellar velocity map can be seen, where the outflow is detected. The galaxy is classified as a spiral galaxy from the Galaxy Zoo 1 project (Lintott et al. 2011) and is at a redshift of $z = 0.028$.

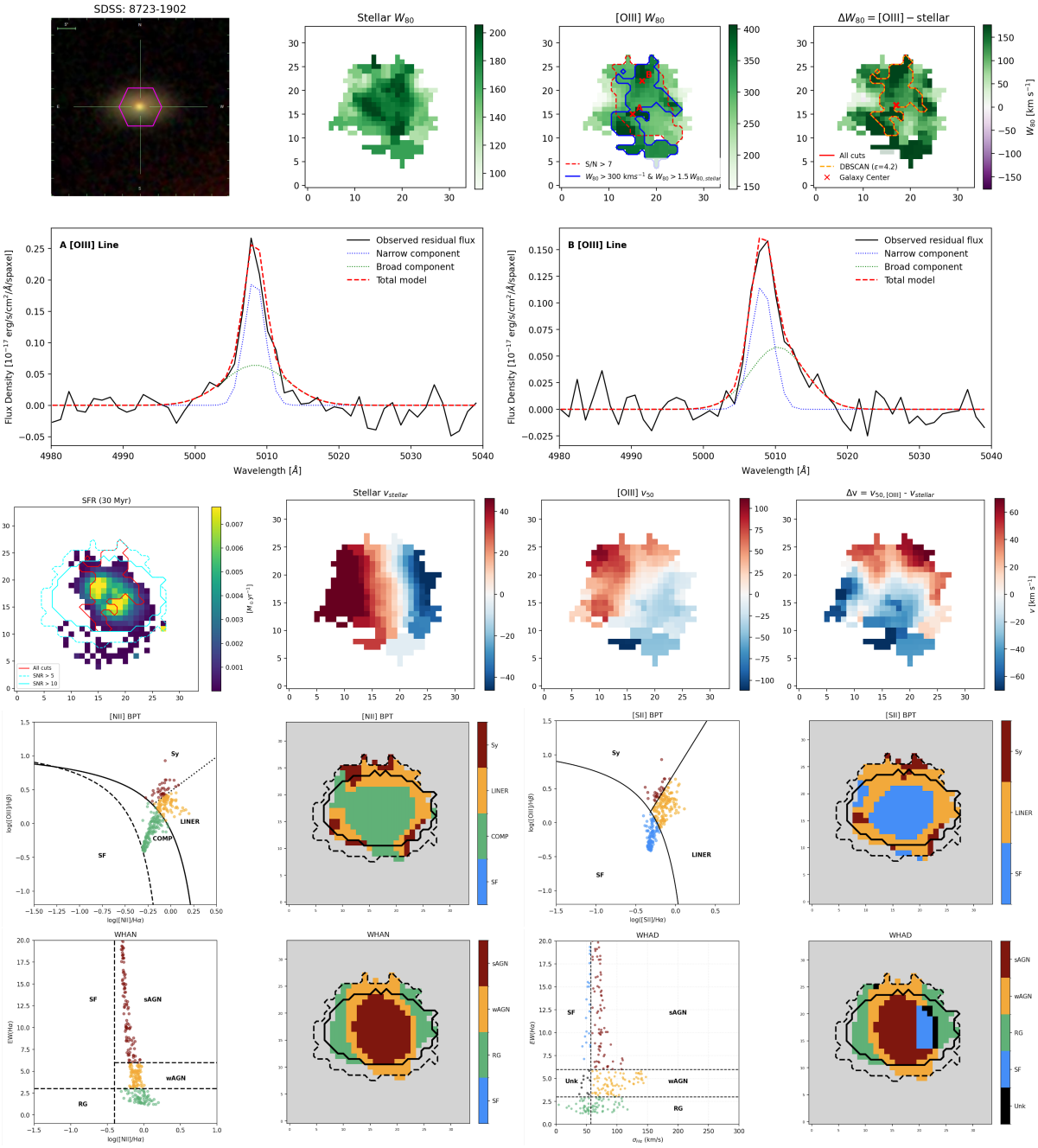

Figure 56. Maps and spectra of promising galaxy 8723-1902 (MaNGA ID: 1-352713). Same panels as in figure (40). Here kinematical gas elevation along the galaxy minor axis can be seen, but the region shows attachement to the galaxy core. The horizontal bar of high [OIII] W_{80} values right below the galaxy center is a result of the selection algorithm choosing the two Gaussian fit as the best fit. Taking this into account one could assume a rather detached outflow component in the north assuming the center elevation are a result of turbulence from a swept through outflow. The [OIII] line profile also shows a more pronounced secondary component to the north. The velocity maps show an distorted axis of the [OIII] LOS velocity compared to the stellar velocity. This is especially visible in the Δv map and indicates outflow to the north and south as well. The galaxy is classified as a elliptical galaxy from the Galaxy Zoo 1 project (Lintott et al. 2011) and is at a redshift of $z = 0.025$. This galaxy is in the AGN sample of Jaison et al. (in preparation) and shows clear AGN signatures in the [NII] BPT in the regions the elevated gas kinematics are detected. In the galaxy center the [SII] diagram detect a SF region whereas the WHAN and WHAD diagram classify the spaxel as sAGN.

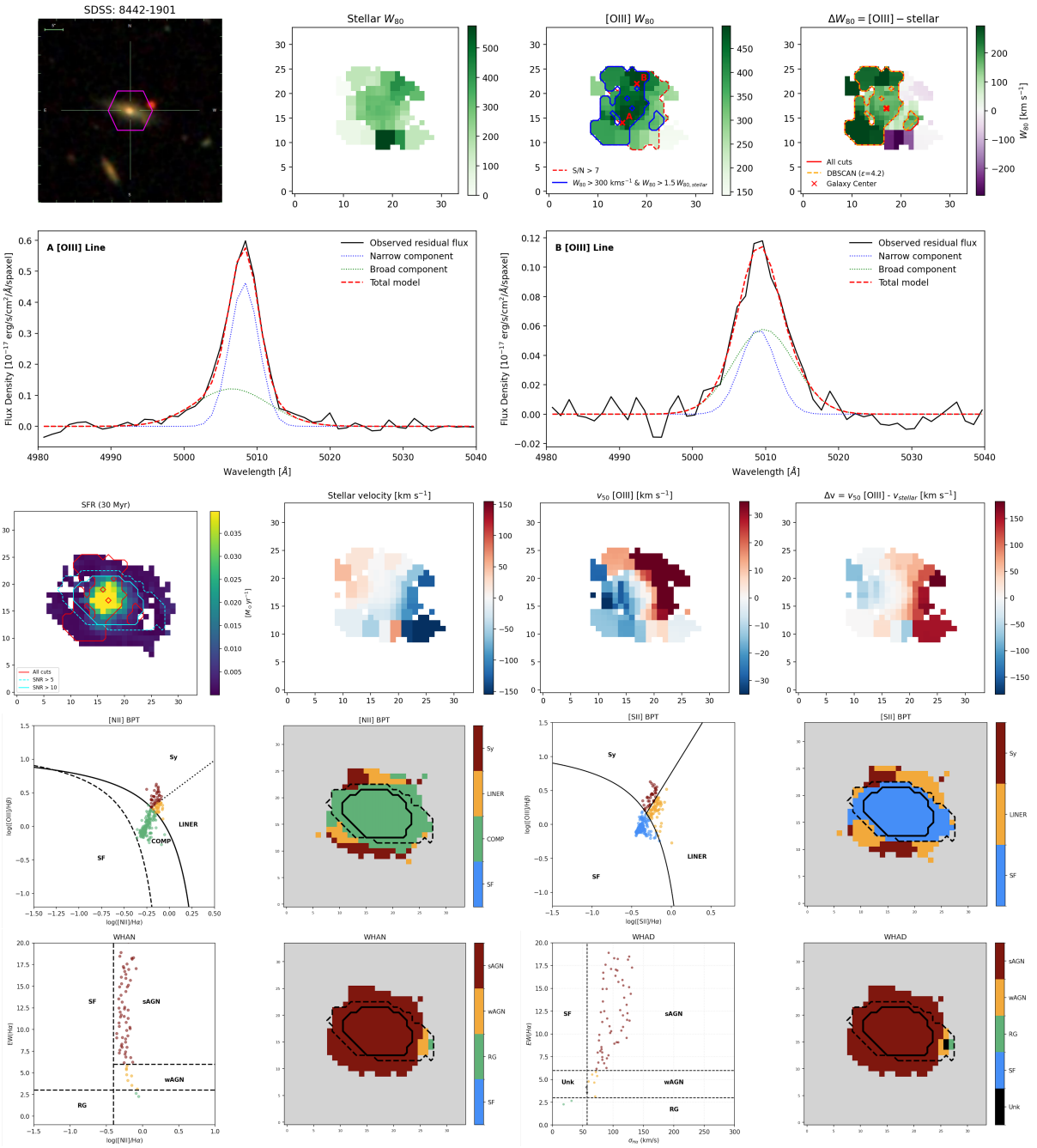

Figure 57. Maps and spectra of promising galaxy 8442-1901 (MaNGA ID: 1-415354). The same panels are shown as in figure (40). In the [OIII] map kinematic elevation for a large part of the galaxy can be seen. Looking at this elevated region in the residual ΔW_{80} map is gets more clear that the line widths are relatively higher towards larger distances from the galaxy core along the galaxy minor axis compared to the stellar dispersion. In the velocity maps large deviations between the stellar and the [OIII] LOS velocity are shown. This galaxy is also in the AGN sample of Jaison et al. (in preparation) and shows Seyfert and LINER signatures in the BPT diagrams towards the outskirts of the galaxy. In fact the [SII] diagram classifies most of the central region of the galaxy as SF. But in the WHAN and WHAD diagram almost the enire galaxy is classified as sAGN which coincides with the detections of elevated ionized gas kinematics also in the galaxy center. For this galaxy a positive significant spaxelwise correlation is found (figure (58)). 8442-1901 is at reshift $z = 0.036$.

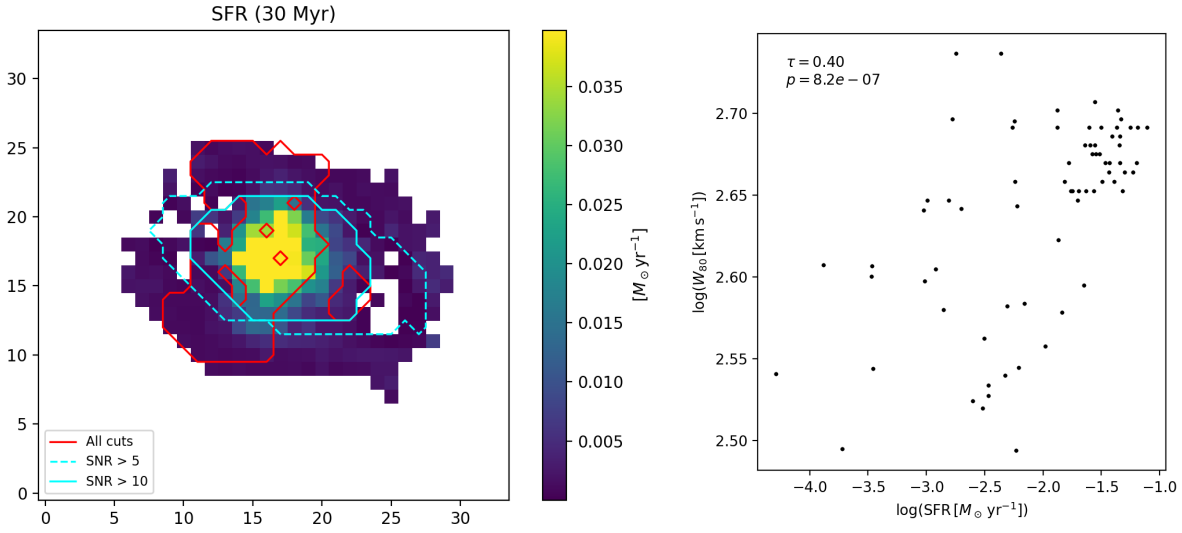

Figure 58. Correlation of v_{out} with SFR for galaxy 8442-1901. The panels are the same as the lower panel row in figure (45).

D Supplementary tables

Table 4. Category table of the fossil outflow candidate sample.

PlateIFU	kin. dist.	prom. 1st	prom. 2nd	str. centr.	improb.	failed	AGN
10214-1902	0	0	0	1	0	0	1
10215-1902	0	1	0	0	0	0	0
10215-6102	1	0	0	0	0	0	1
10218-6103	0	0	0	0	1	0	0
10219-12702	0	0	0	1	0	0	0
10221-3701	0	0	1	1	0	0	0
10223-1901	0	0	0	1	0	0	0
10223-3703	0	0	0	1	0	0	1
10223-6104	0	0	0	0	1	0	0
10225-3704	1	0	0	1	0	0	0
10226-12704	0	0	1	0	0	0	0
10492-12703	1	0	0	0	0	0	0
10496-12704	1	0	0	0	0	0	1
10500-12704	1	0	0	0	0	0	0
10503-9102	0	0	0	0	1	0	0
10506-1901	0	0	1	0	0	0	0
10508-6104	0	0	1	0	0	0	0
10510-12704	0	0	0	1	0	0	1
10512-6104	0	0	1	0	0	0	0
10515-6104	0	1	0	0	0	0	1
10516-6104	1	0	0	0	0	0	1
10516-9101	0	0	0	1	0	0	1
10520-1902	0	0	0	1	0	0	1
10520-3701	0	0	1	0	0	0	0
10841-12702	0	0	0	0	1	0	0
10843-9101	1	0	0	0	0	0	0
11004-12703	1	0	0	0	0	0	1
11004-3703	1	0	0	0	0	0	0
11010-1901	0	0	0	1	0	0	1
11010-3702	0	0	1	0	0	0	0
11010-6104	0	0	1	0	0	0	0
11013-3701	0	0	1	0	0	0	0
11018-12701	1	0	0	0	0	0	0
11024-12704	0	0	0	1	0	0	1

PlateIFU	kin. dist.	prom. 1st	prom. 2nd	str. centr.	improb.	failed	AGN
11025-9102	1	0	0	0	0	0	1
11742-12704	0	0	1	0	0	0	0
11743-6104	0	0	0	1	0	0	0
11745-6101	0	1	0	0	0	0	0
11747-1901	0	0	0	1	0	0	1
11753-12702	0	0	0	0	1	0	0
11753-6103	0	0	0	0	1	0	1
11754-6102	0	0	1	0	0	0	0
11755-1901	0	0	1	0	0	0	1
11758-1901	0	0	0	0	0	1	0
11759-12704	0	0	0	1	0	0	0
11761-3703	0	1	0	0	0	0	0
11823-9101	1	0	0	0	0	0	0
11824-12701	0	0	0	1	0	0	0
11828-3703	1	0	0	0	0	0	0
11831-3704	0	0	1	0	0	0	0
11831-6101	0	0	1	0	0	0	0
11834-1901	0	0	0	1	0	0	1
11836-12702	0	0	0	0	1	0	1
11838-3701	0	1	0	0	0	0	0
11865-9102	0	0	0	0	1	0	0
11939-12705	0	0	0	1	0	0	1
11939-3703	1	0	0	0	0	0	1
11939-6103	0	0	0	1	0	0	1
11941-12703	0	0	0	0	1	0	0
11942-12704	1	0	0	0	0	0	0
11942-3702	0	0	1	0	0	0	1
11946-3703	0	0	1	0	0	0	1
11950-6104	0	0	1	0	0	0	0
11954-12704	0	0	0	0	1	0	0
11954-1901	0	0	1	0	0	0	1
11955-3702	0	0	0	1	0	0	1
11955-9102	0	0	0	1	0	0	0
11956-6104	0	0	0	1	0	0	1
11957-1901	0	0	0	1	0	0	1
11957-6102	0	0	1	0	0	0	0
11962-6104	0	0	0	0	1	0	0

PlateIFU	kin. dist.	prom. 1st	prom. 2nd	str. centr.	improb.	failed	AGN
11969-6104	0	0	1	0	0	0	0
11976-3701	0	0	0	1	0	0	1
11977-12701	0	1	0	0	0	0	0
11979-3703	0	0	0	1	0	0	1
12068-12703	0	0	1	0	0	0	0
12068-12704	0	0	0	0	0	1	0
12069-12705	0	0	0	1	0	0	1
12074-12705	0	0	0	0	1	0	0
12074-6104	0	0	1	0	0	0	1
12075-12705	0	0	1	0	0	0	0
12078-3703	0	0	1	0	0	0	0
12078-6104	0	0	0	0	1	0	0
12078-9101	0	0	0	1	0	0	1
12080-12705	1	0	0	0	0	0	0
12080-6104	1	0	0	0	0	0	1
12084-12704	0	0	0	0	1	0	0
12085-6103	0	0	1	0	0	0	0
12087-6104	0	0	0	0	1	0	1
12089-12705	0	0	0	0	1	0	0
12089-3703	0	1	0	0	0	0	0
12090-9101	0	0	0	0	1	0	0
12092-6101	1	0	0	0	0	0	0
12094-1901	0	0	0	1	0	0	0
12094-3701	0	1	0	0	0	0	1
12483-6104	0	0	1	0	0	0	0
12488-1901	0	1	0	0	0	0	0
12488-6102	0	1	0	0	0	0	0
12490-3701	0	0	0	1	0	0	0
12514-9102	0	0	0	1	0	0	0
12620-3703	0	0	0	1	0	0	1
12620-6104	0	0	0	0	1	0	0
12621-9102	0	0	0	0	1	0	1
12624-12704	0	0	0	0	1	0	0
12673-3704	0	0	0	1	0	0	0
12673-6101	0	1	0	0	0	0	0
12673-9102	0	0	0	1	0	0	0
12684-12703	1	0	0	0	0	0	1

PlateIFU	kin. dist.	prom. 1st	prom. 2nd	str. centr.	improb.	failed	AGN
12700-6103	0	0	0	0	0	1	0
7443-12704	0	0	1	0	0	0	1
7443-3704	0	0	0	0	1	0	0
7443-9101	0	0	0	1	0	0	0
7815-1901	0	0	1	0	0	0	1
7958-6101	0	0	1	0	0	0	0
7960-3703	0	0	1	0	0	0	0
7961-6101	0	0	0	1	0	0	1
7963-12703	0	0	0	0	1	0	0
7965-1902	0	1	0	0	0	0	1
7965-6102	0	0	0	1	0	0	1
7972-12703	0	0	1	0	0	0	0
7977-12701	1	0	0	0	0	0	0
7977-12705	1	0	0	0	0	0	0
7993-1902	0	0	1	0	0	0	0
8075-6101	0	0	0	1	0	0	0
8078-6104	0	0	1	0	0	0	1
8079-1902	1	0	0	0	0	0	1
8079-6103	0	0	0	1	0	0	1
8080-12703	0	0	1	0	0	0	1
8080-3702	0	0	0	1	0	0	1
8080-3704	0	0	0	1	0	0	1
8081-12703	0	1	0	0	0	0	0
8081-9102	1	0	0	0	0	0	0
8082-12701	0	0	0	1	0	0	1
8082-1901	0	0	0	1	0	0	1
8082-3704	0	0	1	0	0	0	0
8082-6102	1	0	0	0	0	0	1
8082-9102	1	0	0	0	0	0	1
8084-12701	0	0	0	0	1	0	0
8084-1902	0	0	0	1	0	0	1
8085-12702	1	0	0	0	0	0	0
8085-3704	0	0	1	0	0	0	0
8086-9102	0	0	0	0	1	0	1
8087-12702	0	0	0	1	0	0	0
8088-3701	0	1	0	0	0	0	0
8089-6103	0	0	1	0	0	0	0

PlateIFU	kin. dist.	prom. 1st	prom. 2nd	str. centr.	improb.	failed	AGN
8091-12703	1	0	0	0	0	0	0
8093-6102	0	0	1	0	0	0	0
8093-6104	0	0	0	1	0	0	0
8095-1902	0	0	1	0	0	0	1
8095-3702	1	0	0	0	0	0	0
8132-12703	0	0	0	0	1	0	0
8132-12704	0	0	0	0	1	0	1
8132-6102	0	0	1	0	0	0	0
8135-12705	0	0	0	0	1	0	0
8135-1901	0	0	0	1	0	0	0
8138-3704	0	0	1	1	0	0	0
8138-6101	0	1	0	0	0	0	0
8143-1901	0	0	1	0	0	0	0
8145-1902	1	0	0	0	0	0	0
8145-9101	0	0	0	1	0	0	1
8146-1901	1	1	0	0	0	0	1
8148-6102	0	0	0	0	1	0	1
8149-3704	0	0	0	1	0	0	1
8149-6101	0	0	0	0	1	0	0
8150-1902	0	1	0	0	0	0	1
8152-1901	0	0	1	0	0	0	0
8154-12705	0	0	1	0	0	0	1
8155-3703	0	1	0	0	0	0	1
8241-12705	1	0	0	0	0	0	0
8243-3703	0	0	0	0	0	1	0
8244-3702	0	0	0	1	0	0	1
8245-3701	0	1	0	0	0	0	0
8247-1901	0	0	0	1	0	0	1
8249-6101	0	0	1	0	0	0	0
8250-3703	0	0	0	0	1	0	0
8250-6101	0	1	0	0	0	0	1
8252-12704	0	1	0	0	0	0	0
8252-12705	0	0	0	0	1	0	0
8252-3704	0	0	0	1	0	0	0
8252-9101	0	0	1	0	0	0	0
8255-12702	0	0	0	0	1	0	0
8257-12701	0	0	0	1	0	0	1

PlateIFU	kin. dist.	prom. 1st	prom. 2nd	str. centr.	improb.	failed	AGN
8259-1902	0	0	1	0	0	0	0
8260-6101	0	0	0	0	1	0	1
8262-9102	0	0	1	0	0	0	1
8263-3701	0	0	0	1	0	0	0
8312-12703	0	0	1	0	0	0	0
8312-12705	0	0	0	1	0	0	1
8312-1901	0	0	0	1	0	0	0
8315-12705	0	0	0	1	0	0	0
8318-3704	0	0	0	1	0	0	1
8319-12704	0	0	0	0	1	0	0
8321-6104	0	0	1	0	0	0	0
8323-6103	0	0	1	0	0	0	1
8328-1902	0	0	1	0	0	0	1
8329-1902	0	0	1	0	0	0	0
8329-6104	1	0	0	0	0	0	0
8330-12702	1	0	0	0	0	0	0
8330-3704	0	0	1	0	0	0	1
8330-6102	0	0	0	1	0	0	0
8334-12701	0	0	0	0	1	0	0
8335-12705	0	0	0	1	0	0	1
8335-3701	0	1	0	0	0	0	0
8337-6103	1	0	0	0	0	0	0
8341-12701	0	0	0	0	1	0	0
8438-12702	0	0	1	0	0	0	1
8438-1901	0	0	1	0	0	0	0
8438-9101	0	0	0	0	1	0	0
8439-12703	0	0	0	1	0	0	0
8440-12701	0	0	0	1	0	0	1
8440-12704	0	0	1	0	0	0	1
8442-1901	0	0	1	0	0	0	0
8445-12702	0	0	0	1	0	0	1
8445-12704	0	0	0	1	0	0	0
8445-6104	1	0	0	0	0	0	0
8448-12704	0	1	0	0	0	0	0
8450-6101	0	0	1	0	0	0	1
8452-12705	0	0	0	1	0	0	0
8453-12702	0	0	0	0	1	0	0

PlateIFU	kin. dist.	prom. 1st	prom. 2nd	str. centr.	improb.	failed	AGN
8453-1901	0	0	1	0	0	0	0
8453-3704	0	0	1	0	0	0	0
8454-6104	0	0	1	0	0	0	0
8455-12705	1	0	0	0	0	0	0
8458-3701	0	1	0	0	0	0	1
8462-1902	0	0	0	1	0	0	0
8464-3702	1	0	0	0	0	0	1
8464-3704	0	0	1	0	0	0	1
8465-3701	1	0	0	0	0	0	1
8465-9101	0	0	1	0	0	0	0
8466-1901	0	1	0	0	0	0	1
8481-6103	1	0	0	0	0	0	1
8483-12704	0	0	0	0	1	0	1
8488-12702	0	0	0	0	1	0	1
8488-12705	0	0	0	0	1	0	0
8546-6102	0	1	0	0	0	0	1
8548-6104	0	0	1	0	0	0	0
8549-3703	0	0	0	1	0	0	1
8550-12703	0	0	0	1	0	0	0
8550-3701	0	0	0	1	0	0	0
8551-12701	0	0	0	0	1	0	0
8551-6104	0	1	0	0	0	0	0
8554-3704	0	0	1	0	0	0	0
8555-1901	0	0	1	0	0	0	0
8564-9102	0	0	0	1	0	0	0
8568-3704	0	1	0	0	0	0	0
8569-6104	0	0	1	0	0	0	1
8570-3701	0	0	0	1	0	0	1
8588-12705	0	0	1	0	0	0	0
8588-6101	0	0	1	0	0	0	1
8592-3702	0	1	0	0	0	0	0
8597-12703	0	0	0	0	1	0	1
8597-12704	0	0	0	0	1	0	1
8601-12703	1	0	0	0	0	0	0
8601-6103	0	0	1	0	0	0	1
8609-12701	0	0	1	0	0	0	1
8610-12703	0	1	0	0	0	0	0

PlateIFU	kin. dist.	prom. 1st	prom. 2nd	str. centr.	improb.	failed	AGN
8611-9102	0	0	0	1	0	0	0
8612-12705	1	0	0	0	0	0	1
8612-6104	1	0	1	0	0	0	0
8615-3703	0	0	0	0	1	0	0
8616-12704	1	0	0	1	0	0	1
8616-3704	0	0	0	1	0	0	0
8616-9101	1	0	0	0	0	0	0
8618-12703	0	0	0	0	0	1	0
8622-12703	0	0	0	0	1	0	0
8626-12702	0	0	1	0	0	0	1
8652-6103	0	0	1	0	0	0	1
8652-6104	0	0	0	1	0	0	0
8656-6101	0	1	0	0	0	0	1
8657-1902	0	0	0	1	0	0	0
8657-6101	0	1	0	0	0	0	1
8657-9101	0	0	0	0	1	0	1
8710-12703	1	0	0	0	0	0	1
8712-1902	0	1	0	0	0	0	0
8719-12702	1	0	0	0	0	0	1
8723-12704	0	0	0	1	0	0	1
8723-1902	0	1	0	0	0	0	0
8723-3702	0	0	0	1	0	0	0
8725-3701	0	0	0	0	1	0	0
8726-12701	0	0	0	1	0	0	0
8727-12705	0	0	0	1	0	0	1
8931-12702	0	0	0	1	0	0	0
8931-9101	0	0	0	1	0	0	1
8935-6104	1	0	0	0	0	0	0
8937-1902	1	0	0	0	0	0	0
8940-3701	0	0	0	1	0	0	0
8940-6104	1	0	0	0	0	0	1
8942-6104	0	0	1	0	0	0	1
8942-9101	0	0	0	0	1	0	0
8944-3704	0	0	1	0	0	0	0
8945-3702	0	1	0	0	0	0	0
8950-12705	0	0	1	0	0	0	1
8950-1901	0	1	0	0	0	0	1

PlateIFU	kin. dist.	prom. 1st	prom. 2nd	str. centr.	improb.	failed	AGN
8952-3703	0	1	0	0	0	0	0
8952-6103	0	0	1	0	0	0	0
8978-12702	1	0	0	0	0	0	0
8982-9101	1	0	0	0	0	0	0
8984-12704	0	0	0	1	0	0	0
8984-12705	0	0	0	0	1	0	1
8985-6104	0	1	0	0	0	0	1
8987-9102	0	0	1	0	0	0	0
8989-1902	0	0	0	1	0	0	0
8991-12705	0	0	0	0	1	0	0
8992-3701	0	0	0	1	0	0	1
8992-6101	0	0	1	0	0	0	0
8994-9102	0	0	1	0	0	0	1
8996-3704	0	0	0	1	0	0	1
8998-3702	0	0	1	0	0	0	0
8999-12704	0	0	0	0	1	0	0
8999-9101	0	0	1	0	0	0	1
9001-6104	0	0	0	1	0	0	0
9025-1902	0	0	0	1	0	0	0
9025-3702	0	0	0	1	0	0	0
9027-1902	0	1	0	0	0	0	1
9027-3701	0	1	0	0	0	0	0
9029-12705	0	0	0	0	1	0	1
9029-1902	0	0	1	0	0	0	0
9031-12703	0	0	0	0	1	0	1
9031-3702	0	0	1	0	0	0	0
9032-3704	0	0	0	1	0	0	0
9032-6104	0	1	0	0	0	0	1
9034-1902	0	0	0	1	0	0	0
9034-6101	0	0	0	1	0	0	0
9037-1902	0	0	1	0	0	0	1
9041-12702	0	0	0	0	1	0	0
9041-1902	0	0	0	1	0	0	0
9041-6102	0	0	0	0	1	0	0
9041-9102	0	0	0	1	0	0	0
9046-12703	1	0	0	0	0	0	0
9047-3701	0	0	1	0	0	0	0

PlateIFU	kin. dist.	prom. 1st	prom. 2nd	str. centr.	improb.	failed	AGN
9049-12701	1	0	0	0	0	0	1
9049-3701	0	0	1	0	0	0	0
9086-12702	0	0	0	0	1	0	0
9087-12704	0	0	1	0	0	0	0
9088-3702	0	0	0	1	0	1	0
9089-12701	0	0	0	1	0	0	0
9093-12705	0	0	0	1	0	0	1
9093-3704	0	0	1	0	0	0	0
9094-3701	0	0	1	0	0	0	0
9181-1902	0	0	1	0	0	0	0
9183-12705	0	0	1	0	0	0	0
9185-9101	1	0	0	0	0	0	1
9186-3701	0	0	1	0	0	0	0
9188-1901	0	0	1	0	0	0	0
9188-6104	0	0	1	0	0	0	1
9190-1901	0	0	1	0	0	0	1
9193-6101	0	0	0	1	0	0	1
9194-12701	1	0	0	0	0	0	1
9194-12703	0	0	0	0	1	0	1
9194-6104	0	0	1	0	0	0	0
9195-12701	0	0	0	0	1	0	1
9195-12704	0	0	0	0	1	0	1
9196-1902	0	0	1	0	0	0	0
9485-6104	0	0	1	0	0	0	1
9488-12704	0	0	0	0	1	0	1
9488-1901	0	0	0	1	0	0	1
9492-12701	0	0	0	1	0	0	0
9493-1902	0	0	1	0	0	0	1
9493-6103	0	0	0	0	1	0	1
9493-9102	0	0	0	1	0	0	0
9494-3701	0	1	0	0	0	0	1
9494-9102	0	0	0	1	0	0	1
9499-6102	0	0	1	0	0	0	0
9503-3702	0	0	1	0	0	0	0
9509-6104	0	0	1	0	0	0	1
9511-3704	0	1	0	0	0	0	0
9511-6101	1	0	0	0	0	0	0

PlateIFU	kin. dist.	prom. 1st	prom. 2nd	str. centr.	improb.	failed	AGN
9511-6102	0	0	0	1	0	0	1
9511-6103	0	0	0	1	0	0	1
9513-3702	0	0	1	0	0	0	1
9514-12703	0	0	0	1	0	0	0
9514-12704	0	0	0	1	0	0	0
9862-12703	0	0	1	0	0	0	1
9865-6104	0	0	0	0	0	1	0
9866-12703	0	0	1	0	0	0	0
9869-6101	0	0	0	1	0	0	0
9872-3701	0	1	0	0	0	0	1
9872-6104	0	0	0	0	1	0	1
9872-9101	0	0	0	0	1	0	1
9878-12701	0	0	0	1	0	0	0
9878-3703	0	1	0	0	0	0	0
9879-12704	1	0	0	1	0	0	0
9881-9102	1	0	0	0	0	0	0
9882-6102	0	0	0	0	1	0	0
9883-3703	0	0	0	1	0	0	1
9885-1901	0	1	0	0	0	0	0
9888-12704	0	0	0	0	1	0	0
9889-12705	0	0	1	0	0	0	1
9891-1901	0	1	0	0	0	0	0
9894-3701	0	1	0	0	0	0	1

Notes. Same columns and boolean arrays as in table (1).

Table 5. Ionized-gas outflow properties for full fossil outflow candidate sample.

PlateIFU	$L_{\rm OIII,wing}$ (10^{39} erg s^{-1})	n_e (cm^{-3})	$M_{\rm gas}$ ($10^3\,M_\odot$)	$R_{\rm out}$ (kpc)	$v_{\rm out}$ (km s^{-1})	$\dot{M}$ ($10^{-5}\,M_\odot$ yr^{-1})	$\dot{E}$ (10^{36} erg s^{-1})
10214-1902	0.60	1796	1.72	0.77	369	84.10	36.05
10215-1902	1.25	295	0.59	3.25	375	6.97	3.08
10215-6102	0.76	206	0.25	1.88	391	5.35	2.57
10218-6103	0.26	87	0.04	5.65	318	0.21	0.07
10219-12702	0.60	264	0.25	2.35	382	4.20	1.93
10221-3701	0.95	1581	2.39	0.99	350	86.72	33.42
10223-1901	0.58	1506	1.41	0.61	362	86.01	35.60
10223-3703	0.54	429	0.37	0.83	423	19.42	10.93
10223-6104	0.19	606	0.18	3.85	340	1.62	0.59
10225-3704	0.79	87	0.11	2.61	369	1.58	0.68
10226-12704	2.86	613	2.80	1.63	393	68.98	33.50
10492-12703	3.93	1386	8.71	3.27	433	117.87	69.49
10496-12704	15.95	703	17.95	1.78	385	395.76	184.51
10500-12704	7.82	272	3.41	6.05	395	22.76	11.18
10503-9102	0.04	250	0.02	6.20	340	0.09	0.03
10506-1901	0.51	1213	0.98	1.33	332	24.95	8.64
10508-6104	20.22	529	17.10	2.56	487	332.84	248.34
10510-12704	2.68	73	0.31	0.11	381	108.88	49.87
10512-6104	0.52	346	0.29	2.49	358	4.26	1.72
10515-6104	0.61	2984	2.90	1.54	357	68.75	27.60
10516-6104	2.94	428	2.01	1.14	379	68.60	31.08
10516-9101	0.34	2829	1.53	0.84	378	69.96	31.51
10520-1902	0.99	1637	2.60	0.69	542	208.47	193.01
10520-3701	0.20	689	0.22	1.91	351	4.09	1.58
10841-12702	0.05	748	0.06	4.04	344	0.55	0.21
10843-9101	35.61	478	27.25	5.59	393	196.11	95.55
11004-12703	2.07	1267	4.20	1.69	444	112.89	70.07
11004-3703	2.25	111	0.40	1.53	338	9.04	3.26
11010-1901	0.81	1353	1.76	0.94	407	78.03	40.66
11010-3702	0.24	135	0.05	0.45	340	3.96	1.44
11010-6104	4.28	179	1.23	1.09	431	49.54	28.93
11013-3701	0.15	54	0.01	1.51	327	0.29	0.10
11018-12701	2.17	2079	7.23	3.76	385	75.77	35.44
11024-12704	0.14	2446	0.56	0.58	338	33.70	12.16
11025-9102	2.38	162	0.62	4.49	368	5.17	2.20
11742-12704	1.13	588	1.06	1.55	366	25.71	10.84
11743-6104	0.76	124	0.15	1.24	377	4.71	2.11
11745-6101	3.45	233	1.29	1.77	356	26.44	10.56
11747-1901	0.18	1613	0.47	0.94	384	19.71	9.14
11753-12702	0.06	577	0.06	3.87	422	0.63	0.35
11753-6103	0.16	593	0.15	3.60	489	2.10	1.58
11754-6102	1.48	745	1.76	0.79	413	94.36	50.61

PlateIFU	$L_{\rm OIII,wing}$ ($10^{39}\,{\rm erg\,s^{-1}}$)	n_e ($\rm cm^{-3}$)	$M_{\rm gas}$ ($10^3\,M_\odot$)	$R_{\rm out}$ (kpc)	$v_{\rm out}$ ($\rm km\,s^{-1}$)	$\dot{M}$ ($10^{-5}\,M_\odot\,\rm yr^{-1}$)	$\dot{E}$ ($10^{36}\,\rm erg\,s^{-1}$)
11755-1901	1.36	205	0.45	0.92	410	20.36	10.76
11758-1901	2.16	1298	4.48	0.63	458	335.65	221.98
11759-12704	10.55	502	8.48	3.57	400	97.24	49.08
11761-3703	1.80	116	0.33	0.84	346	14.06	5.30
11823-9101	13.68	361	7.90	5.81	361	50.20	20.62
11824-12701	1.59	191	0.48	1.92	351	9.05	3.52
11828-3703	1.02	104	0.17	1.94	475	4.22	3.01
11831-3704	0.33	1522	0.80	0.79	345	35.30	13.22
11831-6101	1.13	168	0.30	1.44	351	7.57	2.94
11834-1901	0.56	861	0.77	0.92	340	29.33	10.66
11836-12702	0.11	715	0.13	3.03	364	1.57	0.66
11838-3701	7.19	539	6.19	1.80	472	165.72	116.16
11865-9102	0.42	239	0.16	8.55	338	0.65	0.23
11939-12705	0.56	1869	1.67	0.74	405	93.08	48.20
11939-3703	3.49	422	2.35	0.68	490	172.99	130.79
11939-6103	1.00	2365	3.80	0.48	386	315.62	148.43
11941-12703	0.15	1936	0.48	6.63	544	4.00	3.73
11942-12704	3.60	280	1.62	5.93	348	9.69	3.69
11942-3702	2.01	561	1.80	0.91	414	84.16	45.52
11946-3703	9.52	409	6.23	0.89	391	279.91	134.95
11950-6104	13.06	516	10.78	1.11	352	348.86	135.91
11954-12704	5.65	253	2.29	3.35	370	25.87	11.17
11954-1901	1.51	307	0.74	0.73	405	42.05	21.68
11955-3702	2.72	1235	5.38	1.20	477	219.39	157.36
11955-9102	3.89	350	2.18	0.91	453	111.06	71.90
11956-6104	0.26	1538	0.63	1.34	346	16.78	6.33
11957-1901	1.19	951	1.81	0.89	336	69.81	24.81
11957-6102	1.22	365	0.71	3.40	345	7.38	2.77
11962-6104	0.12	894	0.17	5.92	319	0.94	0.30
11969-6104	0.96	563	0.86	1.45	335	20.35	7.18
11976-3701	12.34	217	4.28	1.72	433	110.28	65.11
11977-12701	0.94	448	0.68	2.42	389	11.10	5.30
11979-3703	2.83	1796	8.12	1.31	551	349.68	335.00
12068-12703	2.09	540	1.80	2.36	339	26.50	9.61
12068-12704	0.86	1436	1.98	6.32	519	16.67	14.16
12069-12705	3.21	776	3.99	1.78	364	83.25	34.81
12074-12705	0.03	837	0.04	2.64	325	0.54	0.18
12074-6104	0.31	1275	0.63	0.91	391	27.95	13.47
12075-12705	0.23	1871	0.70	0.69	350	36.23	13.96
12078-3703	0.60	230	0.22	2.22	351	3.54	1.37
12078-6104	0.05	641	0.05	4.08	319	0.43	0.14
12078-9101	5.00	273	2.18	5.49	367	14.96	6.36
12080-12705	12.90	1573	32.47	3.25	458	468.78	309.91
12080-6104	0.39	735	0.45	1.46	341	10.83	3.98

PlateIFU	$L_{\rm OIII,wing}$ ($10^{39}\,{\rm erg\,s^{-1}}$)	n_e ($\rm cm^{-3}$)	$M_{\rm gas}$ ($10^3\,M_\odot$)	$R_{\rm out}$ (kpc)	$v_{\rm out}$ ($\rm km\,s^{-1}$)	$\dot{M}$ ($10^{-5}\,M_\odot\,\rm yr^{-1}$)	$\dot{E}$ ($10^{36}\,\rm erg\,s^{-1}$)
12084-12704	0.03	256	0.01	5.23	412	0.11	0.06
12085-6103	2.92	390	1.82	1.10	386	65.37	30.64
12087-6104	8.53	838	11.43	1.44	407	329.69	172.10
12089-12705	1.28	401	0.82	4.43	358	6.79	2.74
12089-3703	0.61	559	0.55	2.42	328	7.61	2.57
12090-9101	0.22	174	0.06	4.64	322	0.43	0.14
12092-6101	1.89	51	0.15	2.78	349	1.97	0.76
12094-1901	1.22	656	1.28	1.40	394	36.98	18.08
12094-3701	17.20	201	5.53	1.99	451	127.96	81.85
12483-6104	0.13	565	0.12	1.71	353	2.50	0.99
12488-1901	0.99	260	0.41	2.45	342	5.88	2.16
12488-6102	1.58	330	0.83	1.98	360	15.47	6.33
12490-3701	2.55	199	0.81	1.14	414	30.13	16.25
12514-9102	2.48	224	0.89	1.51	405	24.40	12.62
12620-3703	1.16	80	0.15	0.52	405	11.86	6.11
12620-6104	0.30	97	0.05	6.37	328	0.24	0.08
12621-9102	1.38	1256	2.77	2.67	455	48.37	31.60
12624-12704	0.15	399	0.10	5.77	563	0.97	0.97
12673-3704	0.70	1172	1.32	1.13	395	47.09	23.20
12673-6101	1.54	559	1.38	1.34	359	37.59	15.24
12673-9102	1.16	915	1.70	1.01	336	57.75	20.53
12684-12703	48.82	602	47.03	9.42	466	237.89	162.66
12700-6103	2.53	268	1.08	3.49	341	10.84	3.96
7443-12704	0.36	735	0.43	4.54	2022	19.54	251.75
7443-3704	0.15	459	0.11	2.62	340	1.42	0.52
7443-9101	1.14	138	0.25	0.71	329	11.95	4.09
7815-1901	0.08	1220	0.15	1.04	355	5.37	2.14
7958-6101	1.10	161	0.28	0.94	374	11.51	5.08
7960-3703	0.38	1138	0.69	3.30	354	7.59	2.99
7961-6101	2.79	1980	8.86	1.33	435	295.26	175.99
7963-12703	0.95	658	1.00	4.64	673	14.91	21.30
7965-1902	1.93	198	0.61	1.42	418	18.42	10.12
7965-6102	0.33	63	0.03	0.96	347	1.25	0.47
7972-12703	0.86	932	1.28	4.38	358	10.68	4.31
7977-12701	101.92	484	78.98	5.57	519	752.54	638.72
7977-12705	5.17	269	2.23	2.18	384	40.15	18.67
7993-1902	4.22	48	0.33	0.93	422	15.15	8.52
8075-6101	0.85	858	1.17	1.42	345	29.03	10.91
8078-6104	11.01	675	11.89	1.56	410	319.07	168.92
8079-1902	1.50	55	0.13	1.64	379	3.12	1.41
8079-6103	0.83	1242	1.65	1.40	396	47.53	23.50
8080-12703	4.43	125	0.89	2.19	418	17.30	9.50
8080-3702	1.51	983	2.38	0.74	455	150.05	97.72
8080-3704	3.17	444	2.25	0.57	371	148.92	64.62

PlateIFU	$L_{\rm OIII,wing}$ ($10^{39}\,{\rm erg\,s^{-1}}$)	n_e ($\rm cm^{-3}$)	$M_{\rm gas}$ ($10^3\,M_\odot$)	$R_{\rm out}$ (kpc)	$v_{\rm out}$ ($\rm km\,s^{-1}$)	$\dot{M}$ ($10^{-5}\,M_\odot\,\rm yr^{-1}$)	$\dot{E}$ ($10^{36}\,\rm erg\,s^{-1}$)
8081-12703	0.28	607	0.27	2.07	376	4.98	2.22
8081-9102	1.35	591	1.28	3.30	394	15.56	7.61
8082-12701	1.04	200	0.33	1.05	419	13.67	7.57
8082-1901	0.61	1167	1.14	0.93	388	48.39	23.00
8082-3704	0.53	2514	2.11	1.38	347	54.27	20.61
8082-6102	4.53	1482	10.75	1.44	608	463.97	540.45
8082-9102	4.11	205	1.35	2.36	457	26.80	17.62
8084-12701	0.28	210	0.09	6.09	345	0.54	0.20
8084-1902	0.20	877	0.29	0.62	355	16.83	6.67
8085-12702	0.20	524	0.17	4.48	391	1.47	0.71
8085-3704	2.63	1343	5.65	1.71	349	118.02	45.18
8086-9102	1.85	575	1.70	2.01	385	33.25	15.51
8087-12702	19.04	654	19.93	2.03	545	547.79	513.48
8088-3701	2.73	300	1.31	1.17	485	55.52	41.17
8089-6103	43.95	391	27.47	1.95	469	674.11	467.13
8091-12703	21.95	1494	52.47	11.04	455	220.95	143.89
8093-6102	2.61	690	2.89	1.86	349	55.41	21.23
8093-6104	3.28	631	3.31	3.50	354	34.24	13.55
8095-1902	16.77	72	1.94	1.66	394	47.16	23.04
8095-3702	0.49	3122	2.45	1.25	357	71.42	28.68
8132-12703	8.73	282	3.94	11.73	425	14.63	8.35
8132-12704	2.82	776	3.50	6.43	429	23.85	13.80
8132-6102	0.17	706	0.19	1.24	335	5.26	1.86
8135-12705	0.04	512	0.04	2.90	332	0.43	0.15
8135-1901	0.23	1291	0.48	0.77	338	21.82	7.86
8138-3704	0.19	722	0.22	0.66	358	11.92	4.82
8138-6101	8.43	822	11.09	1.23	367	338.84	143.71
8143-1901	1.65	1583	4.17	1.01	353	149.01	58.64
8145-1902	23.80	146	5.57	1.03	429	237.21	137.31
8145-9101	0.40	417	0.26	0.77	340	11.92	4.33
8146-1901	2.30	320	1.18	1.29	366	34.31	14.44
8148-6102	0.12	699	0.14	3.24	347	1.48	0.56
8149-3704	0.22	53	0.02	0.34	330	1.83	0.63
8149-6101	0.32	681	0.34	6.30	411	2.30	1.22
8150-1902	0.10	183	0.03	1.20	344	0.88	0.33
8152-1901	0.71	173	0.20	1.30	359	5.58	2.26
8154-12705	2.27	698	2.54	1.02	354	89.88	35.42
8155-3703	0.40	779	0.50	2.33	380	8.43	3.83
8241-12705	0.46	955	0.71	1.16	365	22.78	9.55
8243-3703	0.60	931	0.89	5.87	1860	28.87	314.73
8244-3702	4.63	174	1.29	0.80	403	66.79	34.22
8245-3701	0.56	589	0.53	2.50	335	7.31	2.59
8247-1901	1.51	454	1.10	0.83	706	95.19	149.49
8249-6101	0.78	619	0.77	1.32	344	20.60	7.69

PlateIFU	$L_{\rm OIII,wing}$ ($10^{39}\,{\rm erg\,s^{-1}}$)	n_e ($\rm cm^{-3}$)	$M_{\rm gas}$ ($10^3\,M_\odot$)	$R_{\rm out}$ (kpc)	$v_{\rm out}$ ($\rm km\,s^{-1}$)	$\dot{M}$ ($10^{-5}\,M_\odot\,\rm yr^{-1}$)	$\dot{E}$ ($10^{36}\,\rm erg\,s^{-1}$)
8250-3703	0.00	293	0.00	nan	nan	nan	nan
8250-6101	1.85	200	0.59	2.31	348	9.13	3.49
8252-12704	0.30	891	0.43	2.14	523	10.74	9.27
8252-12705	0.11	193	0.03	4.76	365	0.26	0.11
8252-3704	4.03	2439	15.73	1.45	415	461.31	250.07
8252-9101	1.86	1380	4.11	1.54	360	98.32	40.11
8255-12702	0.10	282	0.04	4.05	348	0.38	0.15
8257-12701	11.63	236	4.39	0.78	401	229.91	116.28
8259-1902	0.22	159	0.06	0.78	362	2.69	1.11
8260-6101	0.19	145	0.04	3.38	332	0.45	0.16
8262-9102	9.39	200	3.01	1.35	557	126.54	123.83
8263-3701	0.85	423	0.57	0.90	415	27.17	14.73
8312-12703	2.07	747	2.47	1.75	350	50.71	19.62
8312-12705	0.48	1417	1.08	1.05	394	41.47	20.29
8312-1901	0.40	1850	1.20	1.02	371	44.41	19.25
8315-12705	7.77	513	6.38	1.95	416	139.02	75.94
8318-3704	12.01	1268	24.38	0.71	574	2001.48	2076.64
8319-12704	0.58	167	0.15	3.95	360	1.44	0.59
8321-6104	0.95	837	1.27	1.75	356	26.52	10.61
8323-6103	2.46	657	2.58	1.40	403	75.98	38.87
8328-1902	3.22	702	3.62	1.05	457	160.88	106.06
8329-1902	0.34	297	0.16	0.82	368	7.43	3.16
8329-6104	0.94	87	0.13	0.77	393	6.92	3.37
8330-12702	6.04	323	3.12	13.24	448	10.78	6.80
8330-3704	0.71	962	1.10	0.84	349	46.80	17.99
8330-6102	0.40	228	0.14	1.40	327	3.45	1.17
8334-12701	0.38	685	0.41	4.82	348	3.05	1.16
8335-12705	0.75	175	0.21	1.07	362	7.24	2.99
8335-3701	0.08	135	0.02	1.41	358	0.45	0.18
8337-6103	7.80	1381	17.24	4.31	413	169.14	91.09
8341-12701	0.13	501	0.11	6.04	800	1.46	2.94
8438-12702	0.44	99	0.07	2.22	356	1.14	0.46
8438-1901	1.75	1280	3.58	0.90	414	169.22	91.46
8438-9101	0.32	309	0.16	4.57	367	1.30	0.55
8439-12703	0.29	234	0.11	2.48	353	1.58	0.62
8440-12701	5.45	543	4.73	1.18	726	297.57	493.87
8440-12704	1.10	1221	2.15	3.12	420	29.61	16.43
8442-1901	7.84	677	8.49	1.23	442	311.77	191.47
8445-12702	6.89	1243	13.71	1.52	548	506.16	478.06
8445-12704	0.37	900	0.54	0.96	384	22.07	10.28
8445-6104	0.05	1107	0.09	1.52	348	2.12	0.81
8448-12704	0.21	921	0.30	1.75	941	16.58	46.24
8450-6101	2.05	299	0.98	0.95	442	46.72	28.73
8452-12705	0.24	234	0.09	2.29	352	1.42	0.55

PlateIFU	$L_{\rm OIII,wing}$ ($10^{39}\,{\rm erg\,s^{-1}}$)	n_e ($\rm cm^{-3}$)	$M_{\rm gas}$ ($10^3\,M_\odot$)	$R_{\rm out}$ (kpc)	$v_{\rm out}$ ($\rm km\,s^{-1}$)	$\dot{M}$ ($10^{-5}\,M_\odot\,\rm yr^{-1}$)	$\dot{E}$ ($10^{36}\,\rm erg\,s^{-1}$)
8453-12702	0.19	382	0.12	4.40	325	0.89	0.30
8453-1901	1.32	255	0.54	0.95	356	20.62	8.23
8453-3704	1.85	380	1.12	1.54	360	26.86	10.94
8454-6104	3.61	118	0.68	3.61	357	6.90	2.76
8455-12705	0.27	203	0.09	5.38	344	0.58	0.22
8458-3701	0.09	431	0.06	1.62	405	1.65	0.85
8462-1902	0.54	206	0.18	1.04	433	7.65	4.52
8464-3702	3.60	294	1.70	1.14	541	82.68	76.30
8464-3704	1.82	114	0.33	1.02	335	11.18	3.95
8465-3701	4.14	100	0.66	1.70	336	13.40	4.78
8465-9101	0.34	403	0.22	1.49	350	5.28	2.04
8466-1901	0.36	1673	0.95	1.42	359	24.63	9.99
8481-6103	8.25	1760	23.24	3.98	441	263.79	161.89
8483-12704	0.43	527	0.36	5.12	3289	23.78	810.14
8488-12702	5.73	773	7.09	6.19	385	45.06	21.00
8488-12705	1.59	659	1.68	3.87	387	17.20	8.11
8546-6102	0.77	660	0.81	4.07	357	7.28	2.92
8548-6104	8.21	1051	13.80	1.53	392	361.17	174.74
8549-3703	4.34	470	3.26	1.60	493	102.75	78.65
8550-12703	0.62	495	0.49	1.36	372	13.67	5.97
8550-3701	4.75	1015	7.72	1.10	457	328.03	215.42
8551-12701	8.59	736	10.12	2.94	378	132.91	59.76
8551-6104	0.26	906	0.38	2.16	397	7.12	3.53
8554-3704	1.41	404	0.91	1.36	351	23.96	9.29
8555-1901	0.86	1113	1.53	1.08	343	49.43	18.31
8564-9102	0.26	337	0.14	2.28	332	2.10	0.73
8568-3704	5.43	180	1.56	2.04	366	28.76	12.13
8569-6104	0.21	732	0.24	1.98	371	4.67	2.03
8570-3701	0.67	382	0.41	0.79	349	18.47	7.07
8588-12705	0.39	450	0.28	2.40	334	4.03	1.41
8588-6101	8.49	189	2.56	1.71	432	66.18	38.83
8592-3702	1.12	828	1.48	3.19	355	16.87	6.69
8597-12703	1.42	226	0.51	2.68	377	7.42	3.33
8597-12704	1.58	675	1.71	1.96	368	32.85	13.99
8601-12703	0.41	2779	1.84	6.82	608	16.78	19.56
8601-6103	0.63	357	0.36	1.12	339	11.19	4.06
8609-12701	3.20	978	5.00	1.25	462	188.63	126.66
8610-12703	3.08	1368	6.74	1.57	429	188.08	109.26
8611-9102	0.68	745	0.81	0.91	355	32.33	12.85
8612-12705	13.72	1166	25.61	4.80	406	222.05	115.57
8612-6104	5.15	326	2.69	1.83	374	55.99	24.65
8615-3703	0.07	167	0.02	1.93	335	0.32	0.11
8616-12704	5.23	932	7.80	1.37	813	474.37	988.07
8616-3704	0.93	310	0.46	0.86	409	22.49	11.83

PlateIFU	$L_{\rm OIII,wing}$ ($10^{39}\,{\rm erg\,s^{-1}}$)	n_e ($\rm cm^{-3}$)	$M_{\rm gas}$ ($10^3\,M_\odot$)	$R_{\rm out}$ (kpc)	$v_{\rm out}$ ($\rm km\,s^{-1}$)	$\dot{M}$ ($10^{-5}\,M_\odot\,\rm yr^{-1}$)	$\dot{E}$ ($10^{36}\,\rm erg\,s^{-1}$)
8616-9101	11.63	1527	28.41	5.30	406	222.61	115.67
8618-12703	0.29	1438	0.67	3.48	345	6.80	2.55
8622-12703	0.35	632	0.36	7.99	378	1.73	0.78
8626-12702	3.09	1258	6.21	1.28	458	227.48	150.62
8652-6103	6.51	784	8.17	1.33	389	244.33	116.21
8652-6104	0.63	88	0.09	1.32	337	2.32	0.83
8656-6101	1.27	755	1.53	0.74	363	76.53	31.72
8657-1902	7.09	246	2.79	2.43	477	55.93	40.10
8657-6101	52.69	127	10.71	1.19	443	408.31	252.08
8657-9101	0.21	167	0.06	8.11	450	0.32	0.21
8710-12703	0.05	602	0.05	4.15	379	0.47	0.21
8712-1902	0.36	81	0.05	1.36	336	1.19	0.42
8719-12702	0.17	963	0.26	3.56	355	2.67	1.06
8723-12704	3.26	738	3.85	1.05	508	190.07	154.55
8723-1902	0.70	685	0.76	1.15	366	24.75	10.43
8723-3702	9.95	64	1.03	0.80	406	53.20	27.62
8725-3701	0.32	302	0.16	4.75	341	1.14	0.42
8726-12701	3.86	965	5.96	1.33	442	201.80	124.32
8727-12705	2.03	282	0.91	0.78	413	49.69	26.74
8931-12702	0.97	376	0.58	1.02	383	22.55	10.41
8931-9101	0.50	2068	1.65	0.84	403	80.96	41.48
8935-6104	0.89	318	0.45	1.72	347	9.27	3.51
8937-1902	2.87	2984	13.72	0.69	409	825.16	433.95
8940-3701	2.21	4650	16.46	1.59	447	472.37	297.29
8940-6104	2.69	602	2.59	1.68	415	65.77	35.72
8942-6104	1.27	1385	2.82	0.81	419	149.35	82.69
8942-9101	0.02	813	0.03	5.42	318	0.19	0.06
8944-3704	0.91	101	0.15	2.17	349	2.41	0.92
8945-3702	3.65	179	1.05	4.96	351	7.57	2.94
8950-12705	1.70	1749	4.75	1.32	413	151.59	81.47
8950-1901	0.76	318	0.39	1.10	349	12.54	4.81
8952-3703	3.34	140	0.75	1.14	404	27.32	14.07
8952-6103	2.91	492	2.29	1.12	406	84.48	43.88
8978-12702	14.49	1375	31.88	10.00	359	116.92	47.37
8982-9101	35.63	556	31.68	0.91	457	1627.91	1072.28
8984-12704	1.21	1229	2.39	0.89	442	121.89	75.18
8984-12705	4.81	101	0.77	2.13	372	13.83	6.04
8985-6104	3.05	565	2.76	1.60	409	71.94	37.88
8987-9102	4.57	825	6.02	1.83	350	117.78	45.40
8989-1902	1.44	211	0.49	1.18	384	16.30	7.58
8991-12705	0.04	426	0.02	3.53	336	0.24	0.08
8992-3701	1.64	1771	4.64	0.77	519	318.01	269.42
8992-6101	12.84	121	2.48	1.34	476	90.15	64.41
8994-9102	2.34	967	3.62	1.02	425	154.07	87.73

PlateIFU	$L_{\rm OIII,wing}$ ($10^{39}\,{\rm erg\,s^{-1}}$)	n_e ($\rm cm^{-3}$)	$M_{\rm gas}$ ($10^3\,M_\odot$)	$R_{\rm out}$ (kpc)	$v_{\rm out}$ ($\rm km\,s^{-1}$)	$\dot{M}$ ($10^{-5}\,M_\odot\,\rm yr^{-1}$)	$\dot{E}$ ($10^{36}\,\rm erg\,s^{-1}$)
8996-3704	6.73	1310	14.11	1.20	363	438.84	182.48
8998-3702	1.18	2323	4.40	0.79	540	308.32	283.03
8999-12704	0.19	735	0.23	3.64	376	2.39	1.06
8999-9101	0.36	1372	0.78	0.73	356	39.03	15.62
9001-6104	1.72	212	0.58	1.03	439	25.36	15.37
9025-1902	0.87	114	0.16	1.64	350	3.48	1.35
9025-3702	2.96	195	0.92	1.59	410	24.34	12.86
9027-1902	0.40	991	0.63	0.77	408	34.22	17.92
9027-3701	13.38	575	12.31	2.45	447	230.00	145.02
9029-12705	1.53	162	0.40	6.60	409	2.51	1.32
9029-1902	0.53	467	0.40	0.92	336	14.71	5.22
9031-12703	8.51	1037	14.12	3.58	473	190.91	134.45
9031-3702	2.20	520	1.83	1.22	342	52.22	19.20
9032-3704	19.47	121	3.76	1.27	471	143.02	99.90
9032-6104	0.25	1450	0.58	1.62	366	13.49	5.69
9034-1902	0.69	1184	1.30	0.78	366	62.05	26.19
9034-6101	0.29	2498	1.16	0.86	348	47.92	18.30
9037-1902	0.14	1202	0.26	0.35	382	29.66	13.63
9041-12702	0.82	343	0.45	3.45	347	4.63	1.76
9041-1902	0.82	1042	1.36	1.19	384	45.08	20.98
9041-6102	5.09	639	5.20	2.71	378	73.99	33.27
9041-9102	0.55	132	0.12	3.33	364	1.29	0.54
9046-12703	34.74	3198	177.81	33.52	469	254.65	176.83
9047-3701	0.65	543	0.56	2.17	378	10.00	4.50
9049-12701	7.02	650	7.31	5.87	433	55.16	32.61
9049-3701	0.52	517	0.43	1.14	351	13.69	5.30
9086-12702	0.20	382	0.13	3.50	341	1.25	0.46
9087-12704	0.58	290	0.27	1.29	358	7.60	3.07
9088-3702	3.40	1026	5.58	0.82	2798	1954.04	48185.07
9089-12701	6.34	196	1.99	1.29	662	104.12	143.73
9093-12705	1.09	124	0.22	1.30	363	6.17	2.57
9093-3704	8.40	2324	31.25	1.07	541	1610.46	1482.84
9094-3701	5.80	68	0.63	7.98	379	3.05	1.38
9181-1902	0.21	518	0.18	2.14	355	2.99	1.18
9183-12705	38.00	477	29.00	1.33	374	836.42	368.35
9185-9101	35.48	857	48.64	5.41	389	358.14	170.91
9186-3701	0.30	495	0.24	2.72	397	3.58	1.78
9188-1901	6.62	82	0.87	1.40	355	22.43	8.91
9188-6104	0.30	1317	0.62	1.11	354	20.34	8.01
9190-1901	0.05	339	0.03	1.12	344	0.86	0.32
9193-6101	1.47	3386	7.95	1.02	532	425.66	380.21
9194-12701	2.60	373	1.55	2.14	354	26.27	10.35
9194-12703	0.98	290	0.45	3.97	419	4.91	2.72
9194-6104	2.08	372	1.24	4.55	374	10.44	4.60

PlateIFU	$L_{\rm OIII,wing}$ ($10^{39}\,{\rm erg\,s^{-1}}$)	n_e ($\rm cm^{-3}$)	$M_{\rm gas}$ ($10^3\,M_\odot$)	$R_{\rm out}$ (kpc)	$v_{\rm out}$ ($\rm km\,s^{-1}$)	$\dot{M}$ ($10^{-5}\,M_\odot\,\rm yr^{-1}$)	$\dot{E}$ ($10^{36}\,\rm erg\,s^{-1}$)
9195-12701	0.00	1173	0.00	nan	nan	nan	nan
9195-12704	0.06	984	0.09	3.73	323	0.80	0.26
9196-1902	0.65	218	0.23	0.71	442	14.35	8.84
9485-6104	5.73	463	4.24	1.25	371	128.59	55.61
9488-12704	0.01	1060	0.02	2.42	354	0.37	0.15
9488-1901	0.53	1089	0.92	0.63	430	63.84	37.14
9492-12701	0.34	216	0.12	1.65	361	2.67	1.10
9493-1902	2.29	209	0.76	0.68	508	58.37	47.36
9493-6103	0.12	370	0.07	2.86	410	1.07	0.57
9493-9102	0.91	597	0.87	1.11	341	27.45	10.03
9494-3701	0.24	1426	0.55	1.06	404	21.57	11.09
9494-9102	1.66	99	0.26	0.66	343	13.99	5.19
9499-6102	1.96	148	0.46	1.64	361	10.43	4.27
9503-3702	0.75	891	1.07	1.59	377	25.91	11.63
9509-6104	0.36	486	0.28	1.91	338	5.12	1.84
9511-3704	5.86	292	2.73	1.50	367	68.28	28.97
9511-6101	1.17	363	0.68	1.21	487	27.91	20.85
9511-6102	0.92	1182	1.74	1.00	352	62.88	24.55
9511-6103	5.58	194	1.73	1.49	470	56.07	38.99
9513-3702	3.37	623	3.36	1.24	490	136.16	102.87
9514-12703	2.50	901	3.61	1.16	435	138.61	82.53
9514-12704	0.48	719	0.55	0.79	347	24.56	9.34
9862-12703	0.72	1573	1.82	1.12	396	65.61	32.40
9865-6104	2.16	929	3.21	10.16	465	15.02	10.22
9866-12703	1.57	895	2.25	1.52	363	54.80	22.75
9869-6101	0.56	551	0.50	1.47	358	12.29	4.95
9872-3701	0.43	1082	0.74	1.72	372	16.27	7.08
9872-6104	0.07	373	0.04	2.12	325	0.61	0.20
9872-9101	3.81	113	0.69	1.84	365	13.94	5.85
9878-12701	0.55	381	0.34	1.16	345	10.33	3.88
9878-3703	5.56	695	6.19	0.93	451	306.34	196.29
9879-12704	2.83	1065	4.82	2.29	364	78.36	32.66
9881-9102	0.32	284	0.14	7.71	334	0.64	0.22
9882-6102	0.06	1535	0.15	4.59	316	1.06	0.33
9883-3703	2.61	1242	5.18	0.82	713	460.29	737.52
9885-1901	1.47	176	0.41	1.26	349	11.70	4.49
9888-12704	4.53	259	1.88	2.21	370	32.03	13.78
9889-12705	63.13	1247	125.92	2.65	521	2530.98	2161.00
9891-1901	12.18	278	5.42	1.32	333	140.30	49.06
9894-3701	1.58	1243	3.14	1.17	433	118.43	69.94

Acknowledgements

First of all, I would like to thank Dr. Dominika Wylezalek for entrusting me with this great project and her supervision. She always led me in the right direction, but also gave enough room to develop and follow my own ideas, which I highly appreciate.

I also want to thank Dr. Marco Albán, who always took the time to answer my questions in the first phase of the project and for supplying the crucial data for this work. In addition, special thanks to Sandra Jaison and Dr. Lara Gatto for their time and also for supplying their data as reference. Furthermore, I want to thank Dr. Jochen Heidt for taking his time to read and evaluate my thesis.

Studying physics would have been impossible for me to do alone, so I want to express my sincere gratitude to my friends for the countless hours and discussions. For their constant support, always open ears and help with the corrections, thanks to Lisa and Anna.

Erklärung

Ich versichere, dass ich diese Arbeit selbstständig verfasst und keine anderen als die angegebenen Quellen und Hilfsmittel benutzt habe.

Heidelberg, den 11.03.2026,